INAUGURAL-DISSERTATION

zur Erlangung der Doktorwürde

der Naturwissenschaftlich-Mathematischen
Gesamtfakultät

der Ruprecht-Karls-Universität
Heidelberg

vorgelegt von

M.Sc. Tobias Wächter
aus Bochum

Tag der mündlichen Prüfung: 13. Januar 2017

Charge Transfer in Monomolecular Films & Metal-Organic Frameworks

Gutachter:
Prof. (apl.) Dr. Michael Zharnikov
Prof. Dr. Dirk-Peter Herten

To my wife Tabea & my soon to be born child

Zusammenfassung

Die Analyse und das Verständnis der elektronischen Eigenschaften von Nanomaterialien ist ein wichtiges Thema der modernen Nanotechnologie, besonders im Bereich molekularer und organischer Elektronik. Als Beitrag zur aktuellen Forschung auf diesem Gebiet, wurde in dieser Arbeit der Ladungstransport (LT) von zwei geeigneten Systemen analysiert.

Zuerst wurde die Dynamik von Elektronentransfer (ET) in einem 2D Aufbau molekularer Drähte, selbstorganisierende Monoschichten (SAMs), mittels resonanter Augerelektronenspektroskopie (RAES) in Kombination mit einer core hole clock (CHC) Methode untersucht. Eine Reihe von geeigneten SAMs wurde designt, um auf spezielle Fragestellungen zur Dynamik von ET einzugehen. Die meisten der SAMs waren mit Nitrilgruppen ausgestattet, welche als vordefinierte Ziele für resonante Anregung eines Elektrons dienten, das während dem Transfer beobachtet wurde. Die Experimente ließen eine ähnliche Effizienz der elektronischen Kopplung der gängigsten Ankergruppen S und Se an das Substrat erkennen und lieferten damit die Lösung zu einer lang diskutierten Kontroverse. Ferner wurde ein effizienter ET in acene-basierten SAM Komponenten gefunden, was durch einen recht niedrigen Wert der Tunnelkonstante (β) von $0.25\,\text{Å}^{-1}$, vergleichbar mit der von Oligophenylen, belegt wurde. In weiteren Experimenten an einem analogen nicht benzenoiden Molekül, wurden die gleichen ET Eigenschaften wie für das benzenoide Isomer gefunden. Für einen eindeutigen Beweis der Methode wurden die Nitrilgruppen direkt auf das Substrat aufgebracht. Hierbei zeigte sich wie bereits erwartet eine ET Zeit (τ_{ET}) im sub-fs Bereich. Ein gut erkennbarer Beitrag des ET Prozesses im RAES [N 1s]π^* Spektrum von Pyridyl-substituierten Molekülen legte dar, dass diese Gruppe für CHC Experimente geeignet ist und als passende Alternative zu Nitril betrachtet werden kann. Unterdessen zeigten die Spektren NO_2-funktionalisierter SAMs Anzeichen für einen inversen ET Prozess.

Als Zweites wurden die statischen LT Eigenschaften von metallorganischen Gerüstverbindungen (SURMOFs) betrachtet, die auf ein Substrat aufgewachsenen sind. Als geeignetes Referenzsystem diente das gut erforschte HKUST-1 Gerüst. Die Messungen wurden mit einem speziell designten two-terminal junction Aufbau durchgeführt und sowohl unbeladene als auch mit Gastmolekülen beladene SURMOFs wurden untersucht. Die unbeladenen SURMOFs zeigten

LT Eigenschaften, vergleichbar mit metallorganischen molekularen Drähten, was sich in einem sehr niedrigen β Wert von $0.006\,\text{Å}^{-1}$ wiederspiegelte. Zusätzliche LT Messungen nach Beladung der SURMOF Poren mit den Gastmolekülen Ferrocen, Tetracyanoquinodimethan (TCNQ) und dem fluorierten F4-TCNQ zeigten eine erhebliche Zunahme der Stromdichte. Dieser Anstieg war mit bis zu 6 Größenordnungen besonders hoch nach TCNQ Beladung. Das Ergebnis bestätigte einen vorherigen Bericht für dieses spezielle Gastmolekül, aber in diesem Fall für Proben mit kontrollierter Dicke und Qualität. Die Ergebnisse für Beladung mit F4-TCNQ zeigten, im Gegensatz zu dem vorherigen Bericht, einen mit TCNQ vergleichbaren starken Anstieg der Stromdichte, was den vorgeschlagenen LT Mechanismus in Frage stellte. Diese Beobachtungen konnten für SURMOFs verschiedener Orientierung und Beladung durch verschiedene Lösungsmittel bestätigt werden. Basierend auf den experimentellen Daten, wurde für TCNQ und F4-TCNQ ein neuer superexchange Mechanismus für LT vorgeschlagen.

Abstract

Characterization and understanding of electronic properties of nanoscale systems is an important issue in modern nanotechnology including molecular and organic electronics. To advance in this topic, charge transfer (CT) properties of two specific nanoscale systems were analyzed in detail in this work.

First, electron transfer (ET) dynamics in supported 2D assembles of molecular wires, self-assembled monolayers (SAMs), were studied by resonant Auger electron spectroscopy (RAES) in a combination with a so-called core hole clock (CHC) approach. A variety of suitable SAMs were custom-designed to address specific questions within the general framework of ET dynamics; most of these SAMs were equipped with nitrile tail groups, serving as a predefined site for the resonant excitation of an electron making the ET. The experiments showed a similar electronic coupling efficiency to coinage metal surfaces for the most frequently used S and Se anchors, solving a long-term controversy. Further, an efficient ET was found in acene-based SAM constituents, manifested by a quite low tunneling decay constant (β) of $0.25\,\text{Å}^{-1}$, similar to that of oligophenyls. In subsequent experiments on an analogous non-benzenoid system, the same ET properties as for its benzenoid isomer were found. As an ultimate proof of the approach, the nitrile groups were attached directly to the substrate, showing an ET time (τ_{ET}) in the sub-fs region, as has been expected. A well-perceptible contribution of the ET process in the RAES [N 1s]π^* spectra of pyridyl-substituted molecules revealed that pyridyl is a suitable resonant group for CHC and can be efficiently used as an alternative to nitrile, while NO_2-functionalized SAM constituents exhibited an inverse ET process.

Second, static CT properties of surface-anchored metal-organic frameworks (SURMOFs) were studied, taking the basic and well-known HKUST-1 framework as a most suitable reference system. The measurements were performed with the custom-designed two-terminal junction setup and both pristine and guest-molecule loaded SURMOFs were investigated. The pristine SURMOFs showed CT properties similar to hybrid metal-organic molecular wires, as manifested by a very low β value of $0.006\,\text{Å}^{-1}$. The CT experiments performed after the incorporation of the guest molecules, viz. ferrocene, tetracyanoquinodimethane (TCNQ) and its fluorinated analog F4-TCNQ, into the pores of the framework showed a significant increase in the current density. This increase

was especially dramatic in the case of TCNQ, achieving up to 6 orders of magnitude. This finding verified a previously reported and highly announced result for this particular guest molecule, obtaining it, however, for the samples of well-controlled thickness, quality and orientation. At the same time, in contrast to the previous report, loading with F4-TCNQ resulted in a similar increase in the current density as for TCNQ, questioning the proposed CT model. These observations were made for several orientations of the SURMOF and different solvents used for the loading. Based on the experimental data, a novel superexchange mechanism for CT in the redox-molecule-loaded SURMOFs was proposed.

Contents

List of Figures

List of Tables

1. Introduction

Within my thesis, I focused on two different nanoscale systems: first, on self-assembled monolayers (SAMs), which are monomolecular films of rod-like molecules attached to a suitable substrate; second, on novel metal-organic, nanoporous materials grown on a solid support, called surface-anchored metal-organic frameworks (SURMOFs), formed by metal centers linked by organic ligands[1,2] giving three-dimensional crystalline structures.

The first mentioned SAMs are an indespensable playground of surface science and physical chemistry of interfaces as well as an important element of modern nanotechnology, including molecular and organic electronics.[3–5] In this context, the characterization of the electronic properties of these systems is an important topic in actual research, which was addressed by several experimental tools as well as by the theory. Some of the established methods are conducting probe atomic force microscopy (AFM),[6,7] scanning tunneling microscopy (STM),[8–14] mercury drop based molecular junctions[15–17] and the eutectic gallium indium (EGaIn) top contact method.[18] Within these experimental approaches, a variety of valuable data was obtained, although, due to limitations of the particular experiments, viz., insufficient characterization of the molecular assembles studied, undefined number of participating molecules, uncertain shape of the nanoelectrodes,[19] and non-defined quality of the top-contact, these data showed a certain scattering. The studies implied that the major mechanisms for charge transfer (CT) in SAMs are nonresonant tunneling and hopping.[20] In the former case, the transport properties depend on the internal coupling between the building units of a SAM-molecule, whereas, in the latter case, CT efficiency is affected by the exact position of the mediating state with respect to involved molecular orbitals (MOs).[6,8,15,20–23] The CT properties of SAMs could be described in most cases by the equation $J = J_0 exp(-\beta l)$ with β being the most important parameter, generally called *tunneling decay constant* and J being the current through a metal-molecule-metal junction. J_0 is a parameter closely related to the molecular contact resistance and l the length of the molecules.[4] The CT properties described by β are mostly related to the molecular backbone, also referred to as "molecular wire (MW)". The lower the value of β, the better the conductivity of the SAM-film. The tunneling decay constant is depending on the identity of the molecular backbone

(β=0.41-0.7 Å^{-1} for oligophenyls[6,10,15,20,24] or β=0.87 Å^{-1} for alkanes[16]) and the length of the backbone,[21] but for some systems, also on the character of the anchor group.[14] Significantly lower values of β (down to 0.001 Å^{-1}) could only be obtained for molecular systems with incorporated metal centers, related to the specific alignment of the MOs involved in the resonant tunneling.[25,26]

All the above experimental strategies and results refer only to the static properties of SAMs, while the dynamic CT properties are mostly unexplored. To understand these properties, a so called core hole clock (CHC) approach within a framework of resonant Auger electron spectroscopy (RAES) was adapted and applied by our group,[27] following the studies by A. Wee et al.[28] Within this method, a transfer of electrons from a specific excitation state to the conductive substrate can be traced. For this purpose, the spectral signatures of different possible decay routes after resonant excitation of a core electron into a bound state are monitored. A specific electron transfer time (τ_{ET}) for a defined pathway can then be obtained from the relation $\tau_{ET} = \tau_{core}(1 - P_{ET}/P_{ET})$ with the portion of electron transfer events ($\mathrm{P_{ET}}$) extracted by a dedicated spectral decomposition procedure from the RAES data. The known lifetime τ_{core} of inner shell vacancy in atoms, common for organic molecules, is in the fs time domain and serves as an internal time reference giving the name to the entire approach.[27,29–31] The detectable range of τ_{ET} is given by $0.1\tau_{core} < \tau_{ET} < 10 - 20\tau_{core}$, viz., ∼0.6 fs to ∼120 fs for common τ_{core} (6.4 fs for N 1s),[32] referring to the largest and smallest perceptible $\mathrm{P_{ET}}$ after decomposition of the REA spectra.

In the previous studies of our group, this method has been used to study specifically designed SAM systems. The major idea of the design was to unequivocally define the pathway of the electron transfer (ET) after the resonant excitation.[33] This made the interpretation of the RAES results straightforward as compared to the situation when the excitation involves several atoms of the molecular backbone.[28,34] Considering that commonly used backbones are mostly composed of hydrocarbons, a nitrile moiety (−C≡N) was introduced, as the most suitable group, allowing site-specific resonant [N 1s]π^* excitation of an electron into an unoccupied valence orbital, with subsequent ET through the molecular backbone to the conductive substrate. Following a recently developed approach,[35,36] the nitrile group also served as a suitable spectroscopic marker to unambiguously determine molecular orientation in the studied systems. Most common molecular backbones, viz. aliphatic[33,37] and (oligo)phenyl[36,38] chains were studied and, similar to the static conductance experiments, their length was varied. Significantly, the application of the CHC approach solves the problem of the top contact, along with the controversy regarding the amount of involved moieties in static experiments since the results are representative of

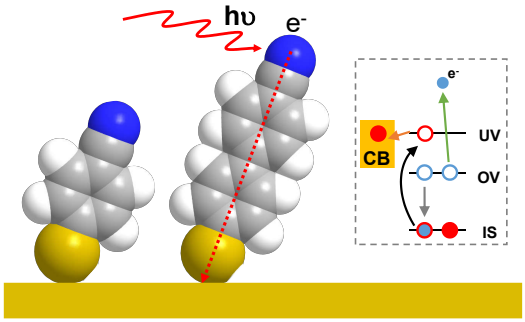

Figure 1.1.: Two molecules with different molecular length, but same general layout showing the unequivocally defined pathway of electron transfer (red dotted arrow) from the resonantly excited tail group to the substrate in the framework of RAES-CHC (inset shows the monitored ET decay route after resonant excitation).

individual molecules. The defined pathway of the ET is schematically shown in figure 1.1 (red dotted arrow) and the inset exhibits the monitored decay route of electron transfer (ET) after resonant excitation (black arrow). Within these studies, it was found that alkanethiols on Au(111) show an exponential decrease in τ_{ET} with increasing molecular length, described by an attenuation factor of 0.93 per methylene unit ($0.72\,\text{Å}^{-1}$; tunneling along the chain assumed) with a τ_{ET} of ∼100 fs for a chain length of only four CH_2 units.[37] Further ET dynamics in a series of conjugated SAMs with an oligo(phenylenethynylene) and oligo(phenyl) backbone were found to strongly depend on the respective MOs mediating the process. The values of β_{OPh} for π_1 and π_3 excitation were found to be 1.25 and 2.34 per phenyl ring ($0.29\,\text{Å}^{-1}$ and $0.55\,\text{Å}^{-1}$), respectively.[38] The MO-depending ET was later verified for the alkane backbone as well, relying on the symmetry of the respective MOs.[39]

To continue and extend the above studies, I investigated further SAM systems addressing specific questions within the framework of ET dynamics in these assembles: (i) the effect of molecular anchor; (ii) ET properties of an acene backbone; (iii) ET properties of a non-benzenoid aromatic molecule; (iv) the ultimate proof of ET by direct attachment of the nitrile groups to the substrate and (v) the suitability of alternative tail groups for site-specific resonant excitation. Besides the CHC experiments, the SAM samples were also extensively characterized by advanced X-ray spectroscopy allowing to determine their structural parameters, proving the film quality and establishing a basis for the CHC studies.

(i) In addition to sulfur, selenium is also a popular anchor in SAM-chemistry on coinage metal substrates.[40–45] The Se−Au vs S−Au bond stability[40,41,46–48]

and the conductance of the respective monolayers[49–52] are still under discussion. Controversial conclusions, derived on the basis of different experiments involving insufficiently studied and/or not equivalent test systems, are reported in the literature. To solve these controversies, I introduced a model system of 6-cyanonaphthalene-2-thiol (NC-NapSH) and the Se-containing analog 6-cyanonaphthalene-2-selenoacetate (NC-NapSeAc). The SAMs of both precursors were extensively characterized by a combination of spectroscopic and microscopic techniques to prove the film quality and similarity, establishing a reliable basis for the comparison of their ET dynamics.

(ii) Further, to investigate the dynamic ET properties of SAMs with aromatic acene backbones and verify the effects of the headgroup exchange (S↔Se) the SAM precursors 6-cyanoanthracene-2-thiol (NC-AntSH) and its Se analog 6-cyanoanthracene-2-selenoacetate (NC-AntSeAc) were introduced and underwent the same dynamic transport analysis as the NC-NapS/Se films. The compiled dataset of dynamic ET properties of acenes provided a reasonable basis for comparison with results from static measurements found in the literature.[22,53]

(iii) In addition to the length effect, I also investigated the suitability of a non-benzenoid aromatic molecule by introducing the SAM precursor 6-cyanoazulene-2-thiol (NC-AzuSH). The only difference to the NC-NapS/Au system was the isomerized backbone, providing a reliable basis for the comparison of their respective dynamic ET properties.

(iv) Motivated by a previous study, which observed a time of ∼2.5 fs for ET across the thiolate head group,[37] I present an ultimate proof of ET by directly attaching the −C≡N moiety to the Au(111) substrate. The orientation of the cyanide, which was important for the CHC experiments, was probed by spectroscopic and microscopic methods.

(v) To test alternative groups for site-defined resonant excitation and subsequent CHC analysis, I introduced two different model systems with either a pyridine ring or a nitro ($-NO_2$) group attached to (oligo)phenylthiols. Both groups show a well-defined [N 1s]π^* excitation comparable to the nitrile group.[54,55]

The pyridine sub-project was particularly interesting, because the nitrogen is directly involved in the aromatic ring system,[56] which can influence the dynamic properties of the excited electron. To monitor the effects of these differences and acquire τ_{ET}, several pyridyl-substituted SAMs were designed. The study of their nitrile-substituted analogs has been reported in the literature and was consulted for evaluation of the results.[38]

To investigate the performance of the NO_2 group, a series of substituted (oligo)phenylthiols was introduced. The nitro group is of particular interest due to its polar character[57] and that additionally to the well-defined [N 1s]π^* excitation,[58] also the oxygen core level can be addressed by [O 1s]π^* excitation.

The second focal point of my studies was the understanding of electronic transport properties of SURMOFs, which is important both from a fundamental perspective as well as with regards to possible applications of these novel materials in electronic devices.[1,59,60] Their high porosity and surface area make them promising materials for storage,[61–63] catalysis,[64] sensors and drug delivery just to name some of the other potential application areas.[1] They also can serve as a component for electronic devices[65–69] as either a supportive material (a scaffold for fuel cells,[70] and batteries[71,72]) or be actively involved in the charge transport. Although their high potential as building blocks for electronic devices is promising, their fundamental transport properties and underlying mechanism still needed to be clarified.

As a first step for these mostly unexplored systems, I studied the static CT properties of representative SURMOFs, based on the metal-organic framework (MOF) HKUST-1,[73] formed by copper nodes and trimesic acid, sprayed layer by layer on a COOH-terminated SAM,[74–76] in two-terminal junctions with either mercury[24] or EGaIn[18] as the top electrode (the substrate served as the bottom electrode,[77–80] as shown schematically in figure 1.2).

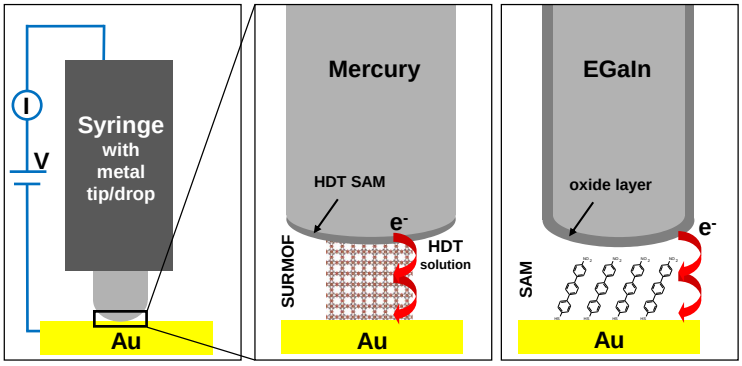

Figure 1.2.: On the left side the scheme of the junction setup is shown. The two cartoons in the center and on the right side explain schematically two possibilities for two-terminal junctions: Hg/HDT//SURMOF/Au and EGaIn/OxLayer//SAM/Au.

Further, motivated by a recent study reporting a huge increase in electrical conductivity after loading HKUST-1 with 7,7,8,8-tetracyanoquinodimethane (TCNQ),[81] I tried to perform analogous experiments in a more controlled fashion. For this purpose I modified the transport properties of the pristine SURMOFs by introduction of suitable guest molecules, viz. ferrocene (Fc), TCNQ and the fluorinated analog 2,3,5,6-tetrafluoro-7,7,8,8-tetracyanoquinodimethane (F4-TCNQ),[81] into their pores and monitored the charge transfer, using the same junction setup as for the pristine system. Additionally the sol-

vent, used for loading, and the SAM-template were varied and following effects on the film structure and the transport properties were monitored. Based on the experimental results, theoretical calculations were performed by our partner groups, revealing the relevant CT mechanisms in both the pristine and loaded SURMOFs.

The majority of the above studies were performed in collaboration with our partner groups in Germany and abroad. Their data, as far as necessary for the understanding of the conclusions or proving the quality and character of the investigated samples, can be found in the Appendix A. Detailed information will be provided in the respective chapters.

2. Basics & Background

In this chapter the background information and basic knowledge about the investigated systems and the used analytical methods are described.

2.1. Self-Assembled Monolayers

A self-assembled monolayer (SAM) is a monomolecular film, formed by adsorption of organic molecules onto the surface of a suitable solid or liquid substrate. The most comprehensivly studied SAM systems are alkanethiols on gold,[82–90] silver,[89,91,92] copper,[89] palladium,[93,94] platinum,[95] and mercury.[96] Gold is well-suited as a substrate, because thin films can be prepared by physical vapor deposition (PVD) and and will not form an oxide layer in ambient air. Any physically or chemically bound contamination can be removed be exposition of the substrate to ultraviolet (UV) light. Silver for example forms an oxide layer and therefore should be handled under inert gas conditions. Thiols, with their high affinity to metal surfaces, are suitable, because they can displace nearly all possible adsorbed molecules from the gold surface. SAMs generally consist of three parts, the *head group*, the *molecular chain* and the *functional group* (see figure 2.1). The *head group* binds the molecule to the substrate and the *molecular chain* or spacer is the connection between the head group and the functional group. In general it is an aliphatic or aromatic chain, which also defines the film thickness and protects the substrate surface. Typically the thickness of a SAM film is in the range of 1 nm to 3 nm. Lastly, the *functional group* defines the chemical or physical properties of the formed SAM at the interface. The process of SAM formation is not understood in detail. That the sulfur is bound to the gold as a thiol could be shown by X-ray spectroscopy.[97] Following Wood's notation, alkanethiol SAMs on Au(111) form a basic $(\sqrt{3} \times \sqrt{3})R30°$ monolayer with a $c(4 \times 2)$ superlattice. The spacing between the sulfur atoms is 4.97 Å and the calculated area per molecule is 21.4 $Å^2$.[98] Besides renowned thiol, selenol can also be a suitable headgroup.[40–45,99–102] Compared to thiols, which are usually stable in air, the analogous selenols easily oxidize. To bypass this, air-stable selenoacetes are commonly used to form selenolate SAMs on gold.[43] In the process of SAM formation, the acetate is removed, and a Au−Se connection forms. As the preparation and storage of SAMs does not generally

require ultrahigh vacuum (UHV) or other specialized conditions, they are easy to prepare and well-suited for investigations in the area of nanoscience and nanotechnology. They form on surfaces of any size or shape and the choosen characteristic structure affects the interfacial behaviour towards the macroscopic environment. Effects can be changes of the surface properties in terms of wetting, adhesion or friction and also optical or electronic coupling, which makes them an interesting tool for nanowires, thin films, colloids and similar structures.[103]

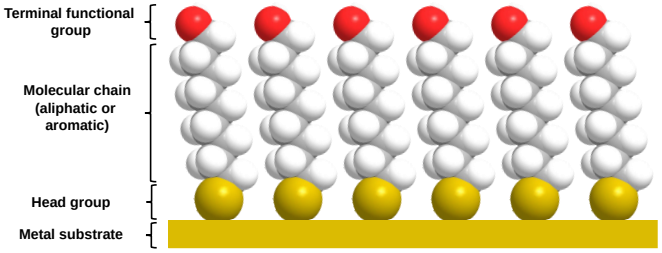

Figure 2.1.: Layout of an ideally ordered SAM on a metal substrate. The SAM characteristics are described on the left side. Drawn with ChemDraw.[104]

2.2. Metal-Organic Frameworks

2.2.1. Description

So called metal-organic frameworks (MOFs) are crystalline materials of ultrahigh porosity and high thermal (250 °C to 500 °C) and chemical stability (sodium hydroxide (NaOH), hydrochloric acid (HCl), methanol (MeOH), benzene). Due to the high variety of possible building blocks, more than 20 000 different MOFs have been studied in the past decade (see literature[1,2] for an overview of inorganic secondary building units (SBUs) and organic linkers).

The most well known and investigated MOFs are MOF-5 and HKUST-1. MOF-5 has a cubic framework with 61% porosity, a Brunauer-Emmett-Teller (BET) surface area of 2320 $m^2 g^{-1}$ and a Langmuir surface area of 2900 $m^2 g^{-1}$. In the MOF-5 the cationic SBU Zn_4O^{6+} is connected by 1,4-benzene-dicarboxylate (BDC) as an organic linker and forms $Zn_4O(BDC)_3$ as a continuous cubic neutral framework[105,106] (Figures 2.2a and 2.2c). HKUST-1 is made of a Cu^{2+} trimer and the organic linker 1,3,5-benzene-tricarboxylic acid (BTC) resulting in $Cu_3(BTC)_2$. The cubic system has a porosity of 40.7%, a BET surface area of 692.2 $m^2 g^{-1}$ and a Langmuir surface area of 617.6 $m^2 g^{-1}$[107] (Figures 2.2b and 2.2d).

2.2.2. Surface-Anchored Metal-Organic Frameworks

MOFs can also be used to modify a surface by growing them on or attaching them to a suitable, SAM functionalized substrate. Established functional groups are for example $-OH$, $-COOH$ or $-CH_3$. There are several approaches to construct surface-anchored metal-organic frameworks (SURMOFs): immersion of the substrate in a prepared "mother" solution,[73,108] microwave-induced thermal deposition,[109] electrochemical[110] and gel-layer synthesis,[111] evaporation induced crystallization[112] and step-by-step growth by repeated alternate immersion into a solution of the SBU and the organic linker.[75] The latter approach has been modified by changing the immersion cycles into spraying cycles[113] to receive monolithic, oriented and highly porous SURMOFs. By controlling the number of cycles, the thickness and the number of layers of the SURMOF can be influenced. Figure 2.2e shows the approach used to produce a SURMOF step-by-step using the spraying method. In steps 1 and 3 the SBU or the organic linker are sprayed on the surface. Steps 2 and 4 are cleaning steps to get rid of excess material by rinsing the sample with ethanol (EtOH).

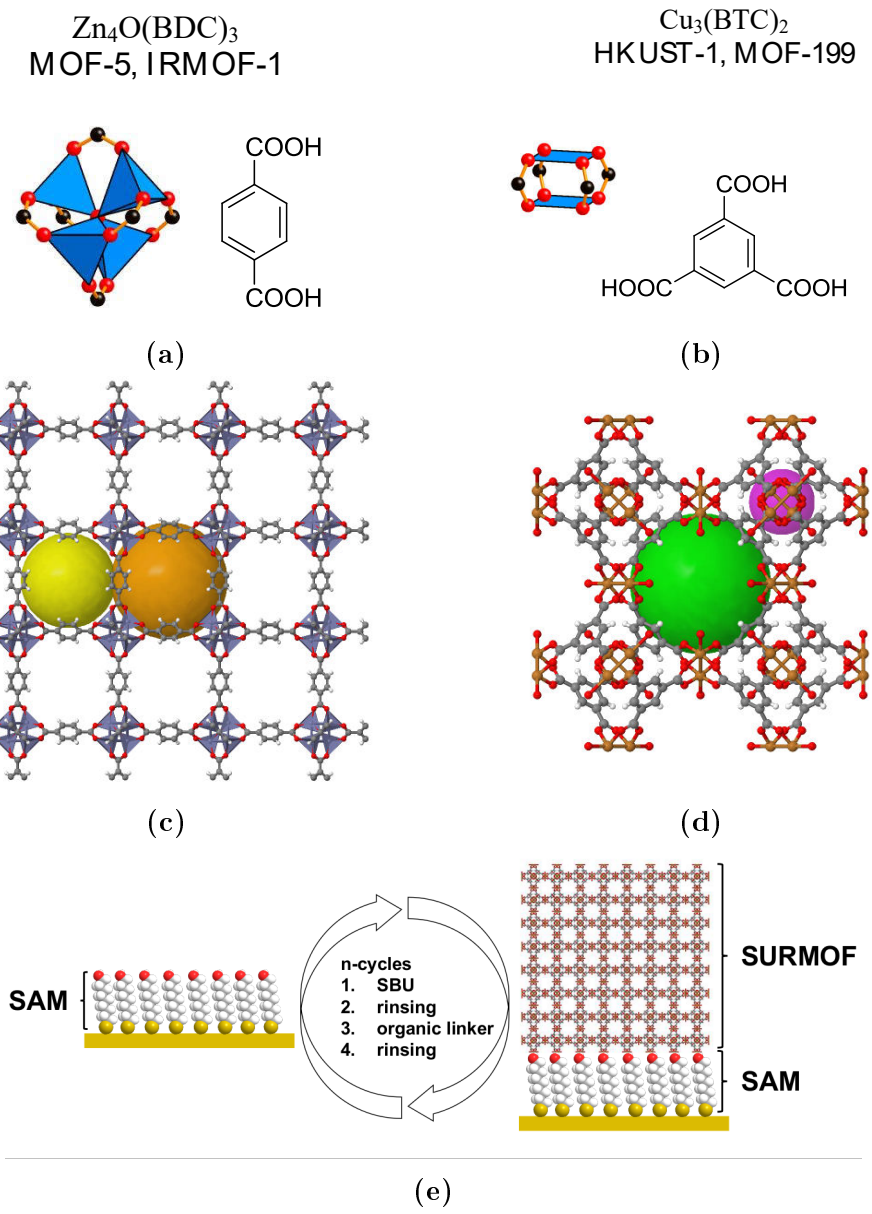

Figure 2.2.: (a) SBU (Zn_4O) and organic linker (BDC) used to build MOF-5; (b) SBUs (Cu_3) and organic linker (BTC) used to build HKUST-1; (c) and (d) show the MOF-5 and HKUST-1 structures, respectively. The spheres represent the pore size.[105] (e) Step-by-step spraying of SBU and organic linker to form a MOF on a SAM functionalized surface.[114]
(a) & (b) from [1]. Reprinted with permission from AAAS. (c) & (d) from ChemTube3D[115] and (e) drawn with ChemDraw[104] and MOF-structure from Chemtube3D[115]

2.3. Auger- and Photoelectron Spectroscopy

Photoelectron spectroscopy (PES) is the most important spectroscopy method to investigate the chemical composition, electronic structure and binding characteristics of interfaces or surfaces, taking advantage of the photoelectric effect. For PES a UHV system is necessary to provide an interference-free and contamination-free environment, which requires a pressure in the range of 1×10^{-9} mbar.

2.3.1. Photoelectron Spectroscopy

Depending on the energy of the light source used to excite the electrons in the sample, two main techniques can be distinguished: ultraviolet photoelectron spectroscopy (UPS) and X-ray photoelectron spectroscopy (XPS) using excitation energies of $h\nu \approx 10$ eV to 100 eV and $h\nu \approx 100$ eV to 1500 eV respectively. UPS can only give information about the electrons in the valence bond (density of states (DOS) and electronic structure), whereas XPS also samples the core electrons. The popularity of XPS is due to its sensitivity and specificity (element of interest >0.05 atomic %). All elements from Li - U in the outer 10 nm of a surface are detectable. Due to their low photoelectron cross sections, H and He can not be detected. The kinetic energy (E_{kin}) of the photoelectrons, emitted upon irradiation with X-rays or UV-light, is characteristic for each chemical element. If the conductive sample is physically connected to the analyzer, their Fermi level (E_F) are the same and the kinetic energy (E_{kin}) of the electrons measured by the analyzer is given by the following: equation[116,117]

$$E_{kin} = h\nu - E_B - \Phi_A \tag{2.1}$$

where $h\nu$ is the initiating photon energy, E_B is the binding energy of the electron according to the E_F, and Φ_A is the work function of the instrument, not the workfunktion of the sample (Φ_S). In figure 2.3 all relevant energy levels for XPS are shown. The analyzer work function Φ_A can be determined with a metallic reference sample, whose E_B was set to zero (Ag or Ni for example). After energy calibration Φ_A becomes zero and E_B and E_{kin} are directly related:[117]

$$E_{kin} = h\nu - E_B \tag{2.2}$$

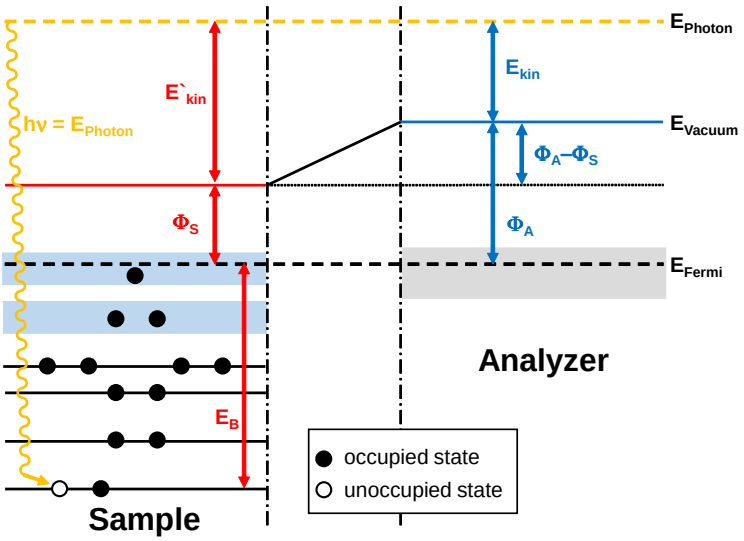

Figure 2.3.: Scheme of relevant energy levels in X-ray photoelectron spectroscopy.[117]

2.3.2. Auger Electron Spectroscopy

The vacancy in a core electron shell, is generally filled by an electron from a higher level (see figure 2.3). The excess energy can be released in two different ways. In the one case by emission of a characteristic X-ray or in the other case by emission of another electron, the Auger electron, which also has a characteristic energy. In figure 2.4 the scheme for Auger electron spectroscopy (AES) is shown. The Auger electron has the energy E_{WXY}, identical to E_{kin} of the emitted electron, which is constant, since it is independent of the excitation energy. The following equation describes E_{WXY}

$$E_{WXY} = E_W - E_X - E_Y - \Phi_A \tag{2.3}$$

with the energy of the different involved energy levels W, X and Y (see figure 2.4). Similar to the XPS case, Φ_A can be subtracted from the equation after calibration with a reference sample. Equation 2.3 is simplified and leaves out ionization and relaxation effects which are involved in any Auger transition. Following the approximation in the literature.[118] the energy for an Auger electron can be described as follows:

$$E_{WXY}(Z) = E_W(Z) - [E_X(Z) + E_X(Z+1) + E_Y(Z) + E_Y(Z+1)]/2 \tag{2.4}$$

All possible energies of Auger electrons from all possible transitions can be calculated with formula 2.4 using tables of electron energies. These tables can

be found in databases[119] and handbooks.[120] The resulting Auger lines are described in the obtained spectra along with the photoemission peaks.

To include all necessary information, the nomenclature of the peaks in AES describes the three respective energy levels, involved in the emission, as follows: $K_nL_mM_p$ with K_n describing the energy level with the electron hole, L_m the energy level for electron transition and M_p the energy level of the emitted electron.[117]

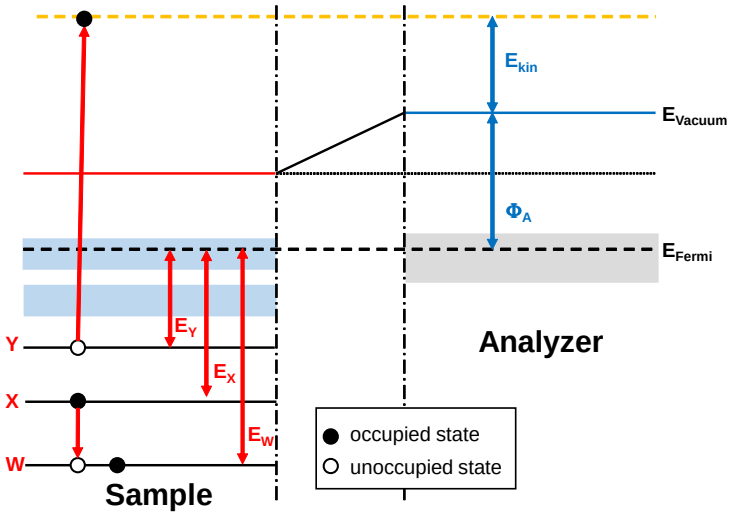

Figure 2.4.: Scheme of relevant energy levels in Auger electron spectroscopy.[117]

2.3.3. Spectrometer Setup

Figure 2.5 shows a typical setup for XPS, which consists of three parts: the X-ray source, the energy analyzer and the detector. Most of the conventional XPS setups use an X-ray source equipped with Mg or Al anodes, with characteristic radiation of MgK_α ($h\nu$=1253.6 eV) and AlK_α ($h\nu$=1486.6 eV). The most important part is the hemispherical energy analyzer, which determines E_{kin} of the photoelectrons. The electrons are going into the analyzer through a small slit and are circularly directed through the hemisphere according to their E_{kin}. Only electrons with a defined energy can reach the exit slit and are detected by the detector. The main task of the detector is to count the electrons according to their energy and intensity (counts per second). Afterwards the signal is converted and saved to a data file.[117]

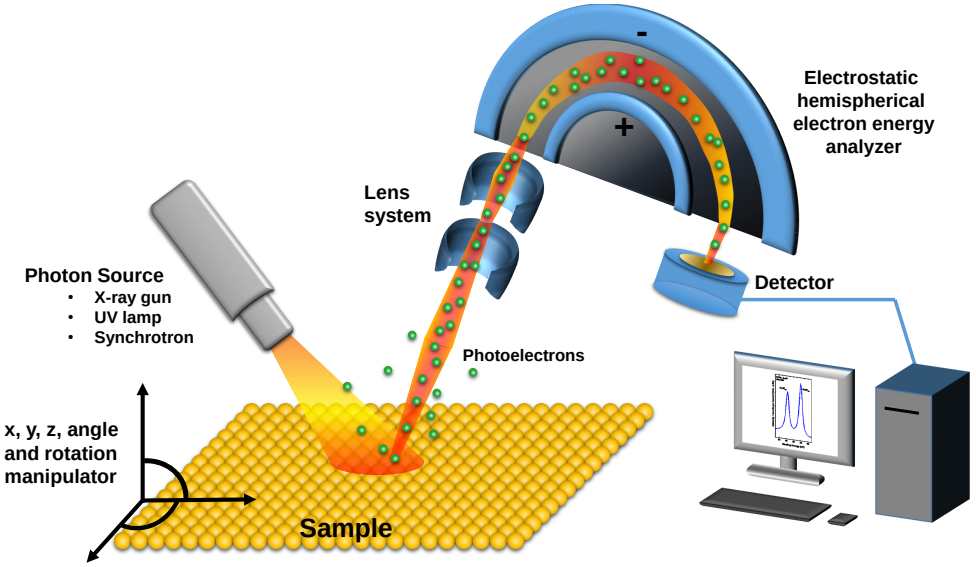

Figure 2.5.: Scheme of the XPS setup. The photons from the source produce photoelectrons, which are directed through a lens system to the analyzer. Electrons with a specific energy can pass the hemispherical analyzer and are measured by the detector. The sample can be moved in x, y and z direction by a manipulator. Also the angle and rotation can be changed.[121]

2.3.4. Synchrotron Radiation

Besides the above mentioned X-ray sources, other light sources can also be used for XPS. One of them, an efficient source for all different kinds of X-Ray applications, is a synchrotron X-Ray Source. Any acceleration of a charged particle causes emission of light. This feature is used by synchrotron accelerators, which accelerate electrons radially by using magnetic fields. The energy of the synchrotron radiation depends on the acceleration and the E_{kin} of the electrons. The photons are emitted tangential to the electron beam and can be used for spectroscopy at so-called beamlines. With the help of electromagnetic elements (e.g. undulators) the photon energy can be tuned to selected values. The selectable photon energy is one of the major advantages of a synchrotron source. Also the beam energy spreads less, which results in an improved energy resolution (0.1 eV or better). On the other hand, samples, especially organic samples, can be destroyed faster. The cost and availability of beamtime is another important aspect and possible limitation.[116,117]

2.3.5. Photoelectron Spectra

The resulting spectra in XPS are displayed in counts per second (intensity) versus E_B. In figure 2.6 the XPS spectrum of a hexadecane-1-thiol (HDT) SAM on gold is shown as an example. Figure 2.6a shows a widescan of the sample and a magnified inlet with a narrowscan of the sulfur region, exhibiting the S 2p peak. Figure 2.6b shows a narrow scan of the Au 4f region. The Au $4f_{7/2}$ peak is used as a reference at 84 eV. All s peaks (l = 0) are singlets and peaks of p, d and f levels are visible as doublets with a slightly different energy. XPS spectra can also contain Auger electron peaks beside the photoelectron peaks resulting from core level and valence band electrons. The phenomenon and nomenclature of Auger electrons was described in this section on page 12.

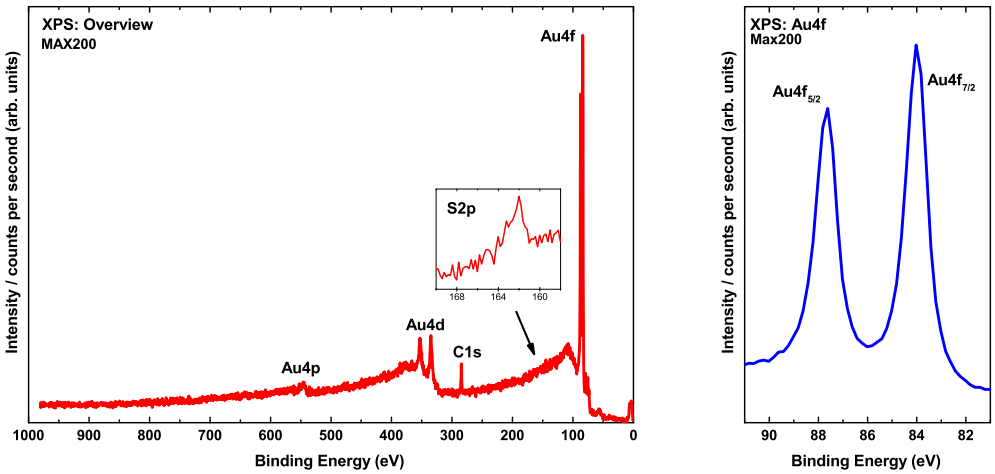

(a) (b)

Figure 2.6.: This figure shows two XPS spectra of a HDT SAM on Au(111) recorded with the MAX200 using its MgK_α X-Ray source. (a) shows a widescan over the whole scanrange with an inlet showing the magnified S 2p region as narrow scan and (b) shows a narrow scan of the Au 4f region. More detailed information about the MAX200 spectrometer and the measuring parameters, sample preparation and substrate details are provided in the experimental section 3.2

.

2.3.6. Chemical Shift

Any change in the chemical environment (oxidation state, change of influencing substituents, hybridisation) affects the energy of the photoelectrons and is therefore also visible in the spectral characteristics. This phenomenon is called

chemical shift and is the major interest in the application of XPS today. As an example one can compare two bound atoms with different electronegativities. In this case a charge transfer to the one atom with higher electronegatity takes place and the effective charge of the other atom becomes more positive, which increases its E_B and at the same time decreases the E_B of the first atom. Based on these observations and the resulting applications, XPS has also a second name: electron spectroscopy for chemical analysis (ESCA).

2.3.7. Quantitative Analysis

Besides the qualitative analysis, XPS is also suitable for quantitative analysis like the stoichiometric composition or the thickness of a film on a surface. In both cases, the intensity of the XPS signals are needed. To get the area of the peaks, the background has to be subtracted. There are different methods to do this, but subtractions of linear, Shirley-type or Tougaard backgrounds are most commonly used.[117,122,123] After background subtraction, the area of the peaks is calculated using a mixed Gaussian-Lorentzian or Voigt function to recreate the line shape of the XPS peaks.[117] Also the model of the inelastic mean free path (IMFP) has to be introduced. It is described as the distance a moving electron can travel between collisions, which can have influence on the electron energy or direction. According to the universal curve by Seah and Dench[117] the IMFP of electrons in solids is in the range of 10 Å to 30 Å for energies, which are relevant for XPS. The so called attenuation length (λ) of electrons adds a correction term that considers elastic scattering effects as well. It is an experimental value, which describes the distance where the intensity of a photoelectron has dropped to e^{-1} while travelling through material. This is also the limiting factor for the analysis depth which is up to 10 nm or $3 \cdot \lambda$. To calculate the λ in SAMs of alkanethiols on gold, the following formula with the empirical constans k and p is used:

$$\lambda = kE^p \tag{2.5}$$

With a radiation energy of the photon source in the range of 300 eV to 1000 eV, the constants in equation 2.5 are as follows:

$$\lambda = 0.3E^{0.64} \tag{2.6}$$

A list of attenuation lengths can be found in the literature.[124] To calculate the thickness of a SAM (d_{SAM}) on a gold substrate, one needs to look at the relation between the intensities of the emission lines of the substrate before (I^0_{Au}) and after (I_{Au}) assembly of the molecular film, as the intensity should be weakened by the film or any contamination.

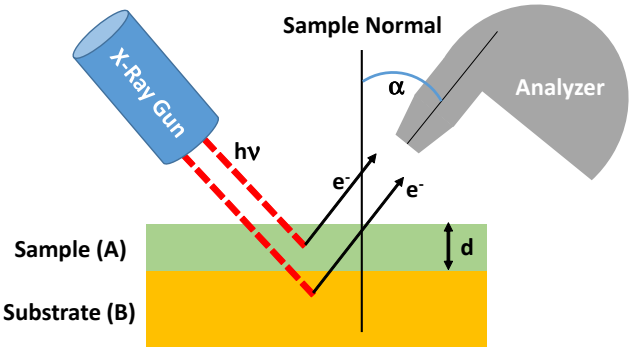

Figure 2.7.: Schematic drawing of the geometry for film thickness (d) calculation. The substrate B (e.g. Au) and a film A (e.g. SAM) are irradiated by photons ($h\nu$) from the X-ray gun. The electrons (e^-) from A and B are detected by the analyzer at the angle α to the sample surface normal. Equation 2.7 is used.[117]

$$\frac{I_{Au}}{I_{Au}^0} = exp\left[-\frac{d_{SAM}}{\lambda cos(\alpha)}\right] \tag{2.7}$$

with α as the angle between the analyzer and the surface normal and the attenuation length (λ) (compare with figure 2.7). The intensity I_{Au}^0 can also be obtained from a clean part of the substrate in the same measuring session. Another way to calculate the film thickness of a SAM is to use a reference SAM with known thickness (for example HDT on Au(111) with a thickness (d_{ref}) of 19.4 Å, calculated from alkyl chain length, inclination and Au−S distance).[91,125,126] In this case, the signal of the substrate I_{Au} and the intensity of the carbon signal I_C of the sample are needed:

$$\frac{I_C}{I_{Au}} = k\frac{1-(exp\frac{d_{SAM}}{\lambda_C})}{exp(\frac{d_{SAM}}{\lambda_{Au}})} \tag{2.8}$$

with k as an instrument specific constant containing the thickness d_{ref}:

$$k = \frac{I_C}{I_{Au}} \cdot \frac{1-(exp\frac{d_{ref}}{\lambda_C})}{exp(\frac{d_{ref}}{\lambda_{Au}})} \tag{2.9}$$

Rearrangement and calculation of the equations 2.7 or 2.8 will give the film thickness.[124] As mentioned, also the stoichiometric composition (N_A to N_B) of a sample containing A and B can be calculated:

$$\frac{N_A}{N_B} = \frac{I_A}{I_B} \cdot \frac{\lambda_B}{\lambda_A} \cdot \frac{\sigma_A}{\sigma_B} \tag{2.10}$$

with the intensity of the XPS peaks (I_A to I_B), the λ and the cross section (σ). With the above mentioned analysis, a sample can be characterized and described in detail.[116,117,127]

2.4. Near Edge X-Ray Absorption Fine Structure Spectroscopy

2.4.1. Basic Description

Near edge X-ray absorption fine structure (NEXAFS) spectroscopy is a valuable, highly surface sensitive method to investigate the electronic structure and also orientation of adsorbates (e.g. SAMs) on metal surfaces. NEXAFS is a synchrotron-based method, which brings the disadvantage that it can not be used with a standard laboratory X-ray source. The best results are achieved when probing light molecules like carbon, nitrogen, oxygen and fluorine using the soft X-ray region (100 eV to 700 eV). The X-ray adsorption edge describes the point, at which the energy of the X-ray photons is just enough to excite the electrons of a certain shell. Transitions from a deep core shell (mostly K shell) to unoccupied molecular orbitals are analyzed. NEXAFS spectra are usually recorded from just below the edge up to around 50 eV above. The step function (thick dashed line) in figure 2.8c describes the simplest case of a core level electron in the absence of any other empty electronic state, when scanning the photon energy and passing the ionization threshold. Before the ionization potential (IP) no absorption takes place and after the IP the core electron is excited. Figure 2.8a depicts a free single atom, which already has more final states than the simple model case mentioned above. Bound states (valence and Rydberg[130]), just below the IP, and unbound states (molecular antibonding), just above the IP. Figure 2.8b shows an energy scheme for a diatomic molecule with the according NEXAFS spectrum in figure 2.8c (solid black line). Empty molecular orbitals are marked by an asterisk (σ^* & π^*). The lowest unoccupied molecular orbital (LUMO) in an sp^3-C would be σ^*, which results in a broad resonance (C1s$\rightarrow$ σ^*). The transition C1s$\rightarrow$ π^* or a π^*-resonance is only observable in π-bonds, viz., double and triple bonds or in aromatic compounds. This transition shows a sharp resonance (figure 2.8c π^*). Transitions to the Rydberg orbitals, which are located between the π^*-resonance and the IP, result in sharp but weak resonances. Besides the resolution of the instrument, the lifetime of the excited state determines the peak broadening as well. Short lifetime results in sharp peaks. De-excitation can happen through Auger-transitions, fluorescence or falling back of the excited electron. As an easy rule, regarding the line shape of the spectrum, one can generally say that the higher

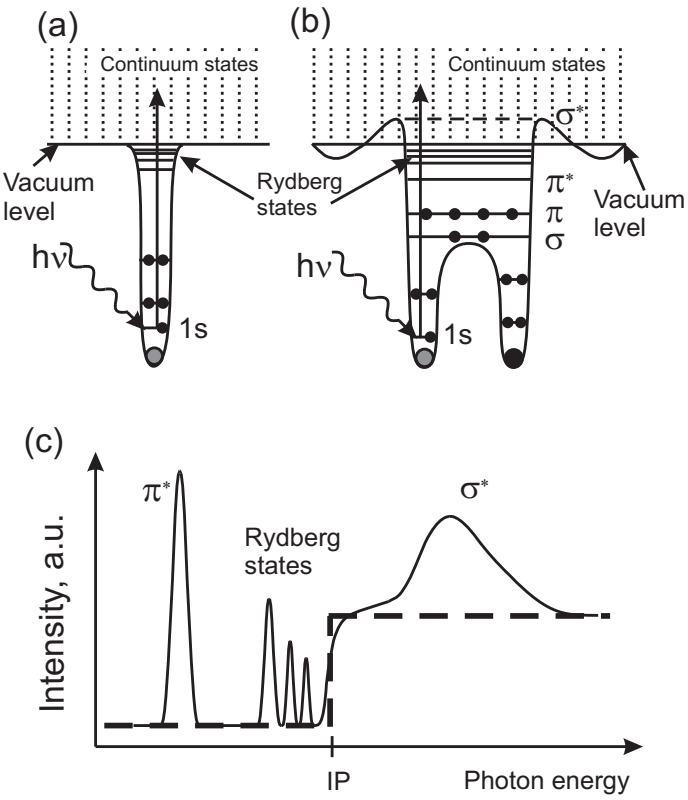

Figure 2.8.: (a) schematic potential for an atom and (b) schematic potential of a diatomic molecule. In addition to Rydberg states and a continuum of empty states similar to those expected for atoms, empty molecular orbitals are present, which are marked by an asterisk label (σ^* & π^*). Figure (c) shows a resulting absorption spectrum. The thick dashed line corresponds to the photoabsorption cross section of an electron located in a single bound state (core level).[128,129] From [128]. Reprinted with permisson of Springer.

a resonance lies in the continuum the larger is its linewidth. The NEXAFS spectroscopy takes the most information from π^*-resonance, and thus is most suitable for the analysis the according orbitals.[128,129]

2.4.2. Angular Dependence & Linear Dichroism Effect

As mentioned above, NEXAFS spectroscopy is suitable to determine the orientation of a molecule, precisely the molecular orbitals, in relation to the surface of the substrate. The orientation can be determined by relating the incidence angle (θ) of the (linearly polarized) synchrotron light to the intensity of the respective orbital resonance (see figure 2.9). The quantum mechanical descrip-

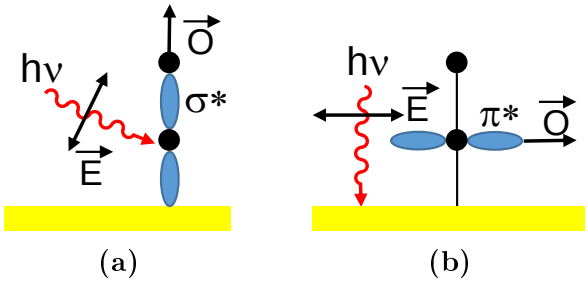

Figure 2.9.: Molecule adsorbed to a substrate with its molecular axis normal to the substrate. The electric field vector $\vec{E}$ and the direction of the final state orbital $\vec{O}$ overlap differently, which results in the following: (a) grazing incidence: the σ^* resonance is maximum; (b) normal incidence: the π^* resonance is maximum. Adapted from [128].

tion, relating the photoabsorption cross section σ_x to the initial and final state, Ψ_i and Ψ_f, respectively, for a single electron is as follows:

$$\sigma_x \propto |< \Psi_f \mid e \cdot p \mid \Psi_i >|^2 \, \rho_f(E) \tag{2.11}$$

with unit electric field vector e and dipole transition operator p and $\rho_f(E)$ as the density of final states.[128,129] For linearly polarized light, the expression $< \Psi_f \mid p \mid \Psi_i >$ is know as transition dipole moment (TDM). The following equation describes the transition intensity for a initial state (1s) and a directional final state (matrix element $\mid e < \Psi_f \mid p \mid \Psi_{1s} >|^2$ points in the direction of the final state orbital O):

$$I \propto | \, e < \Psi_f \mid p \mid \Psi_{1s} >|^2 \propto | \, e \cdot O \, |^2 \propto cos^2\delta \tag{2.12}$$

with δ as the angle between the TDM direction and the electric field vector E. This relationship shows that the intensity is the largest, when the direction of the final state orbital O (or the direction of the TDM) and the direction of the electric field vector E are the same (see figure 2.9). The π^* resonance, as the most pronounced one, is suitable for for the analysis of angular dependence.

The simple equation to determine the molecular orientation relates the average intensities of the measurements of the resonance to the direction of the TDM (α), the incident angle (θ) and the polarization (P) of the synchrotron light:

$$I \propto P \cos^2\theta (\cos^2\alpha + \frac{1}{2P} \tan^2\theta \sin^2\alpha) \tag{2.13}$$

From this relationship, the so-called *magic* angle of $\theta = arctan(\sqrt{2P})$ =55° with $P \approx 1$ can also be understood. At this incidence angle, the absorption

intensity does not depend on the molecular orientation. This incidence angle is used to acquire orientation independent spectra or spectra of samples with *unordered* molecules. These NEXAFS spectra contain only information about the electronic structure of the surface film.

For aromatic molecules, the TDM orientation (α) of the π^* orbitals of the phenyl rings is directly related to the tilt angle (β) of the molecular backbone:[35]

$$\cos(\alpha) = \sin(\beta)\cos(\gamma) \tag{2.14}$$

For the twist angle γ, a typical value for aromatic systems would be 32°.[131] As mentioned above, at an incidence angle of 55° no orientational effects influence the spectrum. On the other hand, a difference of two spectra, acquired at 90° (normal incidence) and 20° (grazing incidence) results in a fingerprint spectrum of the molecular orientation, known as the linear dichroism. Taking into account that $cos(90°) = 0$ and $cos(20°) \approx 1$:

$$I(90°) - I(20°) \propto (\frac{3}{2} sin^2\alpha - 1) \tag{2.15}$$

When α is small (angle between the electic field vector E and the averaged TDM direction), it results in a negative spectrum and for $\alpha \geq$55° the spectrum is positive.[128] This difference spectrum shows the orientational order at first sight. For molecules with a π^* resonance (double or triple bonds in the molecular plane) a negative spectrum signifies a planar orientation and a positive spectrum an upright orientation. For the σ^* resonances it is the other way round, as the two orbitals are perpendicular to each other.

2.5. Charge Transfer in Molecular Systems

Charge transfer processes on the nanoscale (1 nm to 100 nm) are currently being investigated with large interest. There is a lot of literature focussing on conduction mechanisms[16,132–134] and charge transport[135–143] in SAMs. Two well-established mechanisms are *tunneling* and *hopping*, which will be described in the following paragraphs.

Tunneling

In saturated alkyl SAMs the most common charge transport mechanism is non resonant tunneling.[144–151] Looking at SAMs with a conjugated π-system, near-resonant tunneling can take place, as the HOMO-LUMO gap is comparably small (∼3 eV).[11,152–154] The gaps of σ-saturated molecules are 6 eV to 8 eV.[13,136,155,156] To understand the easiest way of tunneling, the used model describes a finite potential barrier at the interface (metal-insulator) and the

finite probability that electrons can overcome the short distance into the SAM, although energy levels are missing. The tunneling model is described by:

$$J(d) = J_0 exp(-\beta d) \tag{2.16}$$

with the leakage current density J, the low field conductivity J_0, the thickness of the SAM (insulator) d and the tunneling decay parameter β,[157] described by:

$$\beta = \frac{4\pi(2m\phi)^{1/2}}{h}\alpha \tag{2.17}$$

with the electron mass (m), Planck's constant (h), the tunneling barrier (ϕ) and the unitless constant α describing the shape of the potential profile (α=1 for a rectangular barrier). The value of β is around 0.2 $Å^{-1}$ to 0.6 $Å^{-1}$ for π-conjugated systems and 0.6 $Å^{-1}$ to 1.2 $Å^{-1}$ for σ-saturated ones.[137] The following equation (Simmons relation) describes a simple process with a rectangular tunneling barrier, showing the exponential dependence of the current density (J_{DT}) on the thickness (d) and the barrier height (ϕ):

$$J_{DT} = \frac{p^2 V}{h^2 d}(2m^*\phi)^{1/2} exp\left(\frac{-4\pi d}{h}(2m^*\phi)^{1/2}\right) \tag{2.18}$$

with electron charge (q) and the applied voltage (V). If the tunneling barrier changes to a rectangular shape (the case for very high voltages above ϕ), the Fowler-Nordheim equation is valid:

$$J_{FN} = \frac{q^3 E^2}{16\pi^2 \hbar m^* \phi_{FN}} exp\left(-\frac{4\sqrt{2m^*}}{3q\hbar E}(\phi_{FN})^{3/2}\right) \tag{2.19}$$

with the tunneling barrier height ϕ_{FN} and the electric field E. The Fowler-Nordheim emission is independent of the temperature, but shows a high dependence on the applied voltage.

Hopping

Simple hopping follows the classical Arrhenius relation:

$$\sigma = \sigma_0 exp\left(\frac{-E_a}{kT}\right) \tag{2.20}$$

with the conductivity σ ($\sigma = J/E$ and $E = V/d$), the Boltzmann constant (k) and the activation energy (E_a). Hopping is more dominant in thicker layers and refers to ohmic transport. It is rarely observed in SAMs, as the investigated molecules generally form a layer with a thickness of ~2 nm.[147,158,159] A clear length-dependent transition between tunneling and hopping has been shown

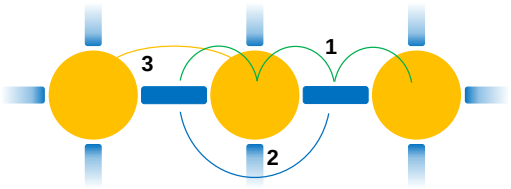

Figure 2.10.: Hopping processes described at the example of MOF systems with guest molecules. Possible first-order (Arrhenius type) transfer processes (solid lines) in a MOF-guest system are the subsequent hopping between guest and MOF sites (1) and the direct transfer between guest-guest or MOF-MOF sites (2,3). Adapted from [168].

in theoretical work,[140,160–162] some organics[163,164] and DNA.[140,165] The study in [166] showed the transition from tunneling to hopping for Au-molecule-Au junctions. Oligophenyleneimine molecules longer than 4 nm exhibit hopping transport and molecules shorter than 4 nm tunneling.[167]

In figure 2.10 the numbers 1,2, and 3 describe first-order hopping mechanisms for the example of a loaded MOFs. One theoretical description of this kind of charge transfer, describing the rate of hopping events between two weakly coupled sites a and b, is the Marcus theory.[169] The rate is given by

$$\Gamma_{a,b} = \frac{2\pi}{\hbar}|J_{a,b}|^2(4\pi\lambda k_B T)^{1/2} exp\left(-\frac{(\Delta E_{a,b}+\lambda)^2}{4\lambda k_B T}\right) \tag{2.21}$$

with $J_{a,b}$ as the electronic coupling matrix element between the initial and the final states; $\Delta E_{a,b}$ as the difference between the energy levels of the molecular orbitals; the reorganization energy λ; k_B is the Boltzmann constant, T the temperature and $\hbar$ the reduced Planck constant.

3. Experimental

In this chapter the preparation methods of the monomolecular films and metal-organic frameworks are presented along with the experimental methods used to characterize their structural and charge transfer properties.

3.1. Materials & Preparationroutes

3.1.1. Substrates

For all samples gold substrates purchased from Georg Albert PVD Germany were used. Onto a polished single-crystal Si(100) wafer, primed with an either 9 nm or 5 nm titanium adhesion layer, either 30 nm, 100 nm or 200 nm of gold (purity 99.99%) was deposited by PVD. The resulting substrate is polycrystalline, with a predominant Au(111) orientation and a roughness <5 Å. The particular substrate will be mentioned in the preparation.

3.1.2. SAM Precursors and SAM Preparation

All compounds used to prepare molecular films and SAMs were either bought or synthesized by one of our partner groups. A suitable acronym was assigned to each system. All molecular structures were drawn with ChemDraw.[104]

Nitrile-Naphthalenethiols and -selenols

The molecules, along with their assigned acronyms, are summarized in figure 3.1. The following compounds were synthesized by the group of Prof. Andreas Terfort from the Frankfurt University, Germany: 6-cyanonaphthalene-2-thiol (NC-NapSH), 6-cyanonaphthalene-2-selenoacetate (NC-NapSeAc), 4′-cyanobiphenyl-4-thiol (NC-BPT) and 4″-cyanoterphenyl-4-thiol (NC-TPT).[35]

The two SAM precursor naphthalene-2-thiol (NapSH) and hexadecane-1-thiol (HDT) were purchased from Sigma-Aldrich and used as received.

To form SAM films from NC-NapSH and NC-NapSeAc, a freshly prepared 200 nm gold substrate with a 5 nm titanium adhesion layer was immersed in a 1 mM solution of the respective compound in absolute EtOH for 24 h at room temperature (RT) (21 °C) or at elevated temperature (60 °C). After immersion,

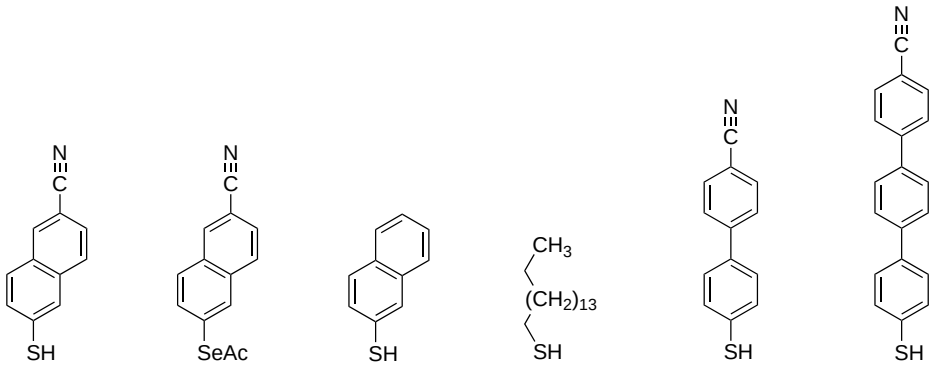

Figure 3.1.: Structures of the molecules along with their assigned acronyms. (a) NC-NapSH; (b) NC-NapSeAc; (c) NapSH; (d) HDT; (e) NC-BPT; (f) NC-TPT.

the SAM samples were carefully rinsed with EtOH and dried with argon. Films of NapSH and HDT were prepared in the same fashion at RT.

The reference SAMs NC-BPT and NC-TPT were prepared according to an established procedure[36,38] by immersion in a 1 mM solution of the compound in toluene for 24 h at RT. Afterwards the samples were rinsed with toluene and EtOH and residues blown off with argon. All samples were either characterized immediately or kept in argon-filled containers until the characterization at the synchrotron a few days after preparation.

Nitrile-Anthracenethiols and -selenols

The SAM precursors with an anthracene backbone, 6-cyanoanthracene-2-thiol (NC-AntSH) and 6-cyanoanthracene-2-selenoacetate (NC-AntSeAc), shown in figure 3.2 were synthesized by the group of Prof. Andreas Terfort, Frankfurt University, Germany.

The SAMs were prepared by immersion of a 30 nm gold substrate, primed with a 9 nm titanium adhesion layer in a 0.7 mM ethanolic solution of the respective compound for 24 h at RT. Afterwards the sample containers were put into an ultrasonic bath for 10 s, the samples taken out and rinsed with absolute EtOH. Residual EtOH was blown off with argon and the samples were stored in argon filled containers till they were measured at the synchrotron facility.

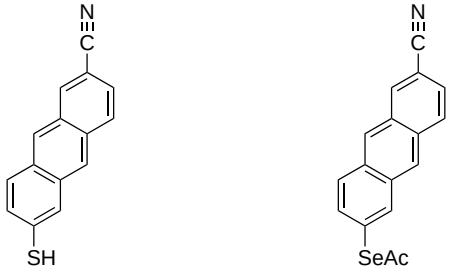

(a) (b)

Figure 3.2.: Structures of the molecules along with their assigned acronyms. (a) NC-AntSH; (b) NC-AntSeAc.

Nitrile-Azulenethiol

The SAM precursors for this project, azulene-2-thiol (AzuSH) and 6-cyanoazulene-2-thiol (NC-AzuSH), were synthesized by the group of Prof. Mikhail V. Barybin, University of Kansas, United States.

The SAMs were prepared by immersion of a 30 nm gold substrate, primed with a 9 nm titanium adhesion layer in a 1.5 mM solution of the respective compound in trichloromethane ($CHCl_3$) for 24 h at RT. Afterwards the samples were cleaned first with the solvent and subsequently with EtOH. Residues of the solvents were blown off with argon. The samples were stored in argon filled containers till they were measured at the synchrotron facility.

(a) (b)

Figure 3.3.: Structures of the molecules along with their assigned acronyms. (a) AzuSH; (b) NC-AzuSH.

Cyanide on Gold

For XPS, NEXAFS and resonant Auger electron spectroscopy (RAES) experiments, Au(111) on silicon was used as a substrate. The measurements were conducted at the BESSY II and Max IV facilities with independent sets of sam-

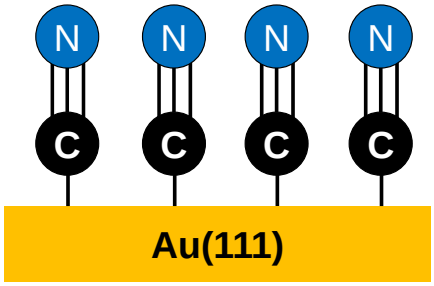

Figure 3.4.: Assumed scheme of cyanide attached to Au(111).

ples, prepared and shipped by the group of Prof. Paul S. Weiss, University of California, Los Angeles, United States.

Pyridinethiols

The pyridine molecules shown in figure 3.5 were synthesized by the group of Prof. Andreas Terfort, Frankfurt University, Germany.

The SAMs were prepared on a 30 nm gold substrate, primed with a 9 nm titanium adhesion layer. The precursors 4-(4-pyridyl)phenyl-1-methanethiol (PyrP1SH), 4-(4-pyridyl)phenyl-1-thiol (PyrP0SH) and 4′(4-pyridyl)biphenyl-4-methanethiol (PyrPP1SH) were immersed in ethanolic solutions with respective concentrations of 0.02, 0.015 and 0.02 mM to form a monolayer on the substrate. After 24 h at RT the samples were taken out and rinsed with absolute EtOH and blown dry with argon. Until measured at the synchrotron, the samples were kept under argon atmosphere.

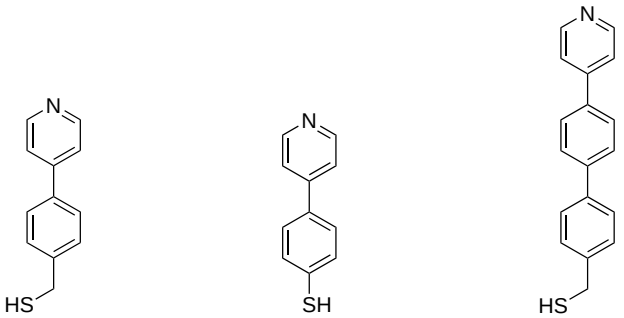

Figure 3.5.: Structure of the projects' molecules along with their assigned acronyms: (a) PyrP1SH; (b) PyrP0SH; (c) PyrPP1SH.

Nitro-Oligophenylthiols

The molecules ($HS-(C_6H_4)_n-NO_2$, short $nPT-NO_2$, shown in figure 3.6, used as precursors for the SAM preparation in this project, were either purchased from Sigma-Aldrich (4-nitrophenyl-1-thiol (PT-NO_2)) or synthesized (4′-nitro-biphenyl-4-thiol (BPT-NO_2) and 4″-nitroterphenyl-4-thiol (TPT-NO_2)) by P. Waske and N. Meyerbröker in our group.

To prepare the SAMs, fresh 100 nm gold substrates with a 5 nm titanium adhesion layer, were immersed for 72 h in a 2 mM ethanolic solution of the respective precursor at RT. Afterwards the films were rinsed with absolute EtOH and blown dry with argon. For reference measurements SAMs of dodecane-1-thiol (DDT) and octadecane-1-thiol (ODT) were prepared on similar gold substrates using the standard procedure.[170] The samples were stored under argon till they were measured at the synchrotron.

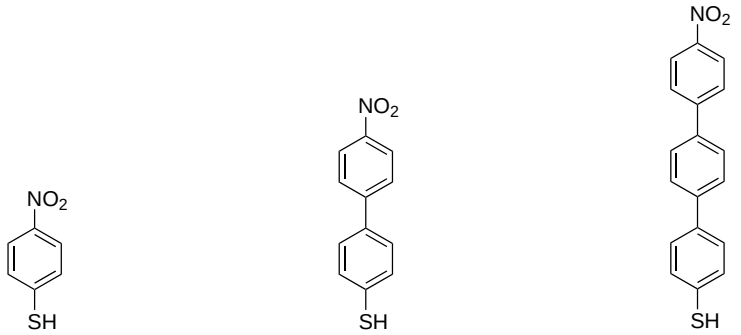

Figure 3.6.: Structures of the $nPT-NO_2$ molecules along with their assigned acronyms: (a) PT-NO_2; (b) BPT-NO_2; (c)TPT-NO_2.

3.1.3. Surface-Anchored Metal-Organic Frameworks

The preparation of the SURMOFs and the loading was done in the MOF-experienced group of Prof. Christof Wöll by Jianxi Liu, KIT, Eggenstein-Leopoldshafen in Germany by liquid phase epitaxy (LPE) using the spray method as described in the literature.[113]

3.1.3.1. Preparation of SURMOFs

For the SAM preparation, a 100 nm gold substrate with a 5 nm titanium adhesion layer, was immersed in a 20 µM ethanolic solution of 9-carboxy-10-(mercaptomethyl)triptycene thiol (CMMT) for 72 h in the dark at RT. Afterwards

the sample was rinsed with EtOH and blown dry with nitrogen. Directly after formation of the SAM, HKUST-1 SURMOFs were produced by LPE using the spray method reported in the literature.[113] Successively a 1 mM ethanolic solution of copper acetate and a 0.1 mM ethanolic solution of 1,3,5-benzene-tricarboxylic acid (BTC) were sprayed on the CMMT SAM on gold for 15 s. After a 25 s waiting time for crystallization to take place, the sample was cleaned with EtOH to remove excessive material. The spray cycles were repeated several times to produce HKUST-1 SURMOFs. By variation of the number of spray cycles, different thicknesses were obtained.

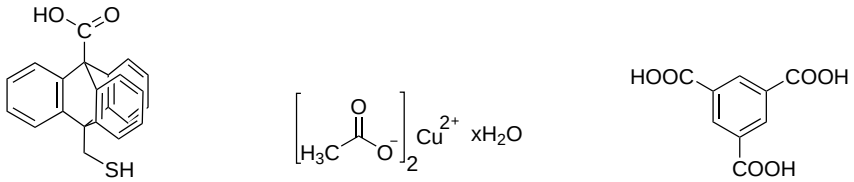

(a) (b) (c)

Figure 3.7.: (a) Shows the anchor molecule CMMT; (b) MOF SBU copper acetate monohydrate and (c) the organic linker BTC.

3.1.3.2. Loading of SURMOFs

The compounds, shown in figure 3.8, which were loaded into the pores of the SURMOF, were obtained from Sigma-Aldrich and used as received. To get rid of residual solvent molecules embedded into the framework, the SURMOF was heated to 60 °C in air for 20 min prior to loading.[76]

In the case of ferrocene (Fc) loading, the framework was exposed to its vapor for 72 h at RT.
In the case of 7,7,8,8-tetracyanoquinodimethane (TCNQ) and 2,3,5,6-tetrafluoro-7,7,8,8-tetracyanoquinodimethane (F4-TCNQ) loading, the samples were

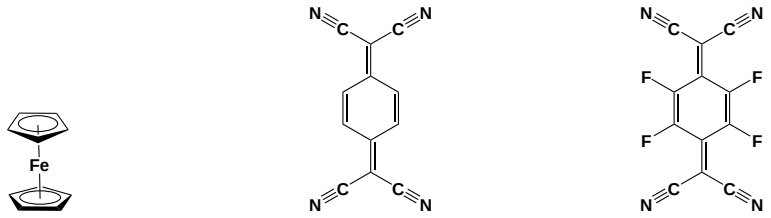

(a) (b) (c)

Figure 3.8.: (a) Ferrocene; (b) TCNQ; (c) F4-TCNQ.

immersed in the respective 2 mM ethanolic solution for 72 h and subsequently rinsed with EtOH and dried with nitrogen.

After synthesis, the samples were stored in absolute EtOH and dried with nitrogen before the measurements.

3.2. Characterization & Analysis

In this section, all used experimental setups and techniques along with the selected parameters are introduced. The analysis, processing of the data and the used calculation methods are also described.

3.2.1. XPS and HRXPS

3.2.1.1. Setups & Parameters

The XPS measurements were done in three different locations: MAX200 in Heidelberg, Germany; BESSY II in Berlin, Germany and MAX-IV laboratory in Lund, Sweden. The setups are described below.

MAX200

The laboratory-based XPS measurements were done with a MAX200 spectrometer (Leybold-Heraeus) with a hemispherical analyzer under UHV conditions at a pressure below 10^{-8} mbar. The magnesium X-ray anode used has its characteristic K_α line at an energy of 1253.6 eV. The acceleration voltage was set to 13 kV with an emission current of 13 mA. The number of scans per spectrum and the dwell time were adjusted to the measured region and intensity. The recorded spectra were normalized using a spectrometer specific transmission function to compensate for any energy dependent deviations of the analyzer and the detector.

BESSY II

Some of the synchrotron-based high resolution X-ray photoelectron spectroscopy (HRXPS) measurements were performed at the HE-SGM beamline (bending magnet) of the synchrotron storage ring BESSY II in Berlin, Germany, using a custom-made experimental station equipped with a Scienta R3000 electron energy analyzer and a partial electron yield (PEY) detector.[171] The synchrotron light served as the primary X-ray source. The spectra acquisition was carried out in normal emission geometry with an energy resolution of ~0.3 eV at an excitation energy of 350 eV and a little lower resolution at higher excitation

energies. The pressure during the experiments was in the low 10^{-10} mbar range all the time.

MAX IV

Some of the synchrotron-based HRXPS measurements were conducted at the MAX II storage ring at the MAX-IV laboratory in Lund, Sweden. The bending magnet beamline D1011 (plane grating monochromator) is equipped with a SCIENTA SES200 electron energy analyzer and a PEY detector. The energy resolution was below 100 meV (mostly 60 meV to 70 meV) and all experiments were carried out under UHV conditions at a pressure below 1.5×10^{-10} mbar.

3.2.1.2. Data Processing

The time to acquire a spectrum was kept as short as possible to reduce and possibly avoid damage to the samples by the primary X-rays.[172,173] Spectra were recorded in the Au 4f, C 1s, Se 3d, S 2p, N 1s, O 1s and F 1s regions, depending on the sample material. The photon energy (PE) ranged from 350 eV over 580 eV to 750 eV. For all recorded spectra, the E_B was referred to the $Au4f_{7/2}$ emission at 84 eV, measured at the same PE.[174] To process the data, the software *XPS Peak 4.1*[175] was used. A Shirley-type or linear background[122] was subtracted and the spectra were fitted using symmetric Voigt functions, if necessary. To fit the Se $3d_{5/2,\ 3/2}$ and S $2p_{3/2,\ 1/2}$ doublets, a pair of such peaks with the same FWHM values, branching ratios of 3:2 (Se $3d_{5/2,\ 3/2}$) and 2:1 (S $2p_{3/2,\ 1/2}$), and spin-orbit splittings (verified by fit) of ~0.86 eV (Se $3d_{5/2,\ 3/2}$) and ~1.18 eV (S $2p_{3/2,\ 1/2}$), were used.[174] Using the data from the resulting fits, the effective thickness and packing density of the sample monolayers were calculated. A well defined SAM on gold with known thickness served as the reference. The thickness was determined on the basis of the intensities of either the C 1s *and* the Au 4f signals *or* only the Au 4f signal, assuming a standard, exponential attenuation by the monomolecular film.[176] For the attenuation lengths reported in ref [124] a series of well-defined hydrocarbon films were used. For the reference-thickness of a HDT SAM, a value of 1.94 nm was used, which was estimated on the basis of the alkyl chain length (0.126 nm per CH_2 moiety),[91] molecular inclination (30° - 33.5°),[177] and Au−S distance (0.24 nm).[178] Other references like DDT or ODT were calculated in the same fashion. The packing densities were estimated from the intensity ratios of the S 2p and Au 4f emissions according to the approach reported in the literature.[179,180] Alkanethiol SAMs on Au(111) served as a reference system with a well-known packing density of 4.63×10^{14} molecules/cm^2 and 0.216 nm^2/molecule.[177]

3.2.2. NEXAFS Spectroscopy

3.2.2.1. Setups & Parameters

The NEXAFS spectroscopy measurements were also performed at the HE-SGM beamline of the synchrotron storage ring BESSY II and the D1011 beamline of the MAX II storage ring in the MAX-IV laboratories. Spectra acquisition was carried out at the carbon, nitrogen, oxygen or fluorine K-edges in the PEY mode with retarding voltages of −150 V, −300 V, −350 V, or −450 V respectively. Linearly polarized synchrotron light with a polarization factor of either ∼91% (BESSY II) or ∼95% (MAX II) was used as the primary X-ray source. The energy resolution was about 0.3 eV at BESSY II and below 100 mV at MAX II. The incidence angle of the light was varied from 90° (normal to the surface) to 20° (grazing incidence) in steps of 10° - 20°.

3.2.2.2. Data Processing

The raw NEXAFS spectra were normalized to the incident photon flux by division through a spectrum of a clean, freshly sputtered gold sample. Afterwards the spectra were reduced to the standard form by subtracting a linear pre-edge background and normalizing to the edge jump (determined by a nearly horizontal plateau 40 eV to 50 eV above the respective absorption edges). The PE scale was referenced to the pronounced π^* resonance of highly oriented pyrolytic graphite at 285.38 eV[181] in combination with the well-known $\Delta h\nu \propto (h\nu)^{3/2}$ behavior of plane grating monochromators.[182,183].

Generally two kinds of spectra are depicted: First, spectra, acquired at the so-called *magic* angle of X-ray incidence (55°). At his particular geometry the spectra are free of orientational effects and are representative of only the electronic structure of the studied systems.[184] Second, the difference between the spectra acquired at normal (90°) and grazing (20°) incidence of X-rays. This difference is representative of the so-called linear dichroism in X-ray absorption. Generally, the cross section of the resonant photoexcitation process depends on the orientation of the electric field vector of the linearly polarized synchrotron light with respect to the molecular orbital of interest.[184] Therefore, the intensity of characteristic absorption resonances exhibits a distinct dependence on the angle of X-ray incidence, if there is a preferable molecular orientation or an orientational order in the studied system. This can particularly be seen in the difference spectra. In addition, numerical information about the molecular orientation, averaged over the whole sample, can be derived from the entire NEXAFS data set within the standard theoretical framework.[184]

3.2.3. AES & RAES

3.2.3.1. Data Acquisition

The resonant Auger electron spectroscopy (RAES) measurements were also performed at the HE-SGM beamline of the synchrotron storage ring BESSY II in Berlin, Germany and at the D1011 beamline of the MAX-IV synchrotron radiation facility in Lund, Sweden. The spectra were acquired using either a Scienta R3000 electron energy analyzer (BESSY II) or a Scienta SES200 spectrometer (Max-IV). The X-ray incidence angle was set to 55° to suppress possible orientational effects[184,185] and the takeoff geometry of the electrons was close to normal emission. Resonant excitation was performed at the nitrogen K-edge and in the case where there is a nitro group at the oxygen K-edge. The excitation energies were determined in a preliminary NEXAFS experiment. The use of a plane grating monochromator at the respective beamline allowed the energy photon calibration at the N and O K-edges to be verified on the basis of the well-known $\Delta h\nu \propto (h\nu)^{3/2}$ behavior of such monochromators.[182] For excitation at the N K-edge, nonresonant decay spectra were recorded at ∼5 eV to 6 eV above the absorption edge, which appeared to be optimal for SAMs on gold to maximize the signal-to-noise ratio and to avoid the appearance of interfering gold photoemission in the spectra.[33,36–39,57] For excitation at the O K-edge, the nonresonant Auger spectra were recorded at either ∼8.5 eV or ∼15.5 eV above the absorption edge to avoid ambiguity related to a possible effect of additional resonant channels. Finally, for every sample, a reference spectrum for the pre-edge excitation was recorded.

3.2.3.2. Core Hole Clock Calculations

Background

The detailed calculation of the electron transfer (ET) time follows the core hole clock (CHC) method, introduced by Brühwiler et al.[27] and adapted for molecular films by A. Wee et al.[28] The further adaptation of this approach by our group,[27] relies on the resonant excitation of a core electron into a bound state of a specific functional group, weakly coupled to a continuum, and subsequent acquisition of the decay spectra. Figure 3.9 shows the basic core excitation and de-excitation routes and their respective spectral signatures for nitrile-substituted SAMs in the framework of RAES. After resonant excitation (**1**), and subsequent intershell transition (grey arrow), either the excited electron (**1a**; participator (P) route) or an electron from the occupied valence level (OV) can be emitted (**1b**; spectator (SP) route). Both of these routes result in different final states with characteristic spectral signatures. As an al-

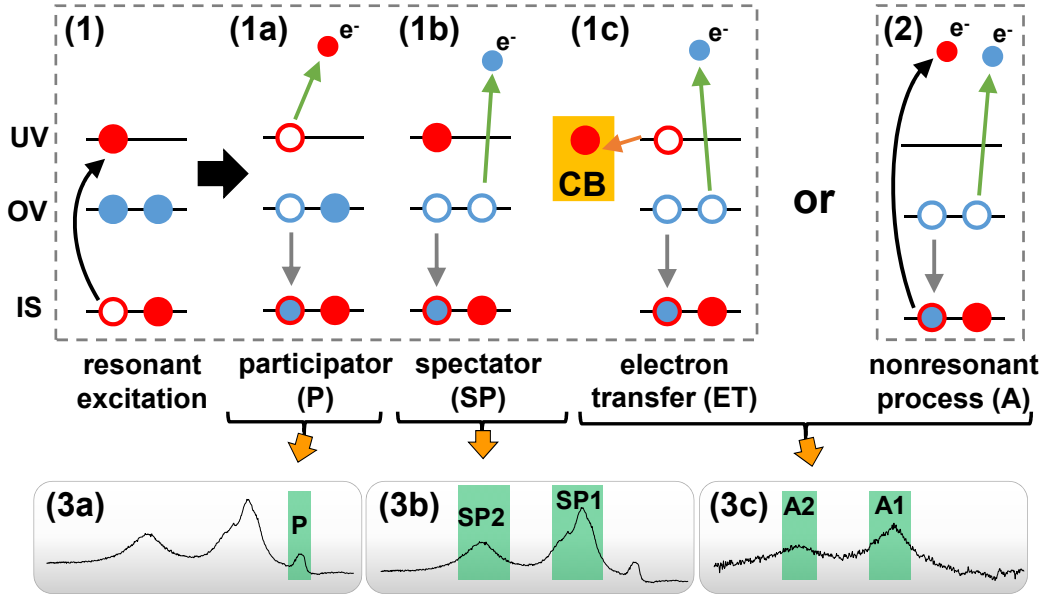

Figure 3.9.: The standard nonresonant Auger (A) process (2) and the scheme of de-excitation routes (1a-c) after resonant excitation (1) of a functional group (e.g. nitrile), weakly coupled to a continuum and the resulting final states and spectral signatures (3a-c) are shown. With IS, OV, and UV denote inner shell, occupied 2s- and unoccupied 2p-derived valence levels. Filled and hollow circles represent electrons and holes, respectively, with red and blue color-code corresponding to IS and OV/UV, respectively. (1) After the resonant excitation of an IS electron into a bound state (UV), the excited electron can either take part in the decay process (participator (P))(1a) or *watch* it as a spectator (SP) (1b). Both P and SP processes lead to characteristic final states with effectively one hole in the valence region and characteristic spectral signatures (3a and b - light green marker in the respective spectrum). Alternatively, ET (1c) of the excited electron to the CB can occur, resulting in a final state with two holes in OV, which is the nearly identical to the nonresonant Auger process (2), where a core electron is excited into a continuum state (curved arrow). (2) and (1c) show the same spectral signature (3c). The hole in IS is always filled by the electron transiting from OV.[27,186]

ternative route after resonant excitation, ET to the continuum can occur during the lifetime of the excited state. The continuum is mostly represented by the conductive substrate. The resulting final state and spectrum of this route (**1c**) is identical to the nonresonant Auger process (**2**). Each of the above routes can be considered as a one-step process.[185]

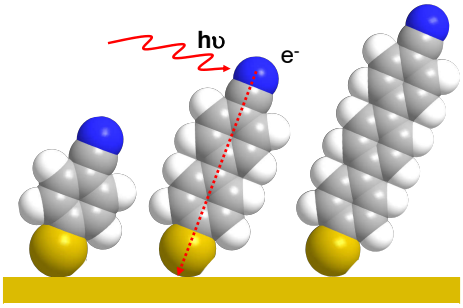

Figure 3.10.: Three molecules with different molecular length, but same general layout as an example, showing the unequivocally defined pathway of electron transfer (red dotted arrow) from the resonantly excited tail group to the substrate in the framework of RAES-CHC.[186]

Since all above final states are different, also in terms of charge, the features related to the respective scenarios can be distinguished in the joint RAE spectrum as far as the target group is clearly defined and the resonant excitation does not interfere too much with the contributions from other processes (e.g. photoemission) or other functional groups within the molecule.

The molecular design for investigation of electron transfer (ET) dynamics of SAMs is shown at the example of nitrile-substituted aromatic thiols in figure 3.10.[33,38] The molecules form SAMs on a gold substrate and within one series, all have the same layout with a head group (−SH), an aromatic backbone and a nitrile (−C≡N) tail group at the SAM-ambience interface. The electron pathway is unequivocally defined (red dotted arrow) by the molecular layout with the nitrile group, suitable for resonant electron excitation at the N K-edge. The only difference is the molecular length. The molecule on the right side (longest) is suitable as a reference. The RAES data from the reference sample can be seen as a pure resonant data, which only contains contributions from the SP and P decay routes. For the reference, ET can be either forbidden, which is the case when the E_B (derived from XPS data) of the respective core electron is higher than the π^*-resonance excitation energy (from NEXAFS data), or insignificant, which is the case when the molecular backbone is too long and the decay spectrum shows no perceptible amount of the ET route.[186–188]

Calculation Procedure

The raw data of the pre-edge, resonant and nonresonant spectra of the sample and the reference were imported into Matlab. After importing, the data was converted from E_{kin} to E_B using the respective excitation energy (E_{exc}), as shown in the following equation, which is the same as equation 2.2, explained

in the basics section:

$$E_B = E_{kin} - E_{exc} \tag{3.1}$$

After conversion, the spectra were shifted, if necessary, normalized and a Shirley-type background was subtracted. Afterwards the data of the pre-edge spectrum was subtracted from the resonant and nonresonant AES data to remove the contribution of photoemission, which could not be avoided completely. In the next step, the data of the resonant and nonresonant spectra was converted back to E_{kin} and a Shirley-type background was subtracted again. To find the amount of the ET contribution and calculate the ET time of the respective SAM, a reconstruction (figure 3.11; red line) of the sample decay spectrum (blue dashed line) was done, using the pure resonant spectrum of the reference (green line) and the nonresonant AES spectrum of the sample (black line). By slightly

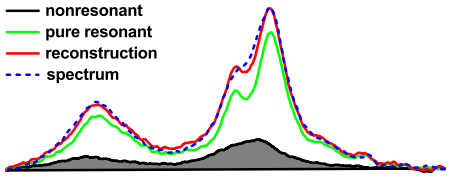

Figure 3.11.: Spectral decomposition on the example of NC-NapS/Au with the reference NC-TPT. The blue dashed line represents the decay spectrum of the sample. The red line shows the reconstruction of the line shape by combination of the nonresonant (black line) spectrum of the sample and the pure resonant (green line) spectrum of a reference sample. The grey filling represents the P_{ET} in the sample decay spectrum and is used for calculation of τ_{ET}. The results of this measurement will be presented and discussed in detail in chapter 4.

changing the relative contributions of the nonresonant and pure resonant to the reconstruction, the best fit was found and used to determine the portion of electron transfer events (P_{ET}), which is the relative intensity of the post-ET portion in the total decay spectrum of the sample (grey filling in the black line).

Using the following simple equation the electron transfer time (τ_{ET}) from the excited functional group to the substrate can be calculated from P_{ET}.[27,189–192]

$$\tau_{ET} = \tau_{core}(1 - P_{ET})/P_{ET} \tag{3.2}$$

The known lifetime of inner shell vacancy (τ_{core}) gives access to the fs-region and serves as an internal clock, giving also the name to the entire approach. The possible range for τ_{ET} is defined as follows: $0.1\tau_{core} < \tau_{ET} < 10 - 20\tau_{core}$. The value for τ_{core} depends on the excitated core shell and is 6.4 fs for N 1s.[32]

One possible case in the final data evaluation needs to be taken into account: it is generally not possible to distinguish between ET from the tail group to the substrate through the molecular backbone and ET to the backbone only, as in both cases the excited electron leaves the terminal excited tail group and results in the same final state as the Auger decay (see figure 3.9). However, for ET to the substrate, a length-dependence can be expected in the spectrum. This length dependence was reported for aliphatic and aromatic SAMs with a nitrile tail group (ET to the substrate through the molecular backbone).[37,38,186–188]

3.2.4. Two-Terminal Junction using Hg & EGaIn Electrodes

3.2.4.1. Setup

In two-terminal junction based measurements on SAMs and SURMOFs, the gold substrate is used as the bottom electrode and a passivated mercury-drop tip as the top electrode. Alternatively, eutectic gallium indium (EGaIn) (75.5wt% Ga and 24.5wt% In) tips were also tested successfully as a top electrode,[24] but only used in selected cases in this work.

The home-built tunneling junction setup described by literature[24] and shown in figure 3.12a was used for all measurements. In the case of mercury, a drop

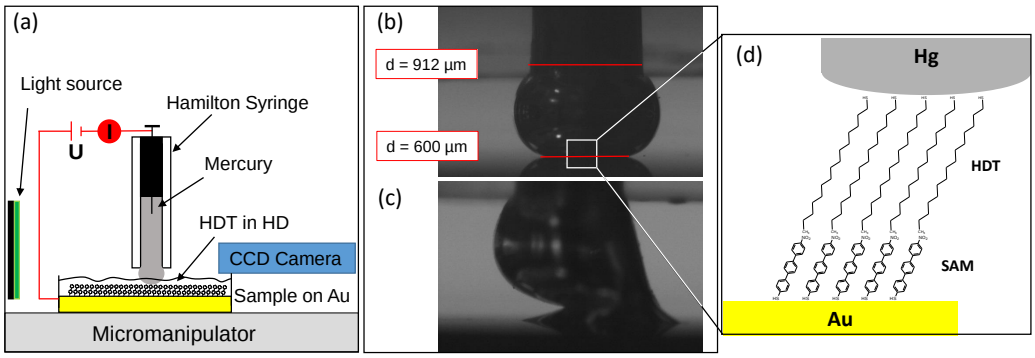

Figure 3.12.: (a) Schematically shows the home-build junction setup. A detailed description of the used parts can be found in the text. In (b) a mercury drop in contact with the sample surface and the according diameters of the syringe (top) and contact area (bottom) are shown. This view is recorded with the CCD camera, positioned as drawn in (a). If the mercury tip is approached too fast or the sample surface has defects, the drop breaks and amalgamates with the gold substrate (c). A close up of the schematic molecular junction (Hg/HDT//SAM/Au) is shown in (d).

was carefully pressed out of a gas-tight Hamilton syringe. The metallic core inside the syringe was connected to a Keithley 2635A sourcemeter. Prior to the measurement, the mercury drop was passivated by immersion in a 10 mM HDT solution in hexadecane (HD) for around 15 min. The sample was fixed in the measuring chamber using a metal clip held by a screw and connected to the sourcemeter. The passivated drop (see figure 3.12) was cautiously brought into contact with the sample (see figure 3.12d). To avoid destruction of the drop (see figure 3.12c), this approach was observed with a CMOS camera with a macro lens (The Imaging Source DMK22AUC03 1/3 in. Micron with MR 8/O), which was positioned perpendicular to the junction. The contact diameter, could be measured from this position, taking the syringe diameter as a reference (see figure 3.12b). Normally, the contact area was in the range of 600 µm to 800 µm. A variation in the pressure and therefore increasing contact diameter (up to 1000 µm) did not influence the results. The measured values increased slightly, but after the calculation, more or less pressure made no difference for the results. During the measurements, the junctions were stabilized by a 1 mM HDT solution in HD, which "repairs" SAM damages and thus decreases the risk of amalgamation.[193] The whole setup was placed on a vibration isolation table and put inside a home-built Faraday cage to reduce vibrations and electrical noise, respectively.

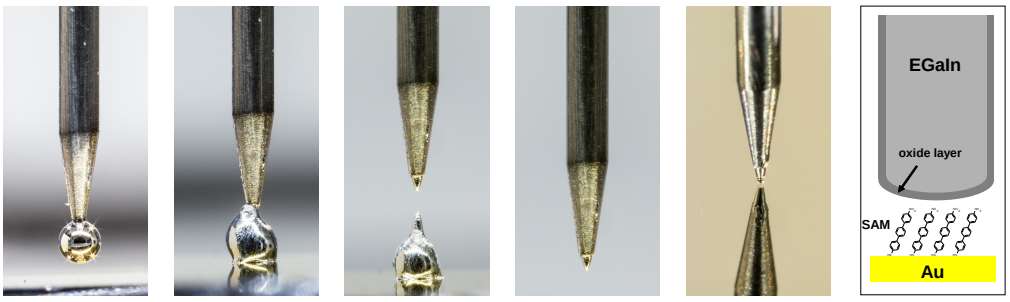

Figure 3.13.: The steps of the EGaIn tip formation are demonstrated: (a) Push EGaIn out of the syringe; (b) bring the drop in contact with the surface (Au in this case) until it sticks; (c) pull a sharp tip slowly out of the sticking drop; (d) wait a few minutes till the tip is passivated with the oxide layer (Ga_2O_3) and (e) bring the tip into contact with the sample and form a junction (the tip is reflected in the metallic surface). (f) A Schematic close up of the formed junction with the oxide layer around the tip. The pictures of the tip shown in this figure were taken in cooperation with Can Yildirim (PhD student, APC Heidelberg) and Peter Jeschka (technical staff, APC Heidelberg).[194]

To use the setup with an EGaIn tip,[194,195] only the syringe had to be changed to a Hamilton Autosampler Syringe 701ASRN and a small teflon adapter was used to modify the holder to accept the smaller syring. The EGaIn was carefully pushed out of the syringe and brought into contact with the sample surface. The formation of the tip and its self-passivation by forming a Ga_2O_3 oxide layer is shown in figure 3.13. The tip diameter was in the range of 40 µm to 70 µm, which is about 10% of the mercury drop. This means that the average contact area of the EGaIn to the substrate is less than 1% of the mercury contact area. For measurements with EGaIn no stabilizing solution is needed. The advantages and characterization of EGaIn can be found in the literature.[194,195]

All junctions form in the following way, depending on the tip material and sample. In the case of mercury: Hg/HDT//sample/Au in 1 mmol HDT in HD solution and in the case of EGaIn: EGaIn/Ga_2O_3//sample/Au.

3.2.4.2. Measurement of I-V Curves

For the experiments with the prepared SURMOFs and SAMs, the mercury drop or EGaIn tip was prepared as described above. The respective to be examined sample and the freshly passivated mercury drop or EGaIn tip were brought into contact. The junctions based on mercury are shown schematically in figure 3.12d. For EGaIn the junctions are similar and shown in figure 3.13f. To get statistical results, for each sample 5 different positions were measured, using more than one sample for each system. For each position, 5 to 10 current-voltage (I-V) curves were recorded. For bias voltages of 0.01 V to 0.5 V and −0.5 V to −0.01 V, 11 data points were collected, with an interval of 5 s between individual steps. Data resembling a metal-metal contact was eliminated (result of a broken drop, amalgamation or local sample defect). After relating the contact area to the measured current, the average of J (current density (A/cm^2)) was plotted vs the applied bias voltage (V) in a semilog plot. To evaluate the data and compare the systems to literature, the characteristic *tunneling decay constant* β can be obtained as a function of J using the exponential decay law introduced in section 2.5, adapted for the actual case:

$$J = J_0 e^{-\beta d_{El1,El2}} \tag{3.3}$$

where $d_{El1,El2}$ is the distance between the two electrodes El1 (Substrate) and El2 (Hg or EGaIn). The thickness is determined by the length of the molecules forming the SAM film. In the case of SURMOF-samples, the thickness was determined using atomic force microscopy (AFM). J_0 is the *theoretical* value for J at $d = 0$. The slope of a linear fit of Log J at 0.5 V vs the film thickness of three or more samples, corresponds to the decay factor β. A smaller β value indicates a better conductance of the sample. Values for β found in

the literature, obtained by the two-terminal junction method, are for instance $0.87\,\text{Å}^{-1}$ for alkanethiols[16] and $0.41\text{-}0.7\,\text{Å}^{-1}$ for oligophenyls[6,10,15,20,24] or go as low as $0.001\,\text{Å}^{-1}$ for molecular systems with integrated metal centers.[196]

4. Results & Discussion

Most of the results were either already published or are in preparation to be published. In each section the respective publications will be precisely cited. In addition, all publications are listed in the Appendix B.4. The publications were prepared in cooperation with our partners. The contributions of our collaborators are mentioned in the text and corresponding figures are presented in the Appendix A.

4.1. Electron Transfer in Monomolecular Films

In this section a the film quality of the monomolecular films is evaluated by a detailed XPS and NEXAFS analysis of each sample. Additional investigative methods are described in the subsections. Subsequently the electron transfer abilities are derived from the RAES data, following the CHC method, introduced by Bruhwiler et al.[27] (procedure described in section 3.2.3).

4.1.1. Nitrile-Naphthalenethiol and -selenol

The results presented in this subsection were published in *ACS Nano* and are adapted from [188]. Besides our analysis of the SAMs formed by the

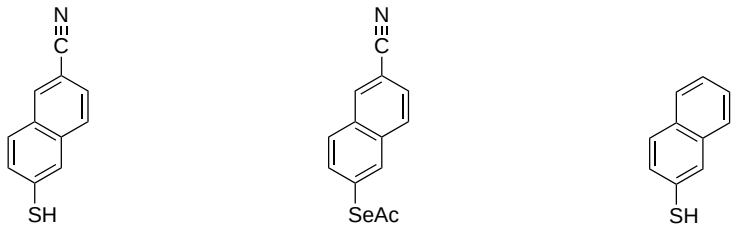

(a) **(b)** **(c)**

Figure 4.1.: Structures of the molecules along with their assigned acronyms. (a) NC-NapSH (b) NC-NapSeAc (c) NapSH

molecules in figure 4.1, the films were also investigated by our partner groups using scanning tunneling microscopy (STM) (Group of Prof. Peter Feulner,

Munich, Germany), Ellipsometry and infrared (IR)-spectroscopy (Group of Prof. Andreas Terfort, Frankfurt, Germany), water contact angle (WCA) and secondary ion mass spectrometry (SIMS) (Group of Prof. Piotr Cyganik, Krakow, Poland). Their findings were included in the discussion and the related figures can be found in Appendix A.

4.1.1.1. XPS and HRXPS

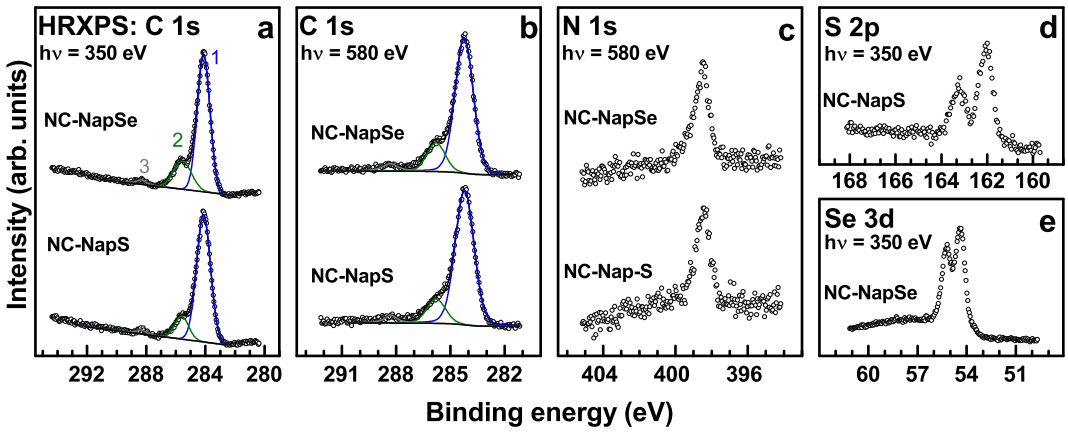

Figure 4.2.: C 1s (a,b), N 1 (c), S 2p (d) and Se 3d (e) HRXP spectra of the NC-NapS and NC-NapSe SAMs. The C 1s spectra are decomposed in individual emission viz. main peak (1; blue line), high E_B shoulder (2; olive line) and a low-intensity feature (3; gray line). The photon energies are given in the panels.

C 1s, N 1s, S 2p and Se 3d HRXP spectra of the NC-NapS and NC-NapSe films prepared at 60°C are presented in figure 4.2. They go in line with the formation of well-defined SAMs. The S 2p spectrum of NC-NapS/Au in figure 4.2d exhibits a distinct S $2p_{3/2,1/2}$ doublet at a binding energy (E_B) position of ∼162.0 eV (S $2p_{3/2}$) with no traces of atomic sulfur, disulfide, unbound thiol or oxidized species. This E_B value corresponds to the thiolate species bound to noble metal surfaces,[89,173,197] which suggests that basically all molecules in the NC-NapS films were anchored to the substrate via a thiolate-gold bond, as it should be the case for well-defined SAMs. Similarly the Se 3d spectrum of NC-NapSe/Au in figure 4.2e exhibits an exclusive Se $3d_{5/2,3/2}$ doublet at a E_B position of ∼54.25 eV (Se $3d_{5/2}$) characteristic of the selenolate species bound to noble metals surfaces.[40,102,173,198] This means that basically all molecules in the NC-NapSe films were anchored to the substrate via a selenolate-gold bond, forming well-defined SAMs.

The C 1s spectra of the NC-NapS and NC-NapSe monolayers in figure 4.2a and b exhibit an intense emission at a E_B of 284.15 eV (**1**) accompanied by a weak shoulder at higher E_B at 285.65 eV (**2**). The intense emission can be assigned to the naphthalene backbone, while the shoulder can be mainly associated with the nitrile carbon, similar to the case of nitrile-substituted oligophenylenes and oligophenylene ethynylenes.[36,57] In accordance with the assignment above, the relative intensity of the shoulder decreases with increasing photon energy as follows from comparison of figure 4.2a and b. This happens, because the larger inelastic mean free path (IMFP) at higher kinetic electron energies favors photoemission from the backbone (inner part of the sample) compared to that from the tail group (outer surface of the sample). This decrease is stronger for NC-NapSe/Au than for NC-NapS/Au, which is presumably related to an admixture of a weak signal from a minor contamination (CO) to the shoulder with a slightly higher contribution for NC-NapS/Au. Additionally there is a low-intensity feature at 288.3 eV (**3**), probably related to another minor contamination such as COOH. The contamination was most likely located at the SAM-substrate interface since its relative weight increased with increasing kinetic energy of the photoelectrons.

The N 1s spectra of the NC-NapS and NC-NapSe SAMs in figure 4.2c exhibit a single N 1s emission at a E_B of 398.5 eV. This emission can be assigned to the nitrogen atom of the nitrile group, similar to the analogous systems.[36,38,57] The presence of this single emission only suggests the same chemical state and location within the SAMs for all nitrile groups. Regarding the given molecular structure and the geometry of attachment to the gold via S or Se (S 2p and Se 3d discussion above), all nitrile groups are located at the SAM-ambience interface.

Besides the above analysis of the HRXP spectra, characteristic intensity relations were examined. The C 1s/Au 4f intensity ratio for the NC-NapSe SAM was found to be slightly higher than for the NC-NapS monolayer at both excitation energies used (350 eV and 580 eV). Accordingly the effective thickness of the former films (∼1.17 nm), calculated using the standard approach described in section 3.2.1.2,[199] was found to be slightly (by ∼11%) larger than that of the latter films (∼1.05 nm). This suggests a slightly higher packing density of the NC-NapSe SAMs as compared to the NC-NapS monolayers. This is in full agreement with the STM data of the SAMs, presented in figures A.1 and A.2 in the Appendix, which give a similar difference in the molecular footprint between NC-NapS/Au and NC-NapSe/Au. The calculated film thickness values are very close to the lengths of the NC-NapS and NC-NapSe precursors (1.12 nm and 1.14 nm, respectively), implying dense molecular packing in the monolayers. These findings were also verified by ellipsometry. The thick-

ness of the NC-NapS and NC-NapSe films were estimated at 1.03±0.08 nm and 1.19±0.04 nm, respectively.

4.1.1.2. NEXAFS Spectroscopy

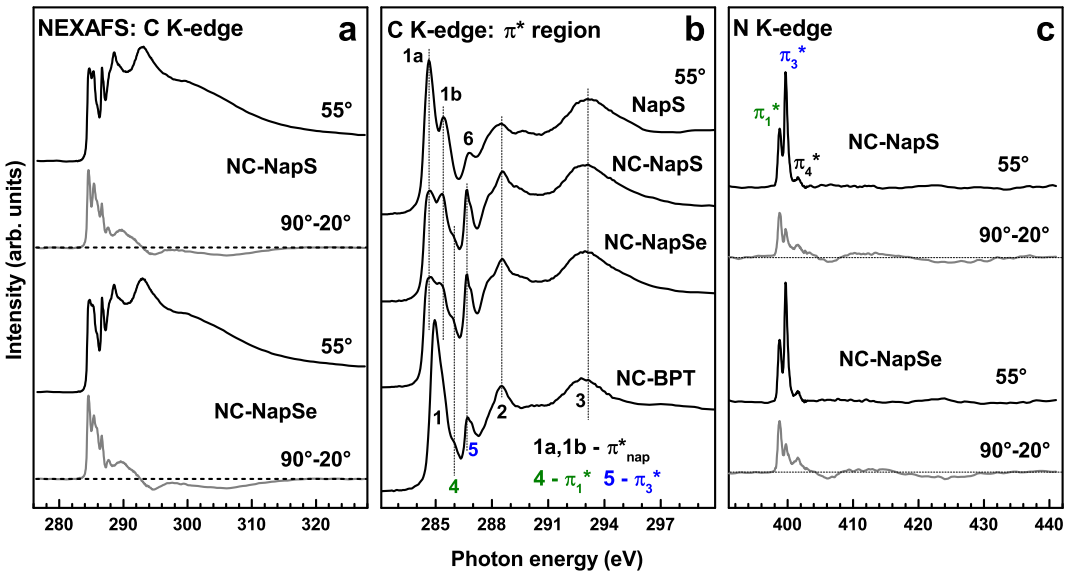

Figure 4.3.: C (a,b) and N (c) K-edge NEXAFS spectra of the NC-NapS and NC-NapSe SAMs acquired at an X-ray incident angle of 55° (black solid curves) along with the respective difference between the spectra collected under normal (90°) and grazing (20°) incidence geometry (gray solid curves in a and c). The horizontal dashed lines correspond to zero. In (b), the region of the π^* resonances is presented and additionally the spectra of several reference systems such as NapS and NC-BPT SAMs are given for comparison. Individual resonances in b and c are marked.

The C K-edge NEXAFS spectra of the NC-NapS and NC-NapSe SAMs are presented in figure 4.3a. This figure compiles the spectra acquired at an X-ray incidence angle of 55° as well as the difference between the spectra acquired at X-ray incidence angles of 90° and 20°. The angle of 55° is the so-called *magic* angle of X-ray incidence, at which the resulting spectrum is exclusively representative of the chemical identity of the sample and free of orientational effects of the molecule.[129] In contrast, the difference of the NEXAFS spectra acquired at 90° (normal incidence) and 20° (grazing incidence) is a fingerprint of the linear dichroism and therefore representative of the molecular orientation in the studied system (see section 2.4.2).

The spectra in figure 4.3a exhibit a variety of overlapping absorption resonances in the pre-edge area and in the vicinity of the absorption edge. To distinguish etwee individual resonances, this region is presented separately in figure 4.3b, along with the spectra of two reference systems, that is, SAMs of naphthalene-2-thiol (NapSH) and 4′-cyanobiphenyl-4-thiol (NC-BPT)[35,36] on Au(111). The spectrum of the NC-BPT film exhibits typical features of poly−p−phenylenes,[129,200–202] π_1* (**1**), π_2* (**2**) and σ_1* (**3**) resonances of the phenyl rings at 285.0 eV, 288.5 eV and 292.9 eV, respectively, along with the double π* resonance at 286.0 eV and 286.7 eV (**4** and **5**) associated with the terminal benzonitrile moiety.[36,38,57] The dominant π_1* resonance splits into two contributions (**1a** and **1b**), at 284.65 eV and 285.4 eV, when passing from the NC−BPT to the NapS monolayer. Such a splitting is typical for acenes[201,203–206] and is explained by the chemical shift of the two symmetry-independent carbon atoms.[204] Apart from this splitting and the lack of the benzonitrile-related resonances (**4** and **5**), the spectrum of the NapS film mimics that of the NC-BPT SAM, exhibiting the same resonances (**2** and **3**), along with a R*/C−S* resonance at 286.8 eV. According to their molecular structure, the spectra of NC-NapS and NC-NapSe SAMs exhibit resonances characteristic of nonsubstituted naphthalene (**1a**, **1b**, **2** and **3**) and benzonitrile (**4** and **5**). Distinct differences are a renormalization of the relative intensities of the **1a** and **1b** resonances and an increase in the relative intensity of the major benzonitrile-related feature (**5**). These changes can be tentatively explained by the conjugation between the π* systems of the nitrile moiety and naphthalene backbone, resulting in a redistribution of the electron density and, subsequently, in changes in the oscillator strengths of the involved electronic transitions.

The N K-edge NEXAFS spectra of the NC-NapS and NC-NapSe SAMs are presented in figure 4.3c. These spectra are dominated by a double π* resonance at ∼398.8 eV and ∼399.7 eV, accompanied by a weak feature at ∼401.7 eV (probably π_4* of nitrile)[207,208] and several hardly visible σ* resonances at higher PEs. The double π* resonance is characteristic of benzontrile and observed for the gas phase,[208] molecular solid[207] and monomolecular films containing this moiety.[36,38,57] The appearance of this resonance is related to the conjugation between the π* orbitals of the nitrile group and the adjacent phenyl ring. As a result, the degeneration of the π(C≡N*) orbital is lifted and it splits into two orbitals with distinctly different energies (in contrast to nitrile-substituted alkanethiols where the energies are quite close),[33,37,39] which are oriented either perpendicular (lower PE; π_1*) or parallel (higher PE; π_3*) to the plane of the adjacent ring,[207,208] as schematically shown in figure 4.4. The comparably lower intensity of the π_1* resonance can be explained by the delocalization of the respective orbital over the entire benzonitrile moiety, while π_3* is exclusively

localized at the nitrile group.

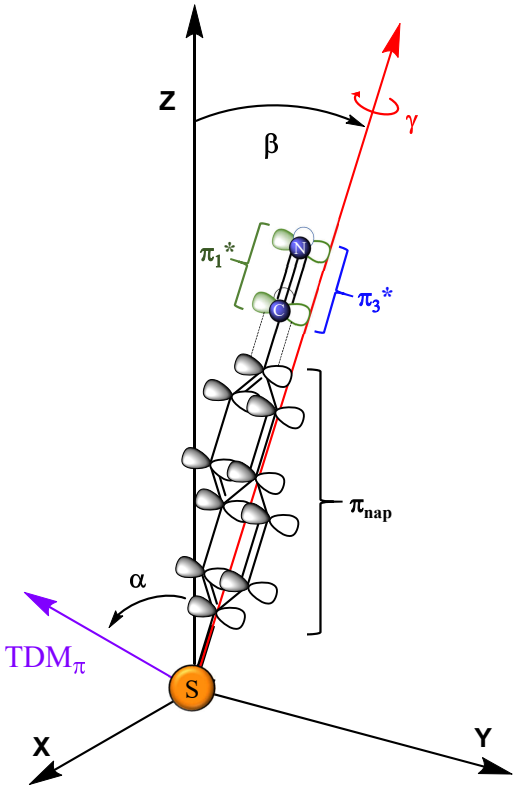

Figure 4.4.: Schematic drawing of the orientation of the NC-NapS and NC-NapSe molecules in the respective SAMs. The π_{nap}* orbitals of the naphthalene backbone (black) and the π_1* orbital of the nitrile group (green) are parallel to each other and perpendicular to the molecular plane; the respective transition dipole moment TDM_π is shown as a violet arrow, its orientation is given by the angle α. The π_3* orbital of the nitrile group (blue) is parallel to the molecular plane. The backbone tilt angle β and twist angle γ describe the molecular orientation. At $\gamma = 0$, TDM_π lies in the plane spanned by the z- and the molecular axis (red dashed line). Black, green and blue are used to color-code the respective resonances in figure 4.3b and c.

The C and N K-edge NEXAFS spectra of the NC-NapS and NC-NapSe SAMs exhibit pronounced linear dichroism as follows from the respective difference curves in figure 4.3a and c. Considering that the TDMs associated with the dominant π* resonances are oriented perpendicular to the molecular axis, the positive sign of the respective difference peaks suggests an upright orientation of the molecules in the SAMs. This qualitative conclusion goes in line with

the results from the IR-spectroscopy (see Appendix for the data in figure A.3). In contrary to the IR measurements, which is only qualitative, the exact twist and tilt angles of the molecules were obtained from the NEXAFS data. Within this procedure, performed within the standard theoretical framework for vector type molecular orbitals,[129,202] the average tilt angles of the most dominant π^* orbitals of the naphthalene backbone (**1a** and **1b**, see figure 4.3b) and the nitrile moiety (π_1^* and π_3^*, see figure 4.3c) were derived. The results are compiled in table 4.1, along with the analogous value for the reference NapS SAM. A schematic drawing of the target molecules, along with the relevant molecular orbitals and angles is presented in figure 4.4.

Table 4.1.: Average tilt angles of the π_{nap}^*(1 and 2) and $\pi_{1,3}^*$(NC) orbitals derived from the numerical evaluation of the NEXAFS data for the NC-NapS, NC-NapSe and NapS SAMs and the average molecular tilt and twist angles of the molecular backbone.[a]

average angles/system	NC-NapS	NC-NApSe	NapS
π^* orbitals (naphthalene) - α_{nap}	68°	67°	71°
π_1^* orbital (NC) - α_1	66°	67°	
π_3^* orbital (NC) - α_3	57°	57°	
twist angle (γ) from α_1 and α_3	52°	54°	
molecular tilt (β) from α_1 and α_3	43°	42°	
molecular tilt (β) from α_{nap} and γ	38°	41°	

[a] Error bars can be estimated at ±3°.

Based on the derived angle values for the NC-NapS and NC-NapSe SAMs the average tilt and twist angles for the molecular backbones in these monolayers were determined with the following equations within the established evaluation procedure.[35,36,57]

$$cos(\alpha_1) = sin(\beta)cos(\gamma) \tag{4.1}$$

$$cos(\alpha_3) = sin(\beta)cos(\pi/2 - \gamma) \tag{4.2}$$

$$cos(\alpha_{nap}) = sin(\beta)cos(\gamma) \tag{4.3}$$

The determination of the tilt and twist angle of the naphthalene backbones in the target SAMs was only possible due o the attachment of the nitrile tail groups and the alignment of the orthogonal π_1^* and π_3^* orbitals of this groups with the π_{nap}^* orbitals. Without this tail group, only the average orientation of the $TDM_{\pi*}$ can be determined. Subsequently the molecular tilt can be evaluated within an assumption regarding the value of the twist angle. Such an assumption, even though it is reasonable (indicated by other technique or

based on the data of the respective bulk signal),[209] is inferior to the direct determination of the twist angle, as done in the present case.

The derived tilt and twist values for NC-NapS and NC-NapSe SAMs are compiled in table 4.1. The values for the twist angle, calculated with equations 4.1 and 4.2 are very close to the analogous values derived with equation 4.3. This underlines the reliability of the approach - in view of the fact that the calculations were based on the independently determined values for the different building blocks of the target molecules, namely the naphthalene backbone and the nitrile group. According to table 4.1, the average tilt and twist angles of the molecular backbones in the NC-NapS and NCNapSe SAMs are similar, being $\sim$41° and $\sim$53°, respectively.

The relatively high tilt can be a consequence of the dipole-dipole interaction between the nitrile tail groups at the SAM-ambience interface. Minimization of this unfavourable interaction can be achieved by the tilting of the nitrile groups,[210,211] along with the rigidly bound naphthalene backbones. Note that the non-symmetrical attachment of these backbones to the thiolate and selenolate headgroups provides an additional rotational degree of freedom for the naphthalene unit,[131] similar to the case of anthracene-substituted alkanethiolates.[206] This permits a easy adoption of the most suitable orientation of the molecular backbones, depending on the balance of the structure-building interactions.

In agreement with the above mentioned hypothesis, the average tilt angle of the π^* orbital in the NapS monolayers is larger than those in the NC-NapS and NC-NapSe SAMs (see table 4.1). This suggests a smaller molecular inclination, even at the same twist angle as for the nitrile-substituted films. At a lower twist angle (25° for the respective bulk material), the molecular inclination is even smaller, being 22°, which is very close to the analogous value for the bulk naphthalene (20.5°).

4.1.1.3. AES and RAES

The electronic conductance in the NC-NapS and NC-NapSe SAMs was tested by RAES at the N K-edge within the CHC approach. The HRXPS and NEXAFS data has shown unequivocally that the nitrile groups were exclusively located at the SAM-ambience interface, being electronically connected to the substrate through the molecular framework. Thus, the ET pathway to the substrate at the resonant excitation of the nitrile group was well-defined. Nevertheless, ET could only occur, if it was energetically allowed. For efficient electron transport, the energy of the π^* resonantly excited electron at the nitrile group should be positive with respect to the Fermi level (E_F) of the substrate. Accordingly, the π^* resonance excitation energy should be higher than the E_B of the respective

core electron. Luckily, in the case of the NC-NapS and NC-NapSe SAMs, this condition is fulfilled for both orbitals, the π_1* and π_3*. The respective adsorption energies (∼399.7 eV and ∼398.8 eV) are higher than the N 1s E_B (398.5 eV). Thus, tail group to substrate transfer of the resonantly excited electron is energetically allowed for [N 1s]π_1* and [N 1s]π_3* excitations.

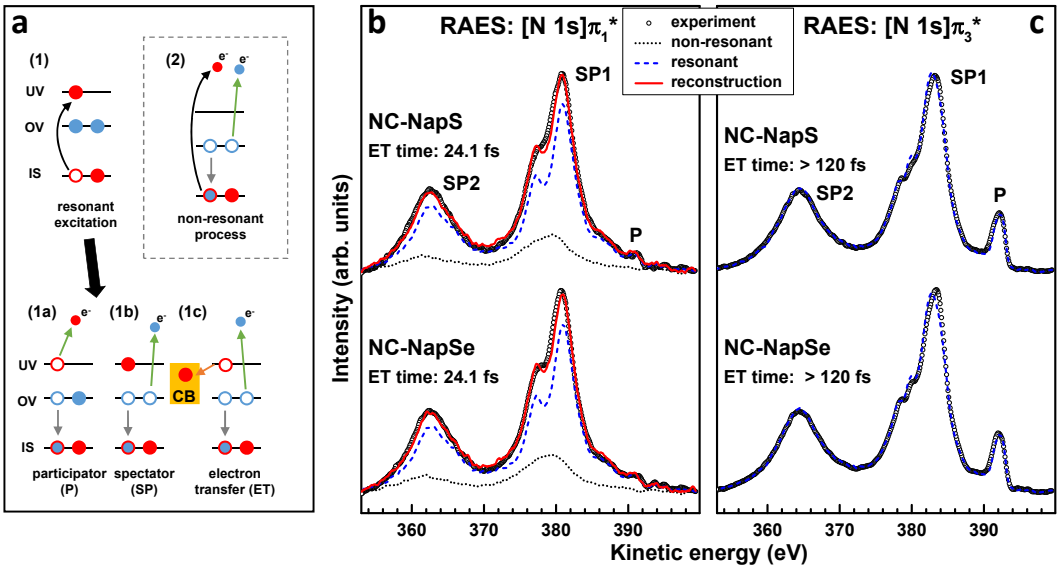

Figure 4.5.: (a) Scheme of core excitation/de-excitation routes for the nitrile group in the NC-NapS and NC-NapSe SAMs in the framework of RAES. This scheme was explained in the experimental part in figure 3.9 and is added just for the sake of completeness. [N 1s]π_1* (b) and [N 1s]π_3* (c) RAE spectra of the NC-NapS and NC-NapSe SAMs (open circles) along with their reconstructions (red solid lines in b) by the linear combination of the purely resonant (blue dashed lines) and non-resonant (black dotted lines in b) contributions. Participator (P) and spectator (SP) features are marked. The derived τ_{ET} values are given in the figures. The experimental and resonant spectra are almost identical in c, so that the nonresonant contribution is too small to be perceptible.

As shown in figure 4.5a and explained in the previous chapter on page 35 in figure 3.9, the decay of the excitation can occur in three possible ways, if radiative decay is neglected. Thes include, first and foremost, so-called participator (P) and spectator (SP) scenarios, resulting in final states with either one hole in the region of the occupied valence (OV) states, corresponding to the P process, or two holes in the OV states but an additional electron in the unoccupied valence (UV) states, which gives in integral one hole per excited atom

and corresponds to the SP process. Additionally, ET of the excited electron to the conduction band (CB) of the substrate can occur, followed by the standard Auger decay. This route leads to the final state with two holes in OV, which is nearly identical to the final state of the Auger decay in the case of nonresonant excitation, apart from subtle effects like alignment of the core hole or difference in vibrational fine structure.[185] Since all above final states are different, also in the terms of charge, the features related to the respective scenarios can be distinguished in the joint RAE spectrum as far as the target group is clearly defined and the resonant excitation does not interfere too much with the contributions from other processes (e.g. photoemission) or other functional groups within the molecule.

An important point is that one can generally not distinguish between ET to the substrate through the molecular backbone and ET to the backbone only in the CHC experiments involving a resonantly excitable tail group. In both cases the electron is not located at the terminal nitrile group any more, leading to the electronic configuration, which is nearly identical to the final Auger decay in the case of nonresonant excitation. However, for ET to the backbone only, no dependence on the length of the backbone can be expected, which is not the case for aliphatic and aromatic SAMs with the nitrile substitution.[37,38] This suggests, that we deal with ET to the substrate in the present case, supported also by the energetic considerations above.

[N 1s]π_1* and [N 1s]π_3* RAE spectra of the NC-NapS and NC-NapSe SAMs along with their reproductions by the linear combination of the purely resonant (P and SP) and non-resonant (ET) contributions are presented in figure 4.5b and c. The purely resonant contributions were measured using a 4″-cyanoterphenyl-4-thiol (NC-TPT) monolayer on Au(111) as a reference. This molecule has the same benzonitrile functional group as the NC-NapS and NC-NapSe moieties but is too long to have a perceptible ET contribution in the RAE spectrum.[38] The RAE spectra of NC-NapS and NC-NapSe exhibit both participator and spectator contributions, with a low spectral weight in the former component in the [N 1s]π_3* case. These spectra are very similar to the analogous spectra of other benzonitirle-terminated monomolecular films, which were analyzed in the literature.[36,38,57]

Analysis of the [N 1s]π_1* RAE spectra in figure 4.5b suggests that they contain considerable contributions from the ET route, represented as an admixture of the nonresonant spectrum to the pure resonant curves. Reconstruction of the RAE spectra by a linear combination of the nonresonant and pure resonant line shapes reproduces the experimental curves quite well, giving the identical portions of the nonresonant features (∼21%), representative of ET, for both the NC-NapS and NC-NapSe SAMs. Based on these values, we can apply the main

formula of the CHC approach (equation 3.2: $\tau_{ET} = \tau_{core}(1 - P_{ET})/P_{ET}$) with 6.4 fs[29] for the known lifetime of inner shell vacancy (τ_{core}) and the relative intensity (P_{ET}) of the post-ET portion in the total decay spectrum.[27,189–192] Accordingly, the derived τ_{ET} for both NC-NapS and NC-NapSe SAMs is 24±4 fs. As expected this characteristic time is longer than the analogous value for the monolayers of nitrile-substituted phenylthiolates (NC-PT; 9±3 fs)[38] but smaller than the value for the SAMs of NC-BPT (29±6 fs).[38] Most important is the fact that τ_{ET} is practically identical for the NC-NapS and NC-NapSe SAMs, differing by either thiolate or selenolate binding to the substrate.

In contrast to the [N 1s]π_1* data, the [N 1s]π_3* RAE spectra of the NC-NapS and NC-NapSe SAMs, presented in figure 4.5c, do not exhibit any perceptible admixture of the nonresonant line shape. These spectra are practically identical to the properly scaled pure resonant spectra. Probably the characteristic ET time following the [N 1s]π_3* excitation in the NC-NapS and NC-NapSe SAMs is much longer (above 120 fs to 150 fs) than the N 1s core hole lifetime and is therefore not resolvable within the applied CHC scheme. Note that the analogous situation occurs for the NC-BPT SAMs as well and is understandable in the case of the naphthalene backbone. The distinctly different τ_{ET} for the [N 1s]π_1* and [N 1s]π_3* excitations are a common phenomenon in benznitrile-substituted monolayers.[38] This difference was explained by the different conjugations of the relevant molecular orbitals.[38] As mentioned above, the π_1* orbital is strongly conjugated with the π* system of the adjacent phenyl ring, which makes the electron transport along the molecular backbone more efficient. In contrast, the π_3* orbital is almost exclusively located at the nitrile group, which can be associated with a longer ET pathway and an additional injection barrier.

4.1.1.4. Discussion

The discussion is started with a short summary of the basic characterization data for both systems studied, including the findings of our collaborators (corresponding data in the Appendix A).

When looking at the effect of the S→Se headgroup substitution (monitored via WCA; figure A.4a and b)[188] on the stability and transport properties of SAMs, it is not sufficient to use just the S- and Se-based molecular analogues, as it is fulfilled in a variety of previous publications[41,43,49,212] and also in the present case, but it needs also to be ensured that the respective SAMs formed by these analogues have similar structure and packing density, so that the relative stability and conductance data can be exclusively related to the SAM-Au(111) interface modification.

In the framework of these basic requirements, the STM analysis of our collaborators (see figures A.1 and A.2 in the Appendix)[188] demonstrates that

the NC-NapS and NC-NapSe SAMs prepared on Au(111) at slightly elevated solution temperature (60 °C) exhibit well-ordered oblique ($2\sqrt{3}\times\sqrt{37}$) and rectangular ($2 \times 1.5\sqrt{3}$) molecular arrangements, respectively. Importantly, both structures are characterized by similar (within ∼10%) packing densities. These conclusions, based on the *local* STM analysis, are fully consistent with the results obtained by *large area* techniques, such as ellipsometry, IRRAS (figure A.3 in the Appendix), XPS and NEXAFS spectroscopy, which show similar effective film thicknesses (∼10.5 Å and ∼11.7 Å) as well as basically identical average tilt (∼41°) and twist (∼53°) angles of the molecular backbones for both of the SAMs. Such consistency of the data obtained from the local and global techniques is crucial at this point, because all further analysis of the stability and transport properties of these SAMs is based on the global techniques, which sample a large area, averaging over possible structural defects.

Despite similar packing densities, the STM analysis of the NC-NapS and NC-NapSe SAMs on Au(111) also shows important structural differences. It can be assumed that, in analogy to similar systems,[43] the molecules in these SAMs adopt a structure which mimics the characteristic herringbone arrangement, known for crystalline naphthalene. For the NC-NapSe SAM, a simple rectangular ($2 \times 1.5\sqrt{3}$) unic cell, involving three different adsorption sites, was observed (see figure A.2e), which, whithin the precision of the STM measurements, corresponds directly to the molecular arrangement within the (001) plane of crystalline naphthalene. Formation of such a simple structure, close to that of crystalline naphthalene, implies that the NC-NapSe molecule are capable of achieving an optimal, single-crystal-like molecular arrangement, even at the comparatively stronger interaction with the substrate. A distinctly different situation occurs in the case of the NC-NapS SAM. Here, a slightly larger, oblique ($2\sqrt{3}\times\sqrt{37}$) is observed, which is fully commensurate with the Au(111) substrate, but is much more complex, exhibiting up to six different adsorption sites. As indicated in figure A.1e, it is still possible to fit the motif found within the (001) plane of crystalline naphthalene into the oblique ($2\sqrt{3}\times\sqrt{37}$) cell, but only relying on the average distances between the molecules inside this complex structure. These observations indicate that the intermolecular interactions in the NC-NapS SAMs are inferior to the molecule-substrate interface energetics, so that the structural template provided by the substrate is a dominant factor for the structure formation. Since the packing motif and the density for both types of SAMs are very similar, we can assume that the observed difference in balancing the impact of the intermolecular interactions and molecule-substrate interface energetics on the 2D structure formation is exclusively attributed to differences in the headgroup-substrate interaction.

To learn more about the energetic of the molecule-substrate interface in both

SAMs, our collaborators have conducted dedicated exchange and S-SIMS experiments, probing the relative stability of these SAMs (see figure A.4).[188] The experiments monitoring the exchange of the NC-NapS and NC-NapSe moieties in the respective SAMs on Au(111) with HDT molecules unambiguously demonstrated an almost complete exchange reaction for NC-NapS/Au(111) and a very small extent of this process, probably limited to the defect sites only, in the case of NC-NapSe/Au(111). Considering that (i) both SAMs have similar structure and packing density and that (ii) the exchange process requires the complete removal of a SAM constituent by cleaving its bond to the substrate, we conclude a higher stability of the Se−Au bond as compared to the S−Au bond in thes fully aromatic SAMs with either S or Se atoms directly attached to the aromatic backbones. Note, that the same conclusion was reached in a previous exchange experiment where the relative stability of two homologue series of biphenyl-substituted alkanethiolates and alkaneselenolates (BPnS(Se): $CH_3-(C_6H_4)_2-(CH_2)$n−S(Se), n=1-6) on Au(111) was compared.[47]. Thus, the present and previous[47] exchange experiments are complementary and show that, independent of the backbone character (aliphatic or aromatic), the Se−Au bond is more stable than the S−Au one in the analogous SAMs.

To analyze the difference in stability of the molecule-substrate interface in the NC-NapS and NC-NapSe monolayers more in detail, a novel approach was exploited based on the ion-induced desorption technique.[213,214] The resulting data (figure A.4c and d) shows that, while the ion-induced desorption of positive ions, associated with the complete molecule and following the breaking of the Au−S(Se), is much more efficient for the NC-NapS SAMs, the emission of the positive ions related to desulfurized(deselenized) fragments by breaking the S(Se)−C bond is more efficient for the NC-NapSe monolayers. Following a general logic as well as the argument provided in a recent S-SIMS publication,[213] we assume that a larger efficiency of ion-induced cleavage of a given chemical bond is related to a smaller bond energy. Consequently, the actual S-SIMS data indicates a higher stability of the Se−Au bond as compared to the S−Au one and at the same time a lower stability of the adjacent Se−C bond as compared to the S−C one. Such effect of reversed relative stability of these two consecutive chemical bonds (viz. Au−S(Se) and S(Se)−C) can be understood intuitively considering that the valence electrons of the same S(Se) atom are involved in bonding with both the Au substrate and the naphthalene moiety. A larger involvement of the valence electrons of the S(Se) atom in one of these chemical bonds should result in a smaller involvement of these electrons in the second bond and consequently the stability of the latter. As documented by recent studies on the model system of BPnS(Se)/Au(111),[213] this intuitive explanation is also consistent with density functional theory (DFT) calculations

of respective bond energies and molecular dynamics simulations of ion-induced desorption. A further hint is a comparison of thiolate-bonded molecules on Au, Ag and Cu. The C−S bond breaks more easily, as the sulfur-metal bond gets stronger.[215,216] Summarizing this part and taking into account the literature data for the BPnS(Se) monolayers,[213] we can conclude that, independent of the molecular backbone (aliphatic or aromatic), the Se−Au bond is more stable than the S−Au one with lower stability of the respective adjacent C−Se/C−S bond.

A reasonable question at this point is why, despite the stronger binding to the substrate in the case of the Se headgroup, the respective SAMs adopt a structure dictated mostly by the intermolecular interaction, with a very simple unit cell, which is very similar to the molecular arrangement in crystalline naphthalene. This unit ell involves different adsorption sites for the identical molecules (see figure A.2e), thus indicating a probably lower involvement of the molecule-substrate energetics into the 2D ordering. There are two possible explanations of this seeming contradiction. First, it can be the effect of a lower corrugation of the binding energy surface for selenolates on Au(111) as compared to thiolates,[47] which is not necessarily related to the bond strength, as it occurs for alkanethiolates that have a better mobility on Ag(111) compared to Au(111), in spite of the stronger bonding to the silver substrate.[217] Second, it can be an effect of the enhanced mobility of the gold atoms in the topmost layer of the substrate mediated by the strong bond to the adsorbate molecules in the case of the Se headgroup.[40,42,45] It is well-known that the mobility of the atoms in the topmost layer of the substrate increases with increasing strength of the molecule-substrate bond due to the reduced interaction of the surface atoms with the underlying layers of the substrate.[47] This can result in relaxation of the stress related to the formation of 2D incommensurate structure driven by the strong intermolecular interactions. The STM data for the NC-NapSe/Au do not exhibit any evidence for a surface reconstruction since the molecular film, as a whole, mimics the structure of the nonreconstructed substrate, except for the small difference in the dimensions of th eunit cells, probably related to a limited accuracy of the STM measurements. Nevertheless, we think that the STM data do not allow a clear distinction between the lower corrugation and surface reconstruction scenarios, both of which are probably important.

The final part of the experiments in this project was devoted to the analysis of the ET processes in the NC-NapS and NC-NapSe SAMs. According to the results of the dedicated RAES-CHC measurements, the characteristic electron transfer time (τ_{ET}) between the terminal nitrile group of the assembled NC-NapS(Se) molecules and the Au(111) substrate is essentially identical (24±4 fs) for both types of SAMs. This suggests very similar ET properties for the

S−Au and Se−Au bonds, even though the entire τ_{ET} is mostly determined by the molecular backbone, with the ET through the backbone being the rate-limiting step.[37,38] According to previous results,[37,38] the characteristic ET time for the S−Au bond is just 2.3 fs to 2.8 fs as far as one can disentangle this contribution from the performance of the entire molecule.[38] Thus, a certain difference between the ET performance of the S−Au and Se−Au bonds cannot bet excluded, but it is certainly much lower than the factor of ∼2.5 or even ∼10 in relation to the entire molecule as reported in the literature.[49,212] Note that this is the only way to deal with the charge transport/transfer properties of the S−Au and Se−Au bonds as to probe the respective molecular adsorbates as a whole and not just the S/Se−Au junction.

In the present case, the ET process is related to individual molecules and does not depend on the packing density, which however is quite close for the NC-NapS and NC-NapSe SAMs, excluding differences in the matrix effects. It is also of importance that these molecules are the constituents of well-defined monolayers with similar structural and geometrical parameters. Note also that there are only a very limited number of experimental reports,[49,212] which compare electron transport through SAMs based on sulfur and selenium analogues. These studies, reportin contradictory conclusions regarding either higher[212] or lower[49] conductance for the Se headgroup as compared to the S one, use similar approaches based on analyzing apparent height differences in the STM images obtained for mixed SAMs of both types. Apart from the basic limitations of th eapplied methodology and possible roleof defects, such mixed SAMs were certainly not as well-defined as the monolayers of the present study. Additional support comes from the most recent DFT calculations analyzing the influence of the S→Se headgroup substitution in biphenyl-based SAMs on gold (C_6H_5−C_6H_4−S(Se)/Au(111)).[50] These calculations show that gold substrate work function modification due to the SAM formation, as well as HOMO and LUMO level alignment, is essentially insensitive to the S→Se substitution, which is consistent with a similar ET efficiency observed for both types of SAMs in our experiments.

Following a recent line of arguments[218] connecting the overlap and involvement of the relevant electronic states with the strength of the S(Se)−Au bond, we get a link between the results of the experiments probing this bond strength (exchange and S-SIMS) with the conclusions regarding the ET properties of the SAM studied (RAES-CHC). Considering the higher stability of the Au−Se bond compared to the stability of Au−S, one would probably expect noticeable differences in the ET properties. This was not observed in our RAES-CHC experiments, but at the same time, is was demonstrated that the larger involvement of the headgroup atom in binding with the metal substrate occurs at the

expense of the decreased involvement in the binding with the neighbouring carbon atom. Since the tunneling process involves both C−S(Se) and S(Se)−Au bonds, we suppose that the better tunnelling conditions in the latter case are compensated by the worse tunnelling conditions in the former case. Thus, it looks as tough the S→Se substitution causes a redistribution of the electronic states at the Au−S−C interface, which, in average, does not change the total probability of charge carrier tunnelling.

4.1.2. Nitrile-Anthracenethiol and -selenol

The molecules, subject to the analysis of their SAMs in this section, are exhibited in figure 4.6. The respective spectroscopic analysis along with the electron transfer properties are investigated and discussed in this section.

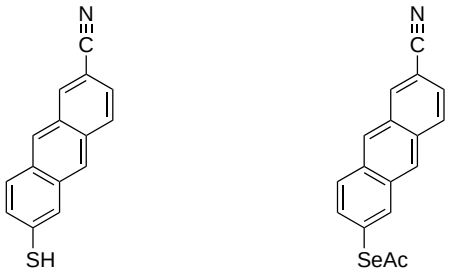

(a) (b)

Figure 4.6.: Structures of the molecules along with their assigned acronyms. (a) NC-AntSH (b) NC-AntSeAc

4.1.2.1. XPS and HRXPS

C 1s, N 1s, S 2p and Se 3d HRXP spectra of the NC-AntS and NC-AntSe films, prepared at 60 °C, are presented in figure 4.7. In general, the spectra go in line with the formation of well-defined SAMs. Besides the S $2p_{3/2,1/2}$ doublet (**1**) at a E_B of ∼162.0 eV (S $2p_{3/2}$) in figure 4.7d, corresponding to the thiolate species bound to a noble metal surface,[89,173,197] a small, but insignificant doublet shoulder at a E_B of ∼160.9 eV (S $2p_{3/2}$; **2**) is visible, which indicates a small amount of atomic sulfur.[219] These emissions indicate that not all, but nearly all molecules in the NC-AntS film are anchored to the surface via a thiolate-gold bond. The formation of the selenolate-gold bond, exhibited by the Se 3d spectrum in figure 4.7e, was slightly better and showed the expected single Se $3d_{5/2,3/2}$ doublet at a E_B position of ∼54.25 eV (Se $3d_{5/2}$). This position is characteristic for the

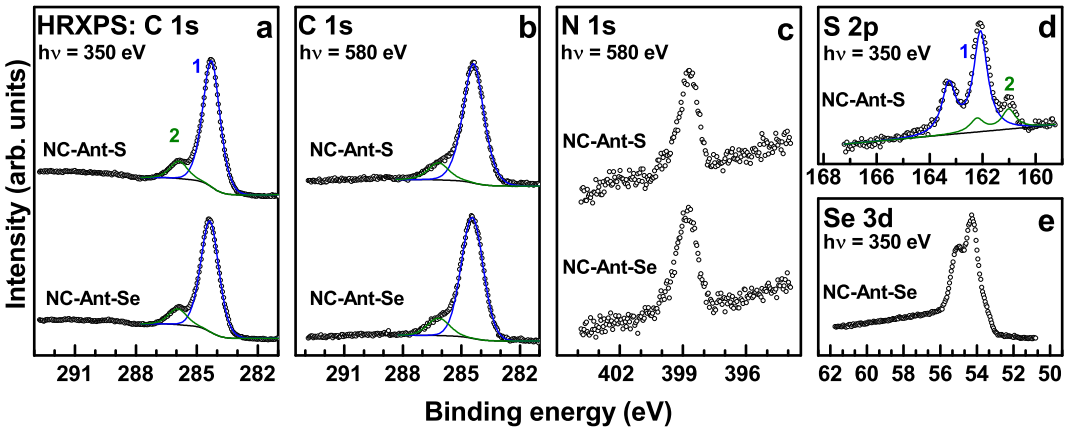

Figure 4.7.: C 1s (a,b), N 1s (c), S 2p (d) and Se 3d (e) HRXP spectra of the NC-AntS and NC-AntSe SAMs. The C 1s spectra are decomposed in individual emission viz.main peak (1; blue line) and high E_B shoulder (2; olive line). The S p spectrum is also decomposed in individual emissions viz. main peak (1; blue line) and a shoulder at lower E_B (2; olive line). The photon energies are given in the panels.

selenolate species bound to noble metal surfaces[40,102,173,198] and means that basically all molecules were anchored to the substrate via a selenolate-gold bond, forming well-defined SAMs.

Similar to the previously discussed case of NC-NapS/Se films, the C 1s spectra of the NC-AntS and NC-AntSe exhibit a small shoulder (**2**) along with an intense emission (**1**) at E_Bs of 285.91 eV and 284.32 eV, respectively. The shoulder can be assigned to the nitrile carbon (compare nitrile-substituted oligophenylenes and previously discussed naphthalene),[36,188] while the main peak represents the anthracene backbone. The shoulder slightly decreases with increasing PE, which is visible from a comparison of figure 4.7a and b. This is due to the IMFP, which increases photoemission from the backbone at higher electron energies.

The N 1s spectra of both NC-NapS and NC-NapSe films in figure 4.7c exhibit a one single N 1s peak at a E_B of 398.7 eV. Similar to the analogous systems, this emission can be assigned to the nitrile group.[36,38,57,188] The presence of only one emission indicates the same chemical state for all nitrile groups. The group is exclusively located at the SAM-ambience interface, regarding the given molecular structure and binding scheme (discussion S 2p, Se 3d spectra).

Besides the above analysis, also the effective thickness of the NC-AntS and NC-AntSe films was determined, using the C 1s to Au 4f intensity ratio. Calculated within the standard approach, presented in the experimental part (section

3.2.1.2), the effective film thickness for NC-AntS is ∼11.0 Å and for the NC-AntSe about 2.7% larger at ∼11.3 Å. This is slightly thinner than the length of the molecular precursors of NC-AntS and NC-AntSe, being ∼13.4 Å and ∼13.5 Å, respectively, which suggests a flat tilt angle of the molecules and a wider molecular packing density, compared to the NC-NapS and NC-NapSe film.

4.1.2.2. NEXAFS Spectroscopy

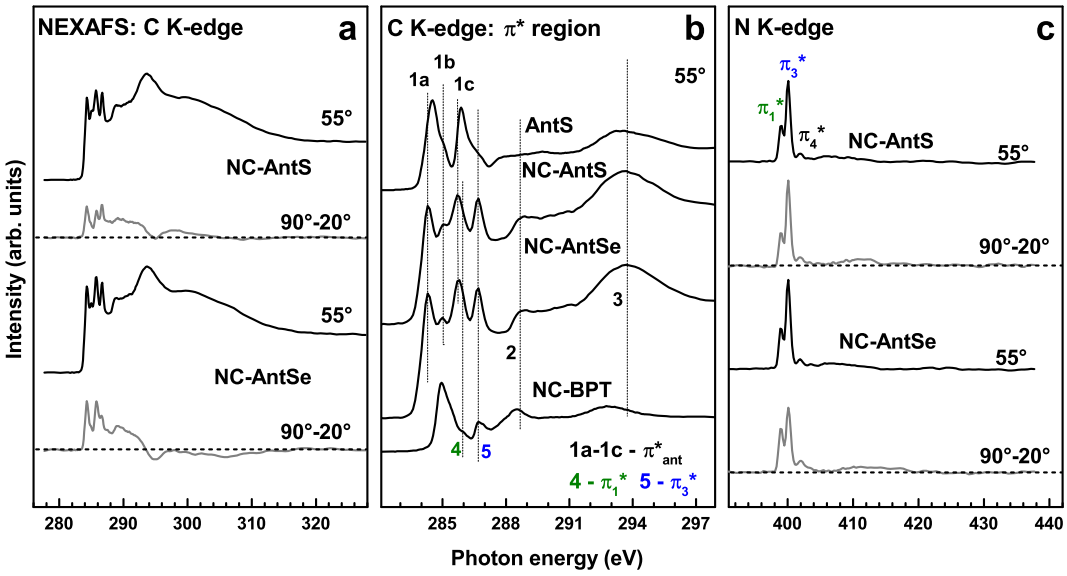

Figure 4.8.: C (a,b) and N (c) K-edge NEXAFS spectra of the NC-AntS and NC-AntSe SAMs acquired at an X-ray incident angle of 55° (black solid curves) along with the respective difference between the spectra collected under normal (90°) and grazing (20°) incidence geometry (gray solid curves in a and c). The horizontal dashed lines correspond to zero. In (b), the region of the π^* resonances is presented to get a better overview; the spectra of NC-BPT and unsubstituted anthracenethiol are added for comparison. AntS adapted with permission from [202]. Copyright 2001 American Chemical Society. Individual resonances in b and c are marked.

The C K-edge NEXAFS spectra of the NC-AntS and NC-AntSe SAMs are presented in figure 4.8a. This figure sums up the spectra acquired at an X-ray incidence angle of 55° as well as the difference spectra collected at X-ray incident angles of 90° and 20°. The C K-edge spectra exhibit a variety of sharp resonances, which are magnified in figure 4.8b along with an unsubstituted

anthracenethiol[202] and NC-BPT for comparison. The resonances are compiled in table 4.2.

Table 4.2.: Compilation of the resonances and according PE in the C K-edge spectrum.

resonance	**1a**	**1b**	**1c**	
PE	284.30 eV	285.02 eV	285.71 eV	
resonance	**2**	**3**	**4**	**5**
PE	288.68 eV	293.80 eV	285.95 eV	286.67 eV

The π resonances **1a**, **1b** and **1c** along with the π resonance **2** and the σ resonance **3** can be assigned (with a small shift) to the molecular backbone of the anthracene molecule anchored to the Au substrate.[202,220,221] The additional π resonances **4** (overlaid with **1c**) and **5** are resulting from the terminal benzonitrile ($-$C$\equiv$N) group[36,38,57] interacting with the anthracene backbone. These emissions can also be found in the added NC-BPT spectrum, added for comparison in figure 4.8b.

The N K-edge NEXAFS spectra of the NC-AntS and NC-AntSe are presented in figure 4.8c. These spectra look very similar to those of NC-NapS and NC-NapSe, discussed in the previous section. The weak emission at $\sim$401.9 eV probably originated from the π_4* of nitrile.[207,208], while the dominant double π* resonance at $\sim$398.9 eV and $\sim$400.0 eV is characteristic of benzonitrile. It appears in spectra for the gas phase,[208] molecular solid,[207] and monomolecular films containing this functional group.[36,38,57] Due to the conjugation between the π* orbitals of the nitrile group and the adjacent phenyl ring, the degeneration of the π(C$\equiv$N*) orbital is lifted and it splits into two orbitals. In contrast to nitrile-substituted alkanethiols, the energies can be clearly distinguished.[33,37,39] The orientation and intensity of the π_1* and π_3* are the same as shown schematically for NC-NapS/Se in figure 4.4.

The C and N K-edge NEXAFS spectra of the NC-AntS and NC-AntSe SAMs exhibit pronounced linear dichorism as follows from the respective difference spectra in figure 4.8a and c. The positive sign of the difference curves suggests an upright orientation of the molecules in the SAMs. The exact twist and tilt angles of the molecules were obtained from the NEXAFS data. The average tilt angles of the most dominant π* orbitals of the anthracene backbone (**1a**, figure 4.8b) and the nitrile group (π_1* and π_3*, figure 4.8c) were derived within the standard theoretical framework for vector type molecular orbitals.[129,202] The same procedure and equations as for the naphthalene molecules in the previous section were used to derive tilt and twist values for NC-AntS and NC-AntSe, which are compiled in table 4.3. The values, derived by the N K-edge data,

Table 4.3.: Average tilt angles of the π_{ant}* and $\pi_{1,3}$*(NC) orbitals derived from the numerical evaluation of the NEXAFS data for the NC-AntS and NC-AntSe SAMs and the average molecular tilt and twist angles of the molecular backbone.[a]

average angles/system	NC-AntS	NC-AntSe
π* orbitals (antracene) - α_{ant}	61°	65°
π_1* orbital (NC) - α_1	67°	71°
π_3* orbital (NC) - α_3	70°	65°
twist angle (γ) from α_1 and α_3	42°	53°
molecular tilt (β) from α_1 and α_3	31°	32°
molecular tilt (β) from α_{ant} and γ	40°	44°

[a] Error bars can be estimated at ±3°.

viz. the nitrile group (α_1 and α_3), can be trusted more, because the C K-edge spectrum has so many emissions, superposing each other, making it difficult to obtain representative results from the π_{ant}* data.

4.1.2.3. AES and RAES

The electronic conductance in the NC-AntS and NC-AntSe SAMs was tested by RAES at the N K-edge within the CHC approach. The spectroscopic analysis of the systems by HRXPS and NEXAFS spectroscopy showed that the nitrile groups are at the SAM-ambience interface and are electronically connected to the substrate through the molecular anthracene framework. Concluding from this analysis, the electronic pathway for ET was well-defined. As mentioned in previous sections and the experimental part, ET could only occur, if it was energetically allowed. The π* resonance excitation energy should be higher than the E_B of the respective core electron (N 1s E_B ~398.6 eV). This was the case for the π_1* but not the π_3* orbital, having excitation energies of ~399.25 eV and ~398.25 eV, respectively. Thus, tail group-to-substrate transfer of the resonantly excited electron is energetically allowed only for the [N 1s]π_1* excitation.

As shown in figure 4.9a, the decay of these excitations can occur in three possible ways if radiative decay is neglected. These include the participator (P), spectator (SP) scenarios and additionally ET of the excited electron to the conduction band (CB) of the substrate. These routes and according spectral signatures were discussed in detail in the experimental section in figure 3.9 and the according text.

[N 1s]π_1* RAE spectra of the NC-AntS and NC-AntSe SAMs along with their reconstructions by the linear combination of the purely resonant (P and SP) and

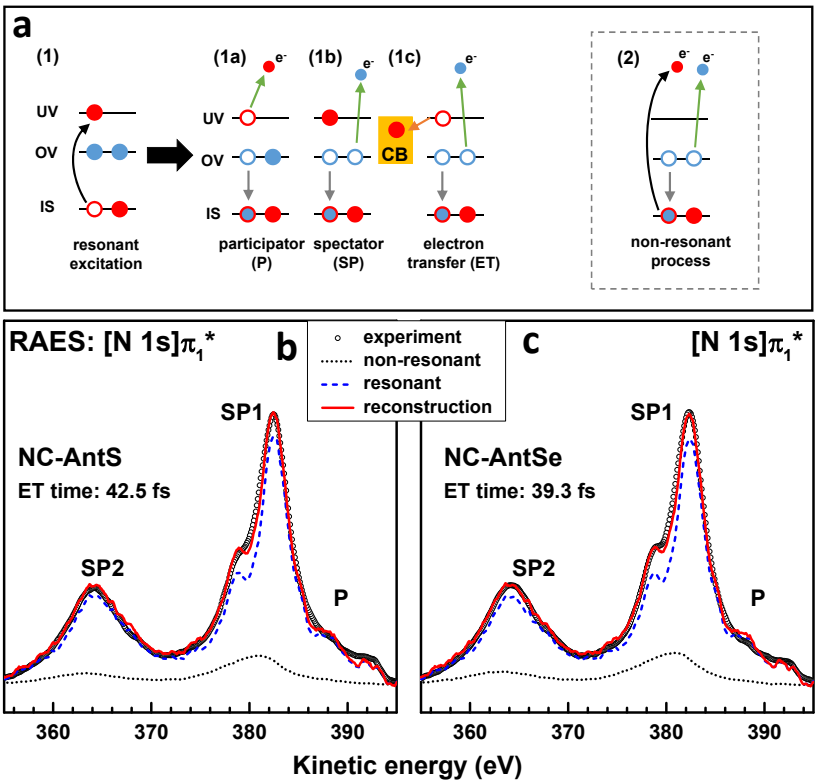

Figure 4.9.: (a) Scheme of core excitation/de-excitation routes for the nitrile group in the NC-AntS and NC-AntSe SAMs in the framework of RAES. This scheme was explained in the experimental part in figure 3.9 and is added just for the sake of completeness. [N 1s]π_1* RAE spectra of the NC-NapS (a) and NC-NapSe (b) SAMs (open circles) along with their reconstructions (red solid lines) by the linear combination of the purely resonant (blue dashed lines) and non-resonant (black dotted lines) contributions. Participator (P) and spectator (SP) features are marked. The derived τ_{ET} values are given in the figures.

non-resonant (ET) contributions are presented in figure 4.9b and c, respectively. The pure resonant spectrum was measured using a NC-TPT monolayer on Au(111), which was also used in the naphthalene case, as it has the same benzonitrile group, but is too long to have a perceptible ET contribution in the RAE spectrum.[38] The spectra of both molecules show a small participator and large spectator contributions. The data are very similar to the NC-NapS and NC-NapSe spectra in figure 4.5b and c.

Analysis of [N 1s]π_1* RAE spectra in figure 4.9b an c suggests that they both contain a detectable contribution of the ET route, represented as an admixture

of the non-resonant spectrum to the pure resonant curves. For both spectra nearly the identical portion of the non-resonant features is detected (NC-AntS: 13% and NC-AntSe: 14%). Based on these values the standard formula of the CHC approach (equation 3.2 explained in the experimental part) can be used. The derived values for τ_{ET} are 42.5±5 fs and 39.5±5 fs for NC-AntS and NC-AntSe, respectively. As expected this value is higher than for the analogous NC-NapS/Se films (both 24±4 fs) or NC-BPT films (29±6 fs) but smaller than for NC-TPT, which is out of the measurable range (>120 fs). Compared to the NC-NapS/Se, also for the NC-AntS/Se the τ_{ET} is nearly identical in both films. The small difference is resulting from the larger variation for smaller P_{ET}. A change of 1% already results in the shown difference, which is in in the error range for both cases. [N 1s]π_3* has forbidden ET, as discussed above, and is therefore not shown. The spectra are identical to the RAE spectra of NC-NapS/Se shown in figure 4.5c. The different τ_{ET} for [N 1s]π_1* and [N 1s]π_3* are well-known and a common phenomenon in benzonitrile-substituted monolayers.[38] The π_1 orbital is strongly conjugated with the π system of the adjacent ring system, which facilitates the electron transport along the molecular backbone. The π_3 orbital is almost exclusively located at the nitrile group, which can be associated with a longer ET pathway and an additional injection barrier.

4.1.2.4. Discussion

The analysis of the NC-AntS and NC-AntSe films with XPS and NEXAFS spectroscopy showed that the SAMs have a similar effective film thickness (∼11 Å)and that the average tilt angles of the anthracene backbone is also quite similar (61° and 65° for coupling via −S and −Se, respectively), which makes them suitable candidates for investigation of their ET dynamics in the framework of RAES and CHC. According to the findings about the intramolecular stability (Se−C and S−C) and electronic coupling efficiency of S−Au and Se−Au bonds in the previous section,[188] similar values for τ_{ET} were expected and confirmed by the RAES measurements (in average ∼41±6.5 fs).

An interesting finding of the experiments in the present case is that ET is actually possible for the π_1* orbital of the nitrile moiety in NC-AntS and NC-AntSe. In the literature it has been shown that τ_{ET} in molecular films increases exponentially with the number of phenyl rings: NC-PT(∼9 fs)→NC-BPT(∼29 fs)→NC-TPT(>120 fs), which is exhibited in figure 4.10 (black dots and exponential fit). The value for τ_{ET} of NC-TPT was set to the limit of the CHC approach, 120 fs in figure 4.10, because NC-TPT shows no perceptible ET contribution in the RAE spectrum.[38] For annulated molecules, namely NC-NapS (∼24 fs; analyzed in the previous section) and NC-AntS (∼41 fs), this exponential increase of τ_{ET} depending on the number of rings is not observed.

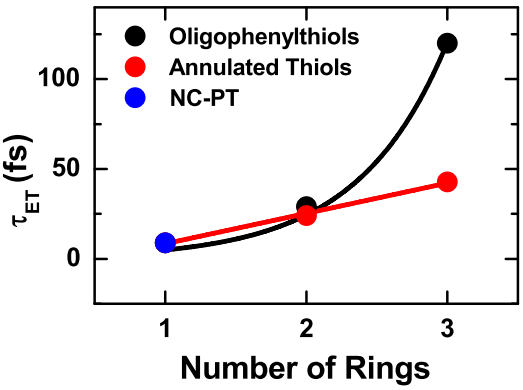

Figure 4.10.: The increase of τ_{ET} from the nitrile group to the substrate in relation to the number of rings in substituted oligophenylthiols and annulated thiols, starting from the one ring molecule NC-PT (blue dot). For oligophenylthiols (namely NC-BPT, NC-TPT, black dots) the increase of τ_{ET} is exponential, while τ_{ET} for annulated molecules (namely NC-NapS and NC-AntS, red dots) it is linear. The respective lines show an exponential and linear fit. ET for NC-TPT was assumed at the limit of the approach for visualisation τ_{ET}=120 fs. The real value might be even higher.

Changing the molecular structure from two to three annulated rings resulted in a linear increase of τ_{ET} (red dots and linear fit in figure 4.10). As a starting point for both systems the one ring molecule nitrile-substituted phenylthiol was used (NC-PT; blue dot in figure 4.10).[38] This change in the τ_{ET} dependence could probably be expected, as the rings in naphthalene and anthracene are fused and they both have one conjugated π-system, delocalized in the molecular backbone,[56] which presumably increased the ET properties through the backbone. The π-systems of molecules with oligophenyl backbone like NC-BPT or NC-TPT are located at each phenyl ring, which probably are conjugated,[222] but less than in the acene backbones and therefore the electron has to "travel" inbetween different π-systems, which increases the ET time.

From the plot of $\ln\tau_{\mathrm{ET}}$ vs the molecular length in figure 4.11, following the approach in the literature[37,38] and adapting the exponential decay law introduced in section 2.5, values for β and τ_{S-Au} can be estimated. According to the adapted equation: $\tau_{ET} = \tau_{S-Au} exp(\beta_{Acene} l_{Acene})$, an attenuation factor β of 0.25 $\mathrm{\AA}^{-1}$ was calculated from the slope, taking both acenes (NC-NapS and NC-AntS) into account (fit; red solid line). To verify the attenuation factor, a second fit, adding NC-PT, was added (blue solid line) and β was found to be 0.35 $\mathrm{\AA}^{-1}$. Taking both fits into account, the real value of β should be inbetween both values, viz. approximatly 0.30 $\mathrm{\AA}^{-1}$. This value corresponds to the value

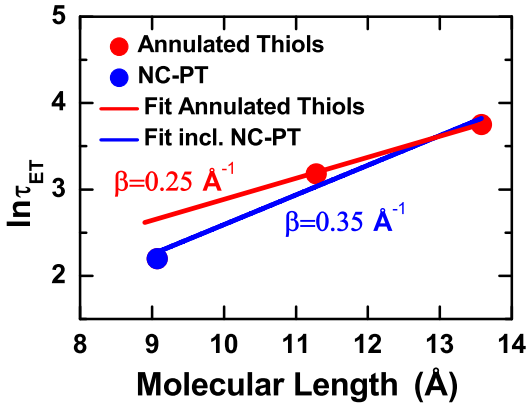

Figure 4.11.: Estimation of β for acenes from the plot $\ln\tau_{ET}$ vs molecular length, following an adaptation of the exponential decay law. The red solid line shows the fit regarding only NC-NapS and NC-AntS. The blue solid line also includes NC-PT into the fit.

derived by dynamic studies of oligophenylthiolates on gold (0.29 $Å^{-1}$; tunneling through the backbone assumed),[38] which indicates a similar efficiency for ET through both backbones, if not a slightly better one for acenes, regarding the β value of 0.25 $Å^{-1}$ without NC-PT. Additionally, ET across the thiolate anchor (S−Au) could be derived from the intersection of the average of both fits with the axis in figure 4.11 and was found to be around 1 fs, for the acene fit only around 1.5 fs, which is lower than the values found for oligophenylthiolate films (2.8 fs)[38] or alkanethiolate films (2.3 fs).[223]

For a comparison with attenuation factors obtained from static conductance measurements, describing the overall performance of the bridging molecules and not providing information on the dynamics related to a specific orbital (π_1 or π_3), the following values for acenes can be found in the literature: β=0.45 $Å^{-1}$[22], 0.5 $Å^{-1}$ for monothiols[53] and 0.2 $Å^{-1}$ for dithiols.[53] These values for monothiols are slightly higher than those of the dynamic studies after defined π_1 excitation. This phenomenon has already been observed and explained in previous studies where β values from both static and dynamic measurements were compared.[38]

4.1.3. Nitrile-Azulenethiol

Figure 4.12 shows the molecules, forming the monomolecular films, which are analyzed in this section.

Figure 4.12.: Structures of the molecules along with their assigned acronyms. (a) AzuSH (b) NC-AzuSH

4.1.3.1. XPS and HRXPS

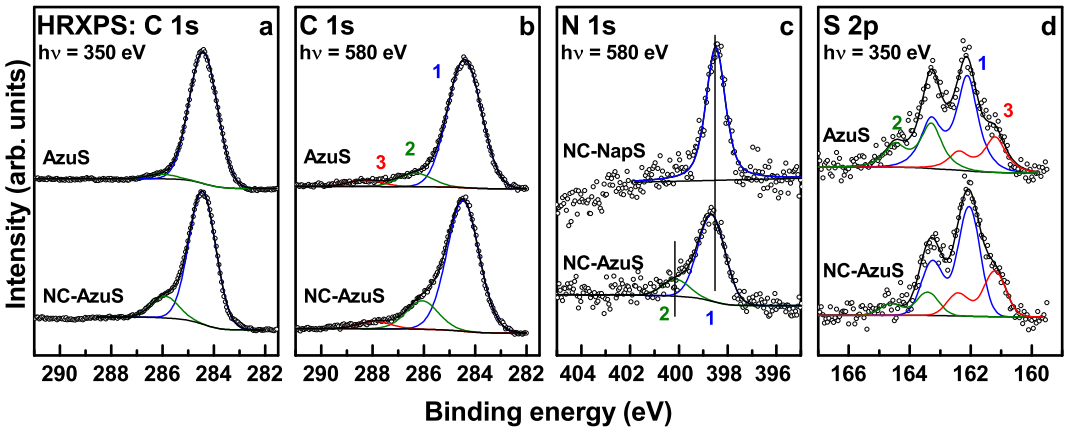

Figure 4.13.: C 1s (a,b), N 1s (c) and S 2p (d) HRXP spectra of the AzuS and NC-AzuS SAMs. The spectrum of NC-NapS from a previous section was added for comparison. The spectra are decomposed into individual emissions marked with numbers. The photon energies are given in the panels.

C 1s, N 1s and S 2p HRXP spectra of the AzuS and NC-AzuS SAMs are presented in figure 4.13. The S 2p spectra in d show a pronounced double peak (**1**) at ∼162 eV ($S\,2p_{3/2}$), representative for thiolate species bound to noble metal surfaces.[89,173,197] Unfortunately, also traces of unbound (**2**) and atomic thiol (**3**) are visible in the spectra. The amount of thiolate-species in NC-AzuS, derived from the relative intensities in figure 4.13d, is about 62% (blue line).

This showed that the film was not perfect, but a representable part of the molecules were anchored via the thiolate bond to the substrate, as necessary for our analysis.

The C 1s spectra in figure 4.13a and b exhibit an intense emission at a E_B of ~284.4 eV (**1**), accompanied by a weak shoulder at E_B of ~286 eV (**2**), which is more intense for the nitrile-substituted molecular film. The emission **1** can be assigned to the molecular backbone. In the case of substituted azulene, the shoulder **2**, is related to the carbon in the nitrile group, similar to the previously analyzed SAMs of NC-NapS/Se and NC-AntS/Se and comparable to substituted oligophenylenes.[36,57] However, in the unsubstitued azulene films, the shoulder is slightly shifted to higher E_B and is stronger in the case of the 580 eV spectrum. This leads to the assumption that the origin is close to the substrate or at least in the molecular backbone. The position of **2** corresponds also to a possible minor contamination (CO). The weak emission (**3**), visible only in figure 4.13b acquired at 580 eV, is presumably related to another minor contamination like COOH. Since the peaks are only visible in the higher energy spectra, the contamination was also most likely located at the substrate to SAM interface.

The N 1s spectrum in figure 4.13c exhibit a strong N 1s emission at ~398.65 eV (**1**). This emission can be assigned to the nitrogen atom of the nitrile group. The spectrum of NC-NapS was added for comparison. The emission **2**, visible as a shoulder to the strong nitrile peak, can be assigned to a possible isonitrile moiety at a E_B of ~400 eV.[224]

From the relation of the characteristic C 1s to Au 4f intensities the effective thickness of the NC-AzuS film was calculated using the standard approach as decribed before.[183,199] It was found to be 10.2 Å, which is comparable to the previously calculated thickness of its isomer, the substituted naphthalene film (10.5 Å). As the effective thickness of the unsubstituted azulene is quite similar (10.0 Å), it suggests a slightly lower packing density for the substituted film. The thicknesses and according packing densities are compiled in table 4.4.

Table 4.4.: Film thickness and packing density derived from the XPS data.[a]

monolayer	effective thickness (Å)	packing density (molecules/cm^2)
AzuS	10.0	4.07×10^{14}
NC-AzuS	10.2	3.87×10^{14}

[a] Error bars can be estimated at ±5%

4.1.3.2. NEXAFS Spectroscopy

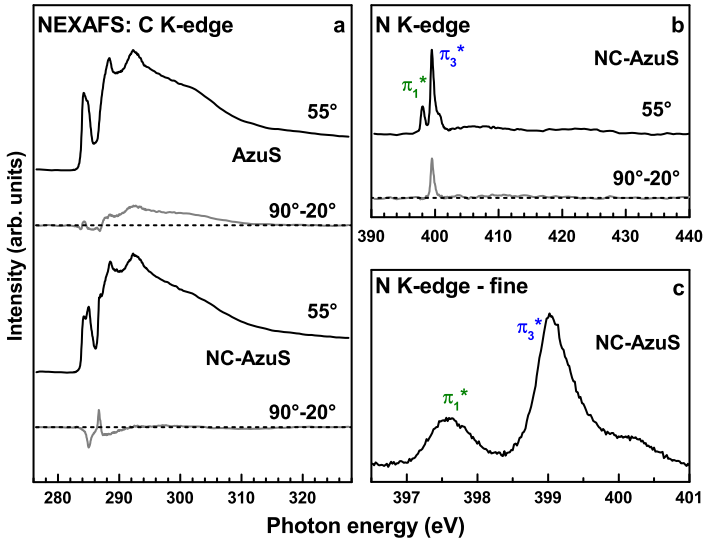

Figure 4.14.: C (a) and N (b+c) K-edge NEXAFS spectra of the AzuS and NC-AzuS SAMs acquired at an X-ray incident angle of 55° (black solid curves) along with the respective difference between the spectra collected under normal (90°) and grazing (20°) incidence geometry (gray solid curves in a and b). The horizontal dashed lines correspond to zero. In (c), the region of the π^* resonances is presented to get a better overview. Individual resonances in b and c are marked.

Magic angle (55°) and respective difference (90°-20°) NEXAFS spectra of AzuS and NC-AzuS measured at the C K-edge and for the latter also at the N K-edge, are shown in figure 4.14.

The C K-edge spectra of AzuS in figure 4.14a are similar to the naphthalene spectra, shown in figure 4.3b, dominated by a sharp, slightly splitted π resonance at ∼284.4 eV (1s→ π_1*). The next peak at ∼288.4 eV is broader and may arise from a combination of the π_3* and σ*(C−H) excitation.[225] The third peak at ∼292.3 eV can be assigned to σ*(C−C) transitions.[225] In the C K-edge spectrum of the nitrile-substituted azulene, all these resonances are also visible with a more pronounced splitting of the first π^* transition at ∼284.1 eV and ∼285.0 eV. This might also be due to the introduction of the nitrile moiety, interacting with the azulene backbone. Compared to the previously analyzed nitrile-substituted naphthalene backbone and the literature,[38] a double feature should be visible in the C K-edge spectrum. This feature could be represented by increased peak at ∼285.0 and the *shoulder* at ∼286.8 eV. Looking at the difference spectrum, the *shoulder* is clearly visible as a separate peak, which is

not visible in the difference spectrum of unsubstituted azulene. Unfortunately both C K-edge difference spectra are not showing a clear linear dichroism for the molecular backbone.

The N K-edge spectrum looks similar to the reported spectra for the benzonitrile moiety.[38,207] The double resonance at ~397.6 eV (π_1; perpendicular to the plane of adjacent ring) and ~399.0 eV (π_3; parallel to the plane of the adjacent ring) is clearly visible.[207,208] Additionally there is a small shoulder at ~400.2 eV, which can be attributed to π_4.[38]

The NEXAFS data was processed to derive the average tilt angles of the most dominant π^* orbitals of the azulene backbone (figure 4.14a) and the nitrile moiety (π_1^* and π_3^* in figure 4.14b and c). The values, derived with the standard procedure described before,[129,202] are compiled in table 4.5.

Table 4.5.: Average tilt angles of the π_{azu}^* and $\pi_{1,3}^*$(NC) orbitals derived from the numerical evaluation of the NEXAFS data for the NC-AzuS SAM and the average molecular tilt and twist angles of the molecular backbone. Additionally, the tilt angle for the AzuS SAM is shown for comparison.[a]

average angles/system	NC-AzuS	AzuS
π^* orbitals (azulene) - α_{azu}	54°	55°
π_1^* orbital (NC) - α_1	55°	
π_3^* orbital (NC) - α_3	63°	
twist angle (γ) from α_1 and α_3	39°	
molecular tilt (β) from α_1 and α_3	48°	
molecular tilt (β) from α_{ant} and γ	49°	

[a] Error bars can be estimated at ±3°.

Based on the derived tilt angles for NC-AzuS, the average tilt and twist angles for the molecular backbone were also determined, using equations 4.1, 4.2 and 4.3, introduced in the naphthalene section.[35,36,57] The resulting values are also compiled in table 4.5. Note that the results obtained from equation 4.1 and 4.2 are very similar to the result of equation 4.3 although they are obtained from different building blocks (backbone and nitrile group).

The average tilt angle of π^* orbital in the unsubstituted azulene is the same as for the NC-AzuS SAM. Following from the derived value around 54-55° and the information from the difference spectra (no linear dichroism for the molecular backbone; figure 4.14a) a slightly unordered SAM has to be assumed.

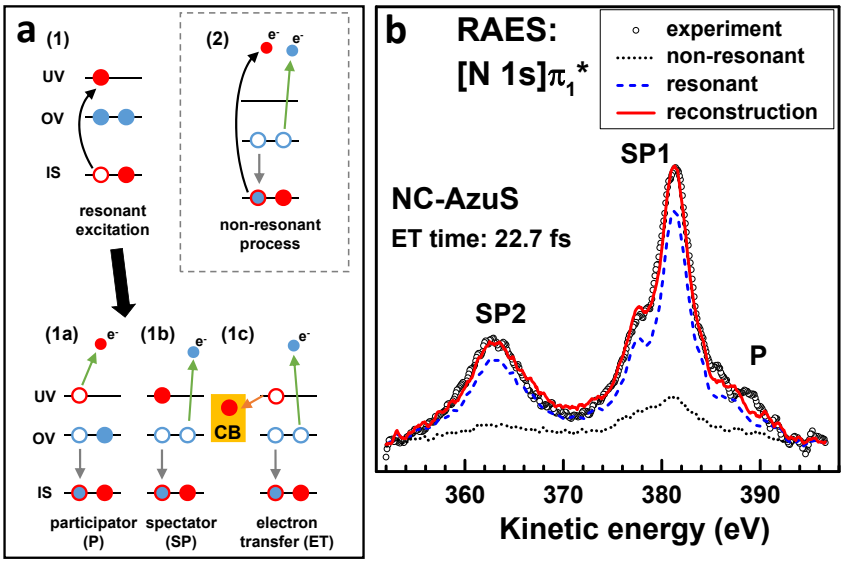

Figure 4.15.: (a) Scheme of core excitation/de-excitation routes for the nitrile group in the NC-AzuS SAM in the framework of RAES. This scheme was explained in the experimental part in figure 3.9 and is added just for the sake of completeness. [N 1s]π_1* RAE spectrum of the NC-AzuS SAM (open circles) along with the reconstruction (red solid lines) by the linear combination of the purely resonant (blue dashed lines) and non-resonant (black dotted lines) contributions. Participator (P) and spectator (SP) features are marked. The derived τ_{ET} value is given in the figure.

4.1.3.3. AES and RAES

The electronic conductance in the NC-AzuS film was tested by RAES at the N K-edge within the CHC approach. Following the spectroscopic analysis with HRXPS and NEXAFS spectroscopy, the prepared films were found to be suitable to deliver a representable result for electron transfer investigations.

ET could only occur, if it is energetically allowed. The energy of the π* resonantly excited electron at the nitrile group should be positive with respect to the E_F of the substrate. The E_B of the respective core electron should be lower than the excitation energy for the π* excitation. In the NC-AzuS project, this is the case for the [N 1s]π_1* orbital (~397.6 eV), compared to the N 1s E_B (~398.65 eV). For [N 1s]π_3* ET is forbidden (~399 eV).

The possible decay routes for the excitation are shown in figure 4.15a and were described in detail in the experimental section (figure 3.9) and were just added for the sake of completeness. The [N 1s]π_1* RAE spectrum of NC-AzuS along with the reproduction by linear combination of the purely resonant (P

and SP) and non-resonant (ET) contributions is presented in figure 4.15b. For the purely resonant contributions, NC-TPT on Au(111) was measured as a reference, which is too long to show a perceptible contribution of ET in the RAE spectrum.[38] In the spectrum of NC-AzuS both spectator and weak participator contributions are visible. The spectrum is similar to the NC-NapS/Se ones in figure 4.5.

Analysis of the [N 1s]π_1* spectra shows a considerable contribution of the ET route. The reconstruction of the spectral line shape, using the purely resonant and the nonresonant curves gives a portion of the ET decay route around 22%, resulting in τ_{ET} of 22.7±4 fs. To derive this value, the introduced main formula of the CHC approach, $\tau_{ET} = \tau_{core}(1 - P_{ET})/P_{ET}$ with τ_{core}=6.4 fs for N 1s was used.[27,29,189,190,226,227] The characteristic transfer time is nearly identical with the previously investigated SAMs of NC-NapS and NC-NapSe (24±4 fs).

4.1.3.4. Discussion

In the spectroscopic analysis with HRXPS and NEXAFS spectroscopy, the investigated NC-AzuS SAM showed the same features as the previously analyzed NC-NapS on gold. The only difference was a second emission in the nitrogen peak besides the dominant emission of the nitrile group, which presumably could be assigned to an isonitrile moiety.[224] The major part of the molecules was bound to the substrate via S−Au, allowing a numerical analysis of the NC-AzuS film on Au(111). From the XPS measurements an effective film thickness of 10.2 Å was derived, which is comparable to the thickness of its previously analyzed isomer NC-NapS with 10.5 Å.[188] Also the respective tilt (∼39° vs ∼41°) and twist (∼49° vs ∼53°) angles of the molecular backbones, derived from the NEXAFS data are quite similar.[188]

The spectroscopic and structural similarities of both NC-AzuS and NC-NapS films let expect a similar result regarding the ET properties. According to the results of the RAES and following CHC calculations, the characteristic ET time (τ_{ET}) between the terminal nitrile group in the NC-AzuS molecules and the Au(111) substrate of 22.7±4 fs is nearly identical with τ_{ET} in NC-NapS film with 24±4 fs.[188] ET was not influenced by the different, non-benzenoid electronic structure, with a higher electron density in the five ring.[228]

4.1.4. Cyanide on Gold

The results presented in this subsection are accepted for publication by *J. Phys. Chem. C* and are adapted from [229].

The films were also investigated by our partners (group of Prof. Paul Weiss, University of California, Los Angeles, USA and group of Prof. David Allara,

Pennsylvania State University, Pennsylvania, USA) using STM, surface enhanced Raman spectroscopy (SERS) and IR spectroscopy. Their findings were included in the discussion and the related figures can be found in the Appendix A. Figure 4.16 shows the assumed formation of cyanide on a Au(111) substrate.

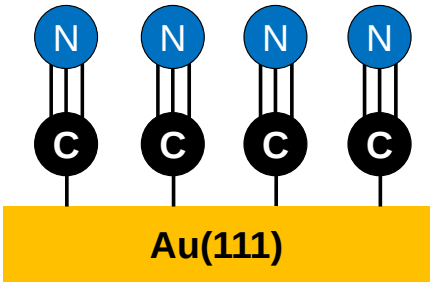

Figure 4.16.: Scheme of the cyanide formation on Au(111).

4.1.4.1. XPS and HRXPS

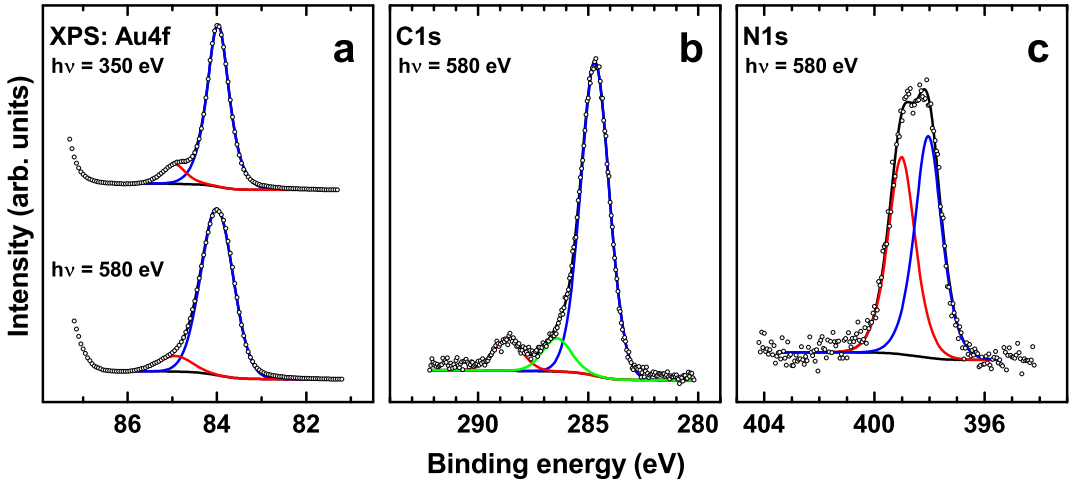

Figure 4.17.: Au $4f_{7/2}$(a), C 1s(b) and N 1s(c) X-ray photoelectron spectra of NC/Au(111) acquired at photon energies of either 350 eV or 580 eV as marked in the panels (open circles). The spectra are fit and decomposed into individual contributions (thin solid lines). Details are discussed in the text.

Representative Au $4f_{7/2}$(a), C 1s(b) and N 1s(c) XP spectra of NC/Au(111) are shown in figure 4.17. The Au $4f_{7/2}$ spectra in (a) exhibit a weak shoulder

at the high E_B side of the main emission at a E_B of 84.95 eV. The appearance of this shoulder is attributed to the effect of adsorbed NC, which is strong and, in its extent, is similar to the oxidation of the gold substrate.[230] Only the topmost layer of the Au(111) substrate is affected, as visible from the direct comparison of the spectra acquired at PEs of 350 eV and 580 eV in figure 4.17a. Due to the strong dependence of the sampling depth of XPS on the kinetic energy of photoelectrons,[176] the contribution of the surface as compared to bulk should be much weaker in the latter case and, as expected, the high E_B shoulder decreases significantly in intensity at a PE of 580 eV as compared to 350 eV. The intensity relation beteen th shoulder and the main emission the 350 eV spectrum can be compared to the analogous relation in the spectrum of clean Au(111), where the contributions of the topmost layer and the bulk can be straightforwardly distinguished.[173] Accordingly, the shoulder is related to the topmost layer of the Au(111) substrate only. According to its spectral weight, the signal corresponds to 25-30% of atoms in this layer.[231]

The C 1s XP spectrum of NC/Au(111) in figure 4.17b exhibits strong emission at ∼284.7 eV accompanied by two weak peaks at ∼284.4 eV and ∼288.65 eV. The dominant emission can be assigned to the adsorbed NC molecules, while the low intensity peaks presumably stem from contamination, most likely CO (∼286.4 eV) and COOH (∼288.65 eV).[232] Such contamination can hardly be avoided considering the ultimate thinness of the NC monolayer and its exposure to ambient in the course of the sample handling. The formation of well-ordered monolayers, as indicated by the STM images (the STM results are presented in figures A.5 and A.6 in the Appendix), suggests that such contamination is inconsequential. As to dominant emission, note for comparison that its E_B is much lower than that of the nitrile carbon in SAMs of the nitrile-substituted alkanethiols, NC−(CH_2)n−SH (NC-Cn) on Au(111), e.g., 286.2 eV at n=3.[37] The lower E_B in the case of NC/Au(111) can be attributed to the direct bonding of NC to the substrate (chemical shift) as well as to more efficient screening of the photoemission hole by the substrate electrons (the screening effect scales according to the Coulomb potential, i.e., is proportional to 1/r).

The N 1s XP spectrum of NC/Au(111) in figure 4.17c exhibits a broad peak that can be tentatively decomposed into two individual emissions at ∼398.1 eV and ∼399.0 eV, with the former emission being more intense. This emission can be unequivocally attributed to the CN molecules attached to the substrate over C−Au bond. The E_B of 398.1 eV correlates well with the respective E_B for the NC-alkyl SAMs on Au(111), viz. 398.84 eV for the NC−C_2H_4S film and 398.98 eV for the NC−C_3H_6S monolayer,[37] being noticeably smaller than these values, because of the stronger proximity of CN to the substrate in the case of NC/Au(111) (see discussion regarding the C 1s spectrum). The value

of ∼399.0 eV is even higher than the value of 398.84 eV for the NC−C_2H_4S film on Au(111), suggesting that the respective species are bound only weakly to the substrate, probably in a physisorbed fashion, or, most likely, as CNH or CN−H_2O species. Is is well known that the protonation or association with H_2O shifts the N 1s binding energy to higher values.[233,234] The C atom attached directly to the metal substrate will not be affected strongly by this process, resulting in only a small binding energy shift and in only one joint C 1s emission.

4.1.4.2. NEXAFS Spectroscopy

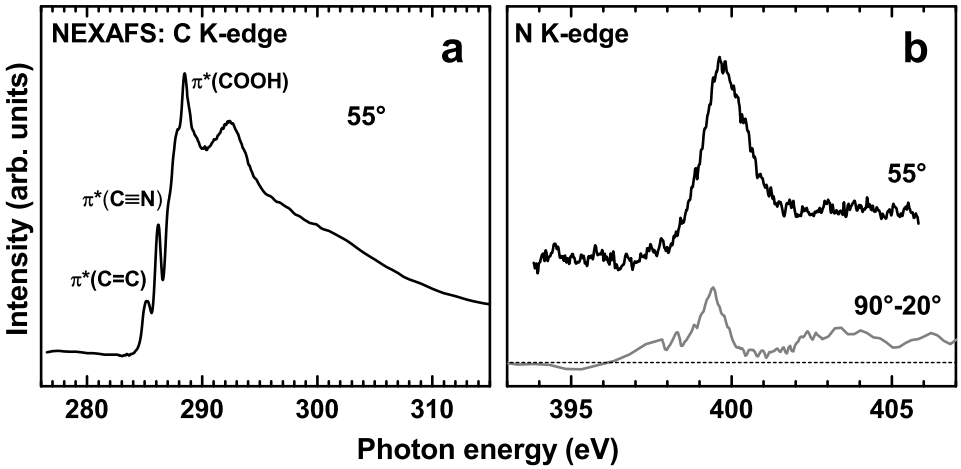

Figure 4.18.: C (a) and N (b) K-edge near-edge X-ray absorption fine structure spectra of NC/Au(111) acquired at an X-ray incidence angle of 55° (black solid curves), along with the respective difference between the spectra collected under the normal (90°) and grazing (20°) incidence geometry (gray solid curve in panel b). The characteristic absorption resonances are marked. The horizontal dashed line in panel (b) corresponds to zero intensity.

C and N K-edge NEXAFS spectra of NC/Au(111) acquired at an X-ray incident angle of 55° are presented in figure 4.18, along with the respective difference between the N K-edge spectra collected under the normal (90°) and grazing (20°) incidence geometry. The *magic* angle, 55° spectra are free of orientational effects and only representative of the electronic structure of the studied systems.[129] In contrast, the difference between the spectra acquired at normal and grazing incidence of X-rays are representative of the molecular orientation, averaged over the probed ensemble, relying on the linear dichroism effect in X-ray absorption.[129]

The C K-edge spectrum of NC/Au(111) in figure 4.18a exhibits several absorption resonances superimposed onto the absorption edge. These features include the π^*(C=C) resonance at 285.1 eV, the π(C*≡N) resonance at 286.2 eV and the π^*(COOH) at 288.5 eV (the assignments were made according to literature).[37,174] The π^*(C=C) and π^*(COOH) features stem from contamination while the π(C*≡N) resonance is characteristic of the CN groups and is attributed to two (almost) degenerated, mutually orthogonal π(C≡N) orbitals.[33,39] Its position depends only weakly on the chemical state of the CN group (unless there is π^*-π^* hybridization with the adjacent functional group)[38] and, in particular, does not vary much across the NC-alkyl/Au(111) series, being 286.8-286.9 eV.

The 55° N K-edge spectrum of NC/Au(111) in figure 4.18b exhibits a characteristic π^* resonance of the nitrile group at 399.7 eV. Similar to the π(C*≡N) resonance, it is attributed to two (almost) degenerated, mutually orthogonal π(C≡N) orbitals.[33,39] The presence of this feature as well as the π(C*≡N) resonance at the C K-edge (see above) suggests an upright orientation of the NC moieties in NC/Au(111). Otherwise, both π(C*≡N) and π(C≡N*) resonances would be quenched through the direct interaction with the substrate and be imperceptible in the spectra. The energy of the π(C≡N*) resonance for NC/Au(111) is close to the analogous value for the NC-alkyl SAMs on Au(111), viz. 399.75 eV (independent of chain length.[37]

The 90°-20° difference spectrum in figure 4.18b exhibits a pronounced, positive peak at the position of the π(C≡N*) resonance suggesting, in view of the orientation f the respective molecular orbitals (perpendicular to the C≡N axis), an upright orientation of the nitrile groups in NC/Au(111).

4.1.4.3. AES and RAES

Nitrile groups have been used in the previous chapters and studies as the starting point for electron transfer / electron transfer (ET) trough the molecular framework in SAMs on conductive substrates.[33,37–39,186,188] These functional groups were attached to the molecular backbone as a tail moiety at the SAM-ambient interface, while the molecules were coupled to the substrate (Au(111)) by the thiolate anchor. The ET was triggered by the resonant excitation of the N 1s electron into the π(C≡N*) orbital and monitored by RAES within the CHC approach.[27,29,189–191] Within this approach, different de-excitation channels of the [N 1s]π^* state are followed, viz. the emission of the excited electron (participator channel; P), emission of another electron from occupied valence molecular orbital (spectator channel; SP), and ET of the excited electron to the substrate, all accompanied by and interband transition from occupied valence

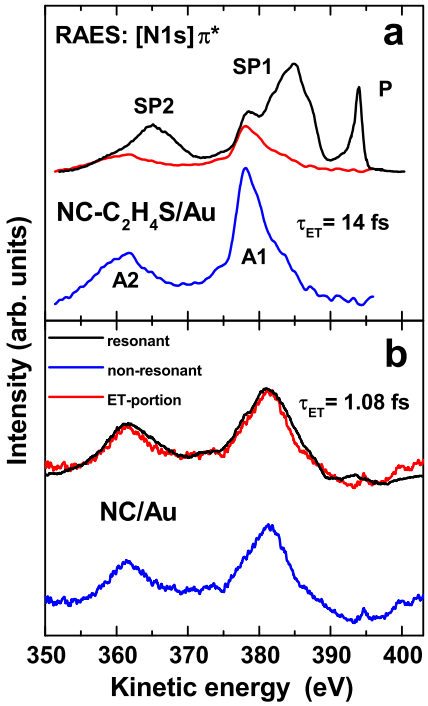

Figure 4.19.: [N 1s]π^* resonant Auger electron spectra (black curves) and non-resonant Auger electron (blue curves) spectra of NC$-C_2H_4$S/Au (a) and NC/Au(111) (b). The electron transfer contribution in the resonant Auger electron spectra is shown (red curves). P, SP1 and SP2 denote the participator and two spectator features. A1 and A2 denote two characteristic features in the non-resonant spectra. The derived τ_{ET} are given. The spectra of NC$-C_2H_4$S/Au are reprinted with permission from [37]. Copyright (2010) American Chemical Society.

molecular orbital to the N 1s hole. The P and SP processes, which are the standard de-excitation routes for RAES, result in one hole (1h) and two-hole one-electron (2h1e) states. In contrast, the ET scenario results in a 2h state, which is almost identical to the final state of non-resonant Auger electron emission process[185] (see figure 3.9 in the experimental chapter for a detailed description and schematic illustration of the processes and their spectroscopic signatures). Using the following equation (described and explained before in equation 3.2)

$$\tau_{ET} = \tau_{core}(1 - P_{ET})/P_{ET} \tag{4.4}$$

with the N 1s core hole lifetime τ_{core} of 6.4 fs,[29] providing access to the femtosecond time domain without use of any complex experimental setup relying on pump-probe techniques, τ_{ET} can be evaluated.

The length of the molecular backbone in the CHC experiments on nitrile-substituted SAMs was varied, with P_{ET} increasing and τ_{ET} decreasing progressively with decreasing backbone length.[37,38,186] In particular, τ_{ET} varied from 100±26 fs for NC−C_4H_8S/Au to 30±9 fs for NC−C_3H_6S/Au to 14±4 fs for NC−C_2H_4S/Au.[37] Further, in the extrapolated limit of the negligible short backbone, the characteristic time for ET from the NC group directly attached to the thiolate anchor to the substrate was found to be ∼2.3 fs[37] and ∼2.8 fs[38] in independent experiments on different systems, being ∼2.5 fs on average. In this context, NC/Au(111) represents a further, ultimate case, with exclusion of the *intermediate* thiolate moiety and direct attachment of the nitrile group to Au(111) with C−Au bond. Under these circumstances, ET to the substrate should be especially efficient, most likely following the major de-excitation channel of the [N 1s]π^* state.

This efficient ET to the substrate is the case, as shown in figure 4.19, where the [N 1s]π^* RAES spectra and corresponding AES spectra for NC/Au(111) are presented, along with the analogous data for NC−C_2H_4S/Au(111),[33,37] for comparison. The RAES spectra of NC−C_2H_4S/Au(111) are dominated by the SP and P contributions, while the ET part, shown separately, contributes only ∼30% of the entire spectral weight. In contrast, the RAES and AES spectra of NC/Au(111) are almost identical suggesting that the former spectra are dominated by the ET contribution, while the SP and P parts are barely perceptible. Taking the RAES spectrum of NC−$C_{16}H_{32}$S/Au(111) as the reference for the purely resonant (autoionization) spectrum[33,37] and the non-resonant AES spectrum of NC/Au(111) as representative for the ET process, the RAES spectrum of NC/Au(111) can be decomposed into the SP/P and ET contributions and τ_{ET} can be calculated according to the major formula of the CHC approach (equation 4.4). Three independent sets of experiments resulted in τ_{ET} values of 0.25, 1.08 and 1.38 fs, giving 0.9 fs on average. The accuracy of this value is ±0.5 fs from the statistical point of view and ±0.25 fs based on the accuracy of the τ_{core} value.[29] The comparison of this value with the analogous values for NC−$(CH_2)_2$S/Au is given in figure 4.20. The most important feature is the dominance of the ET process over the SP/P contributions in the [N 1s]π^* decay spectrum of NC/Au(111), suggesting strong coupling to the substrate. Another important result, it is an ultimate proof for the CHC approach in its specific application to SAMs, based on the resonantly addressable NC group.[33,37–39,186,188] As can be expected, the value of τ_{ET} for the direct attachment of the nitrile group to the Au(111) substrate is noticeably smaller than that for any molecular backbone, e.g., 14.4 fs for NC−C_2H_4S/Au[33,37] and 9±3 fs for NC−C_6H_4S/Au,[38] fitting well to the proposed exponential dependence of τ_{ET} on the length of the alkyl chain derived from the NC−(CH_2)nS/Au

data (figure 4.20a). The τ_{ET} for NC/Au(111) is slightly smaller than the characteristic time for n=0, obtained from the intercept of the lnτ_{ET} plot with the y-axis, viz. 2.3 fs[37] (2.8 fs in [38]). This result is understandable since the latter value, $\tau_{n=0}$, is associated with both ET time required for transfer from the NC group to the backbone and the ET time required for transfer from the backbone to the substrate. Assuming that the former contribution is close to τ_{ET} for NC/Au(111), the latter time can be coarsely estimated at ∼1.3 fs. This value is comparable to a characteristic time of ∼320 as observed for ET from an adsorbed sulfur atom to the substrate in the $c(4 \times 2)$-S/Ru(0001) system.[191] The difference, which is reasonably small, can be explained by band alignment differences, the stronger bonding of the S atoms to the substrate in the latter case, as well as by the different characters of the involved orbitals serving as the starting point for ET in both cases. It is well known that the character of the primary molecular or atomic orbital affcts the efficiency of ET.[38,39]

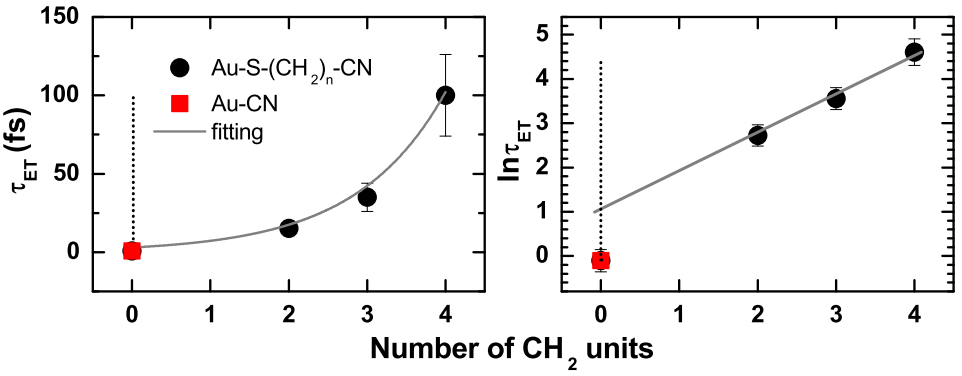

Figure 4.20.: The electron transfer (ET) time (left panel) from the excited NC group to the substrate and its natural logarithm (right panel) for NC/Au (red square) and NC−$(CH_2)_n$S/Au (n=2-4; black filled circles) versus the number (n) of methylene (CH_2) units in the aliphatic chain. The gray solid lines in the left and right panels represent the best exponential and linear fits, respectively. The intercept of the lnτ_{CT} plot with the y-axis corresponding to the ET time required for transfer from the NC group to the backbone plus the ET time required for transfer from the backbone to the substrate. The intercept of 0.83 gives a $\tau_{n=0}$ of 2.3 fs. The values for NC−$(CH_2)_n$S/Au are reprinted with permission from [37]. Copyright(2010) American Chemical Society.

4.1.4.4. Discussion

Combining the structural and spectroscopic measurements with known Au-cyanide chemistry, we propose a bonding scheme for cyanide monolayers on Au(111). Assuming that the molecules on the surface organize to maximize intermolecular interactions for monolayer stability, and to offset unfavorable dipole coupling,[234] we propose a bonding scheme were the cyanide molecules are bound via an Au−C bond and are oriented normal to the surface. Note that when cyanide is attached to a carbon backbone as a nitrile group, it has an inclined orientation measured around 65°[37,211] suggesting that the strength of the substrate-molecule bond is dominant over the intermolecular interactions and overpowers the unfavourable dipole-dipole interactions.

Finally, from the CHC results measuring the ∼1 fs charge transfer from the cyanide directly to the gold, as shown schematically in figure 4.21, we can infer that the electronic coupling is particularly stron between the carbon and gold based on the facile electron transfer. This result directly supports the expected dominance of σ bonding suggested by the increase in CN vibrational frequency (see IR and RAMAN results in the Appendix figure A.7). The electron transfer efficiency, coupled with the molecule orientation, is and indication that there is a favorable energetic overlap between the molecular transport orbitals and substrate Fermi level[235] and follows the trend for electron/charge transfer time as a function of the length of the carbon backbone in nitrile functionalized alkanethiol SAMs previously shown in figure 4.20.[37] In fact, complementary to these results, it has been reported that the conduction efficiency is significantly lower for isocyanide or Au−NC bound molecules.[236]

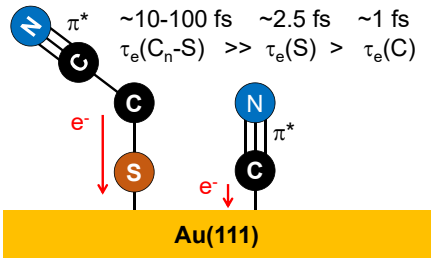

Figure 4.21.: Electron transfer across the Au−C bond is extremely efficient at ∼1 fs indicating strong electronic coupling between substrate and molecule.

4.1.5. Pyridinethiols

The molecules, forming the SAMs analyzed in this section, are displayed in figure 4.22. In this section, their spectroscopic analysis along with the investigation of the respective electron transfer dynamics is presented.

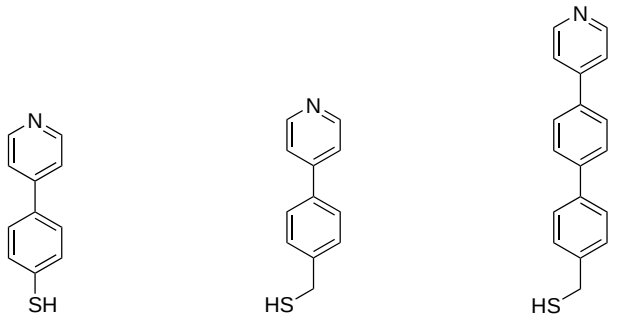

(a) (b) (c)

Figure 4.22.: Structure of the projects' molecules along with their assigned acronyms (a) PyrP0SH (b) PyrP1SH (c) PyrPP1SH

4.1.5.1. XPS and HRXPS

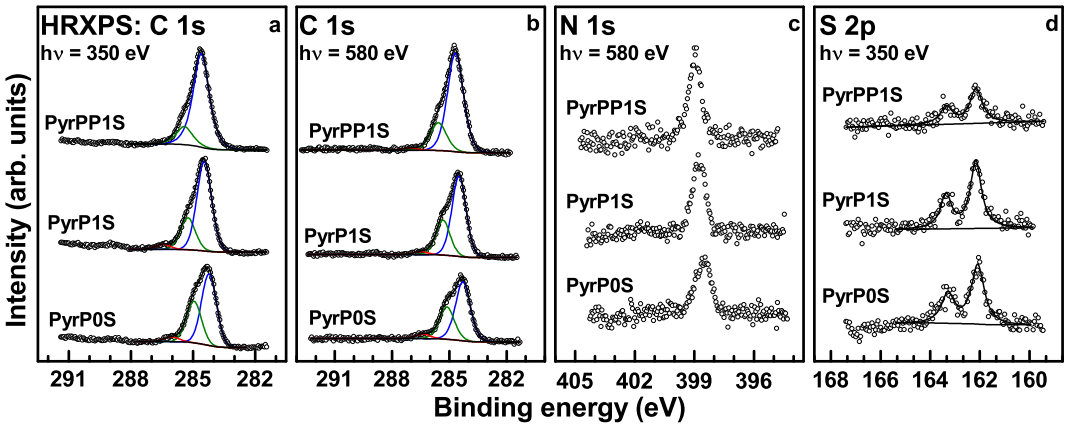

Figure 4.23.: Synchrotron-based C 1s (a) + (b), S 2p (c) and N 1s (d) XP spectra of the pyridine-based SAMs acquired at photon energies of either 350 eV or 580 eV as marked in the panels (open circles). The fitting of the spectra is shown (thin green, red and blue solid lines), including the respective background (thin black solid lines).

Synchrotron-based C 1s, S 2p, and N 1s XP spectra of the pyridine-based monolayers are presented in figure 4.23. The S 2p spectra in figure 4.23c

are dominated by the characteristic S $2p_{3/2,\ 1/2}$ doublet at a E_B position of ∼162.1 eV, which corresponds to the thiolate species, bound to gold.[89,173,197]

The N 1s spectra in figure 4.23c exhibit a major peak at a E_B of ∼398.8 eV, attributed to the free nitrogen atom in the pyridine ring.[237] The weak broadening to higher binding energies in the case of PyrP0S and PyrP1S can be assigned to a weakly coupled H atom at the pyridine nitrogen (∼399.2 eV).[233] Due to the combination of the clear nitrogen signal and the sulfur spectra, showing only thiolate-coupled species, it can be concluded that all molecules are coupled to the substrate via Au−S bonding and the nitrogen atom is located at the SAM-ambience interface.

For the reproduction of the C 1s spectral shape (figures 4.23a and b) three components can be assigned. The most intense signal **1** at ∼284.5 eV can be assigned to the phenyl rings and meta positions of pyridine, the green fit (**2**) at ∼285.4 eV shows contributions of the ortho and para positions of pyridine and the spacer molecule in PyrP1S and PyrPP1S. The third, very small, contribution at a E_B of ∼286.4 eV (red thin fit) shows the effect of protonation at the nitrogen and influence on the ortho and para positions of the pyridine.[234] The assignment of the positions goes in line with the change in peak intensity comparing the different spectra acquired at either 350 eV or 580 eV. This happens, because the larger inelastic mean free path (IMFP) at higher kinetic electron energies favors photoemission from the inner part of the sample (CH_2-spacer and phenyl) compared to that from the outer surface of the sample (pyridine moiety).

According to the attenuation of the Au $4f_{7/2}$ signal, the respective effective thickness of the films was evaluated and compiled in table 4.6. The value

Table 4.6.: Film thickness and packing density derived from laboratory XPS data.[a]

monolayer	effective thickness (Å)	packing density (molecules/cm^2)
PyrPP1S	17.67	5.05×10^{14}
PyrP1S	12.02	4.60×10^{14}
PyrP0S	11.05	3.77×10^{14}

[a] Error bars can be estimated at ±5%

for PyrP0S of 11.05 Å is in accordance with the thickness of the biphenylthiolate SAMs on gold (11 Å)[202] and comparable to previously found values of 10.4 Å.[233] The additional CH_2 moiety in PyrP1S increases the effective film thickness by 1.03 Å to 12.02 Å. This increase is in line with the literature value of 1.26 Å[91] per CH_2 moiety. For the PyrPP1S molecule it is the same, as the

effective film thickness of 17.67 Å is slightly different from the effective film thickness (16±1.5 Å)[238,239] of the terphenyl analog with a CH_2 spacer.

4.1.5.2. NEXAFS Spectroscopy

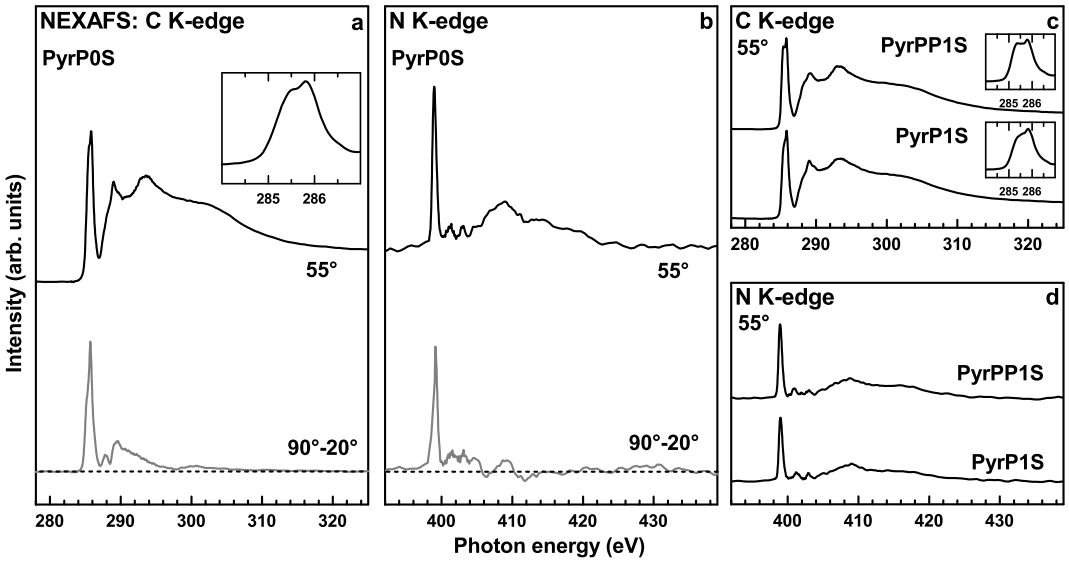

Figure 4.24.: C (a) and N (b) K-edge NEXAFS spectra of the PyrP0S acquired at an X-ray incident angle of 55° (black solid lines) along with their respective difference spectra (90°-20°; grey solid lines). The dashed line corresponds to zero. The insets in a and c magnify the most pronounced double π resonance at 55°. Spectra of PyrPP1S and PyrP1S SAMs acquired at an X-ray incident angle of 55° are exhibited in (c) and (d).

Representative C and N K-edge NEXAFS data for the PyrP0S SAM, acquired at an incidence angle of 55° are compiled in figure 4.24a and b along with their respective difference spectra (90°-20°). In figure 4.24c and d spectra of PyrP1S and PyrPP1S acquired at the *magic* angle of 55° are depicted. At this particular angle no orientational effects influence the spectrum. All C K-edge spectra are dominated by a split resonance at ∼285.6 eV. This position can be associated with with the π^* transitions in aromatic phenyl (higher PE) and pyridine (lower PE) rings. The magnified inset in figure 4.24a exhibits this split resonance.[55]. Additional resonance are at ∼288.95 eV and a broad σ^* resonance around ∼293.5 eV. The spectra are similar to literature spectra of PyrP0S on Au[233], PyrP1S on Au[55] and biphenylthiolate SAMs.[202] The pronounced linear dichroism, visible in the difference spectrum (figure 4.24a; grey line) of the PyrP0S SAM indicates an high orientation of the surface

anchored molecules in this film. Following the standard approach introduced before,[57] the average tilt angle (α_{arom}), including the pyridine and phenyl rings, obtained from the C K-edge NEXAFS data, is 67°.[55]

The N K-edge NEXAFS spectra show three separate resonances associated with the π system of the pyridine ring at ~399 eV, ~401.2 eV and ~402.9 eV. Additionally a broad σ^* resonance around ~408.7 eV is visible. The positions of the peaks and the general spectral layout of the SAMs, formed by the respective pyridine molecules, are in accordance with the literature.[233,240] The pronounced dichroism in the difference spectrum of PyrP0S supports the conclusion of the C K-edge spectrum, viz., the oriented character of the molecules in the molecular film. A calculation of the average tilt angle from the N K-edge spectrum (representative of the pyridine ring only) derives α_{pyr}=68°. Comparing this value to α_{arom} (67°), derived from the C K-edge spectrum, only a very small deviation within the error range of 3% is visible, thus, only a very small or no torsion angle between the pyridine and phenyl ring, close to a coplanar conformation, could be assumed. A comparison with calculated spectra in the literature leads to a similar conclusion.[55].

4.1.5.3. AES and RAES

The goal of the RAES experiments was to monitor ET across the molecular framework to the conductive gold substrate following the resonant excitation of the pyridine by a narrow band synchrotron radiation. The pathway is unequivocally defined by the molecular structure and the orientation in the molecular film. Comparable to the nitrile moiety, the nitrogen is located at the SAM-ambience interface.[33,36–39,57] The scheme of the core excitation and de-excitation is exhibited in figure 4.25a and was explained in detail in the experimental part and figure 3.9. The resonant excitation was performed at the N K-edge following the [N 1s]π^*. The resonances are quite intense as derived from the NEXAFS analysis in figure 4.24.

For electron transfer to the substrate, driven by the potential difference between the excited pyridine moiety and the substrate, the energy needed to resonantly excite π electrons should be higher than the E_B of the respective core electron. For the two pyridine samples PyrP0S and PyrP1S the respective E_B are ~398.5 eV and ~398.7 eV, while the energy of the π(N*) resonance is ~399 eV for both layers. Thus, ET from the excited pyridine group to the substrate is energetically allowed for both PyrP0S and PyrP1S films.

The resulting [N 1s]π_1^* spectra of the SAMs along with their reproductions by the linear combination of the purely resonant (P and SP) and the nonresonant (ET) contributions are presented in figure 4.25b and c. As a reference molecule for the pure resonant spectrum, a film of PyrPP1S on Au(111) was used (too

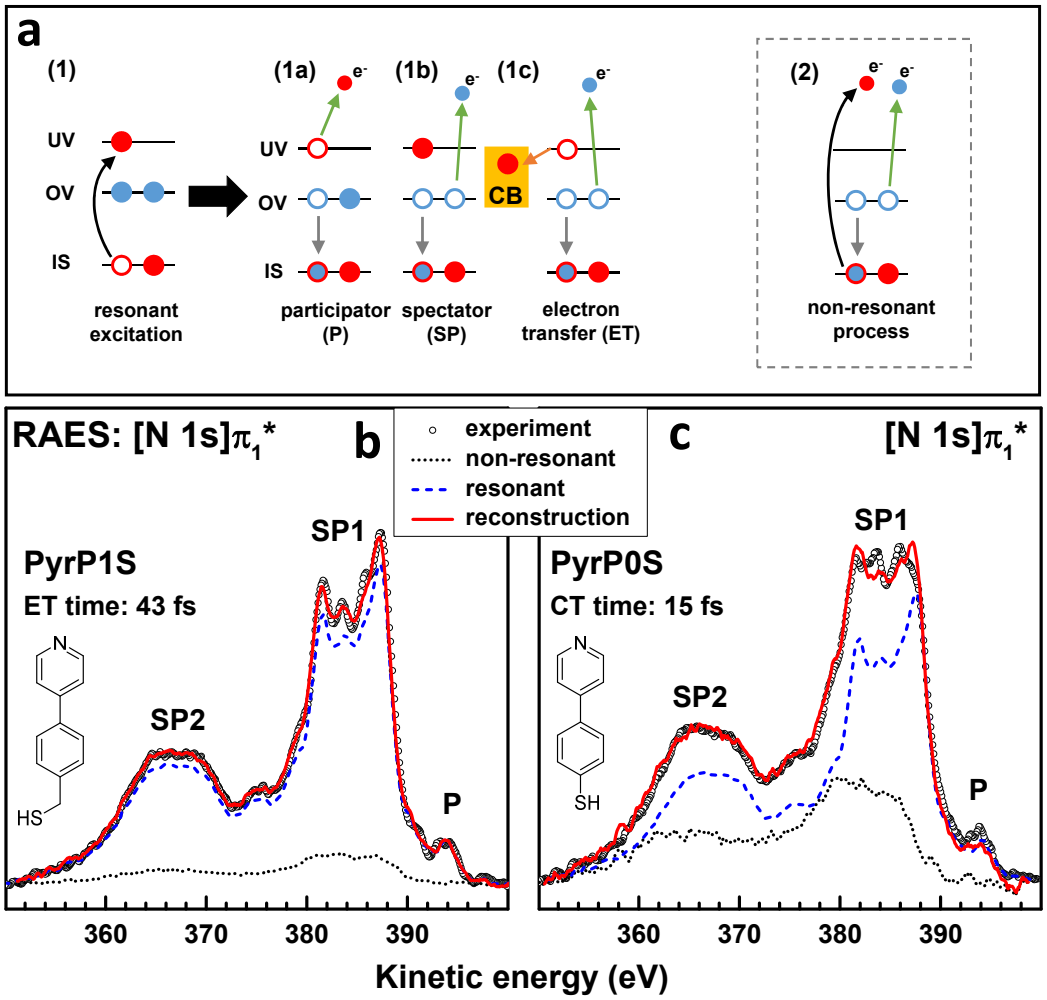

Figure 4.25.: (a) Scheme of core excitation/de-excitation routes for the pyridine group in the PyrP0S and PyrP1S SAMs in the framework of RAES. This scheme was explained in the experimental part in figure 3.9 and is added just for the sake of completeness. (b) + (c) [N 1s]π_1* RAE spectra of the PyrP1S and PyrP0S SAMs (open circles) along with their reconstructions (red solid lines) by the linear combination of the purely resonant (blue dashed lines) and non-resonant (black dotted lines) contributions. Participator (P) and spectator (SP) features are marked. The derived τ_{ET} values are given in the figures.

long for a distinct contribution of ET in the decay spectrum; comparable to NC-TPT;[38] structure in figure 4.22c). The RAE spectra of the pyridine SAMs are looking slightly different compared to the spectra, recorded in the previous

projects for SAMs formed by nitrile-substituted molecules. The left shoulder of the SP1 is more pronounced, showing similarities to the literature spectra of pyrimidine.[241]

Analysis of the spectra in figure 4.25b and c suggested that both contain a considerable contribution of the ET route, represented as an admixture of the nonresonant spectrum to the pure resonant curves. A reproduction of the experimental curves by recombination of the resonant and the non-resonant line shape exhibited P_{ET}, which was used to calculate τ_{ET} of 15±3 fs for PyrP0S and 43±7 fs for PyrP1S, using the basic equation $\tau_{ET} = \tau_{core}(1-P_{ET})/P_{ET}$[27,189–191] with τ_{core}=6.4 fs for N 1s.[29] The τ_{ET}-value of PyrP0S (15±4 fs) was slightly above the one for the nitrile-substituted analog NC-PT (9±3 fs)[38] but half of the time reported for NC-BPT (29±6 fs).[38] For the molecules with a CH_2 spacer a comparable nitrile-substituted analog to PyrP1S (43±7 fs) would be NC-PT1 (19.2±5 fs).[38] The strong conjugation of the [N 1s]π_1* of a nitrile moiety with the adjacent phenyl ring[38] exceeded the pyridine connected to the phenyl ring in τ_{ET}. However, for excitation in the pyridine moiety, shorter times for τ_{ET} were obtained than those reported for excitation in the non-conjugated [N 1s]π_3 orbital of the nitrile group in the respective analogs: ([N 1s]π_3* NC-PT; 31.5±4.5 fs and [N 1s]π_3* NC-PT1; 60±10 fs).[38]

4.1.5.4. Discussion

The spectroscopical analysis of the fabricated films (PyrP0S/Au, PyrP1S/Au and PyrPP1S/Au) with HRXPS and NEXAFS spectroscopy showed well-defined systems with upright oriented molecules indicating that the nitrogen of the pyridine moiety was positioned at the SAM-ambience interface and the molecules are connected to the substrate via the thiolate anchor. From NEXAFS spectroscopy the energies for resonant [N 1s]π* excitation for in the PyrP0S and PyrP1s films were observed. The obtained RAE spectra of the respective films showed a perceptible contribution of the ET decay route, indicating the suitability of the pyridyl moiety as an alternative to nitrile for site specific resonant excitation. From subsequent spectral decomposition and CHC calculations the specific τ_{ET} for both SAMs could be estimated. The implementation of the nitrogen into the aromatic system of pyridyl suggested that a resonantly excited electron is directly involved in the aromatic system. Thus, the ET for PyrP0S (15±4 fs) is faster than for NC-BPT (29±6 fs),[38] where the electron is excited in the nitrile group. In the latter case, the electron has to "travel" to the electronic system in the adjacent phenyl ring first, to have a comparable position as the electron in PyrP0S had after excitation, being alread involved in the aromatic system of the pyridine ring. This situation made it more reasonable to treat pyridine like a group as nitrile and compare PyrP0S (15±4 fs) and PyrP1S

(43±7 fs) to NC-PT (9±3 fs)[38]and NC-PT1 (19.2±5 fs),[38] respectively. The mentioned τ_{ET} for the nitril-substituted molecules were derived after [N 1s]π_1* excitation. The π_1 orbital of the nitrile group is parallel to, and conjugated with the π-system of the adjacent phenyl ring in NC-PT and NC-PT1.[35] Thus, τ_{ET} values for [N 1s]π_3* excitation, with the π_3 orbital being perpendicular to the π_1 and not conjugated with the adjacent ring, are higher for NC-PT and NC-PT1 ([N 1s]π_3* 31.5±4.5 fs and [N 1s]π_3* 60±10 fs, respectively),[38] indicating a lower efficiency for ET after orbital selective excitation in π_3.

For PyrP0S and PyrP1S, the respective derived τ_{ET} for [N 1s]π_1* excitation in are inbetween the above described values of τ_{ET} for [N 1s]π_1* and [N 1s]π_3* of their nitrile-substituted analogs. These findings suggested an interaction between the two adjacent rings, viz. pyridyl and phenyl, in these SAMs. Moreover, the electronic properties of molecules can be influenced by the torsion angle between adjacent rings,[222] increasing the bandgap with larger angles. In the literature, a torsion of 36° has been reported for free PyrP1 and 18°[55] was estimated for PyrP1S SAMs on gold. Although this would give first hints for an explanation of the ET properties of PyrP0S and PyrP1S, NEXAFS spectroscopy (see above) proposed a very small and nearly coplanar organisation, according to the approach used in the literature.[55] A planar conformation of adjacent orbitals greatly benefits the electronic properties, as seen for the conjugated π_1 orbital in the nitrile-substituted (oligo)phenyls.[38] At the same time a coplanar orientation of two adjacent rings increases the steric interaction of their hydrogen atoms, which leads to a prolongation of the C−C bond between the rings.[222] The C−C bond in PyrP0S is already longer (∼1.36 Å)[104] than the C−C bond between phenyl and nitrile in NC-PT (∼1.31 Å).[104] Conjugation of the −C≡N group with the adjacent ring resulting in additional shortening of the C−C bond and at the same time steric interaction of the hydrogen atoms as well as an additional prolongation due to the conformation, presumably influenced the length of the defined pathway for ET in the respective molecules and consequently the derived τ_{ET}.

Overall, the suitability of the pyridine group as an alternative to nitrile for site specific resonant excitation within the framework of CHC was proven. To support either one, or a combination of the above suggested explanations (torsion; bond length) for τ_{ET} of PyrP0S and PyrP1S, calculations of the involved orbitals and their orientation and conjugation within the molecules are needed. Similar extensive studies for the nitrile group have been reported in the literature.[38,39,57]

4.1.6. Nitro-Oligophenylthiols

The results presented in this section were published in *The Journal of Physical Chemistry C* and are adapted from [187].

The spectroscopic analysis along with the dynamic electron transfer properties of the films, formed by the molecules shown in figure 4.26, are presented and discussed in this section.

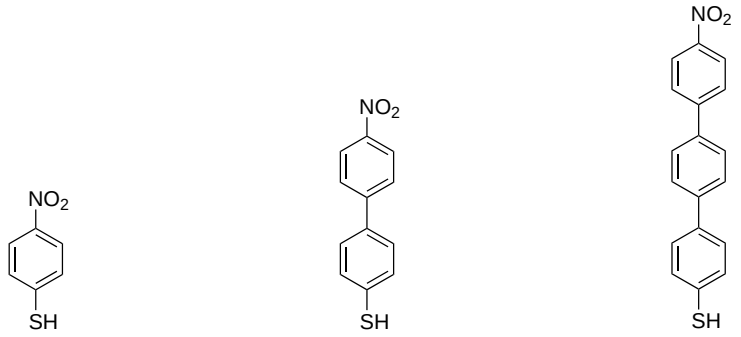

Figure 4.26.: Structures of the nPT−NO_2 molecules along with their assigned acronyms.(a) PT-NO_2 (b) BPT-NO_2 (c)TPT-NO_2

4.1.6.1. XPS and HRXPS

Synchrotron-based Au $4f_{7/2}$, C 1s, S 2p, N 1s and O 1s XP spectra of nPT−NO_2 monolayers are presented in figure 4.27. The S 2p spectra in figure 4.27c are dominated by the characteristic S $2p_{3/2,\ 1/2}$ doublet at a E_B position of ∼162 eV (S $2p_{3/2}$) for all three monolayers with only a small trace of physisorbed species for the BPT-NO_2 monolayers as well as a weak trace of atomic sulfur or differently bound molecules (a E_B position of ∼162 eV for S $2p_{3/2}$).[173] The above E_B value corresponds to the thiolate species bound to noble metal surfaces,[89,173,197] which suggests that basically all molecules in the nPT−NO_2 films were bound to the substrate via thiolate-gold bonds, as it should be the case in well-defined SAMs. The intensity of the S 2p doublet decreases with increasing length of the aromatic backbone, which agrees well with the expected attenuation of the respective photoemission signal for the intact nPT−NO_2 molecules bound to the substrate via conventional thiolate bonds; a thicker molecular film is associated with a stronger signal attenuation. Accordingly, the intensity of the Au $4f_{7/2}$ signal decreases (figure 4.27a) and the intensity of the C 1s signal (figure 4.27b) increases when passing from the PT-NO_2 to the TPT-NO_2 film.

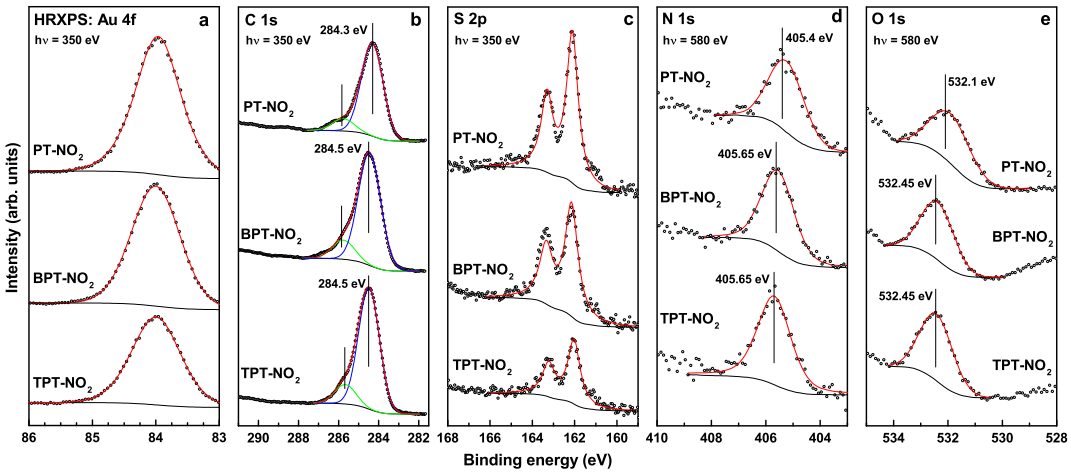

Figure 4.27.: Synchrotron-based Au $4f_{7/2}$ (a), C 1s (b), S 2p (c), N 1s (d) and O 1s (e) XP spectra of the nPT−NO_2 SAMs acquried at photon energies of either 350 eV or 580 eV as marked in the panels (open circles). The fitting of the spectra is shown (thin red, green and blue solid lines), including the respective background (thin black solid lines). The vertical solid lines in panels b, d and e highlight the E_B positions of the emissions.

The C 1s spectra are dominated by a strong emission at a E_B of 284.3 eV to 284.5 eV accompanied by a weak shoulder at a slightly higher E_B (∼285.8 eV). The dominant emission is assigned to the aromatic backbone,[173,202,242] while the shoulder at higher E_B can be mainly attributed to the terminal carbon atom bound to the electronegative nitro group (also nonsubstituted aromatic thiolate SAMs on noble metals show a weak shoulder).[173,242] No significant emissions of oxidation products, such as C−O, C=O and COOH could be found for nPT−NO_2 sample. The position of the major emission shifts to higher E_B when passing from the PT-NO_2 to BPT-NO_2 film, which can be explained by the different screening of the photoemission hole by the substrate electrons (a well-known final state effect, extra-atomic relaxation).[176] The extent of screening depends on the separation between the hole and the substrate and is therefore stronger for the thinner PT-NO_2 film as compared to the thicker BPT-NO_2 and TPT-NO_2 monolayers.

Similar effects are also observed in the N 1s (figure 4.27d) and O 1s (figure 4.27e) spectra, which are characteristic of the nitro tail group. For all three of the studied systems, these spectra exhibit only one emission, suggesting a homogeneous character of the SAM-ambience interface. The position of this emission in both spectra (N 1s and O 1s) shifts to higher E_B when going from the PT-NO_2 to the BPT-NO_2 film, following the decreasing screening. A larger

shift, when looking at the TPT-NO_2 monolayer, does not occur, because of the short-range character of the effect (only PT-NO_2 is really affected).

The above analysis of the XP spectra was complemented by their numerical evaluation. Based on the C 1s to Au 4f ratio, the effective thickness of the nPT−NO_2 monolayers was calculated, using a standard procedure described in section 3.2.1.2.[199] The derived values of the effective thickness are ∼8.9 Å, ∼13.5 Å and ∼17.6 Å for the PT-NO_2, BPT-NO_2 and TPT-NO_2 monolayers, respectively (see table 4.7) These values correlate well with the respective molec-

Table 4.7.: Film thickness and packing density derived from the laboratory XPS data.[a]

monolayer	effective thickness (Å)	packing density (molecules/cm^2)
PT-NO_2	8.9	3.9×10^{14}
BPT-NO_2	13.5	4.5×10^{14}
TPT-NO_2	17.6	4.3×10^{14}

[a] Error bars can be estimated at ±5%

ular dimensions of 6.6 Å, 11.0 Å and 15.2 Å after adding the S−Au bond length of ∼2.4 Å,[178,243] which takes the molecular assembly on the substrate into account. This correlation suggests upright molecular orientation with a small inclination for all three studied monolayers.

From the intensity ratios of the S 2p and the Au 4f emissions, the packing densities in the nPT−NO_2 monolayers were calculated following the approach in the literature.[179,180] As a reference system with well-known packing density of 4.63×10^{14} molecules/cm^2 or 0.216 nm^2/molecule, DDT on Au(111) was used. The calculated values for the packing density are summarized in table 4.7. These values are close to the packing density of the DDT monolayer, which suggests a dense molecular packing. The density values for the BPT-NO_2 and TPT-NO_2 are slightly higher than for the PT-NO_2 monolayers, which is understandable regarding the larger energy gain upon the assembly of the longer molecules. Such an energy gain represents on of the major driving forces for the self-assembly.

4.1.6.2. NEXAFS Spectroscopy

The carbon, nitrogen and oxygen K-edge NEXAFS spectra of the nPT−NO_2 monolayers are presented in figures 4.28, 4.30a and b, respectively. At first, spectra acquired at the so-called *magic* angle of X-ray incidence (55°) are depicted. At his particular geometry the spectra are free of orientational effects

and are representative of only the electronic structure of the studied systems.[184] Secondly, the difference between the spectra acquired at normal (90°) and grazing (20°) incidence of X-rays, which is representative of the so-called linear dichroism, is shown. The C K-edge NEXAFS spectra of the nPT−NO_2 mono-

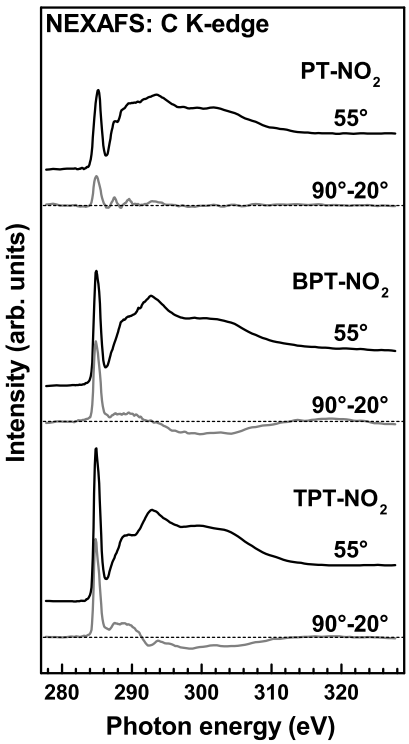

Figure 4.28.: C K-edge NEXAFS spectra of the nPT−NO_2 SAMs acquried at an X-ray incident angle of 55° (back solid curves), along with the respective difference between the spectra collected under normal (90°) and grazing (20°) incidence geometry (gray solid curves). The characteristic absorption resonaces are marked. The horizontal dashed lines correspond to zero.

layers are presented in figure 4.28. They are representative of the molecular backbones. The spectra are dominated by a pronounced absorption resonance at ∼285.0 eV (π_1*), which exhibits a successive increase in relative intensity and a slight narrowing when passing from the PT-NO_2 to TPT-NO_2 film, typical of aromatic thiolate SAMs on noble metal substrates.[197,202] This behaviour is assumed to be related to the interaction with the substrate, because neither the intensity, nor the width of the π_1* resonance is affected by the length of the oligophenyl chain for thick, evaporated films of the substances.[201] The π_1* is accompanied by several weaker and broader resonances at ∼287.6 eV (mixture of R* and C−H*), ∼289.0 eV (π_2*), ∼293.0 eV (σ_{C-C}*), ∼297.0 eV (σ_{C-C}*)

and ∼305.0 eV (σ_{C-C}*).[184,200–202,244–246] The TDMs of the molecular orbitals related to the π_1*, R* and π_2* resonances are believed to be oriented perpendicular to the phenyl rings.[200,201,244] In contrast, the TDMs of the σ_{C-C}* resonances are assumed to be oriented along the molecular axis.[200,201,244] In accordance with these orientations and expected upright molecular arrangements in the nPT−NO_2 monolayers (previously mentioned), the π_1*, R* and π_2* resonances exhibit positive anisotropy peaks, while the σ_{C-C}* resonances show negative anisotropy peaks in the 90° − 20° curves. Note that both biphenyl and terphenyl moieties exhibit a dihedral rotation of individual rings in the molecular state. It is believed that this rotation decreases and disappears in the respective bulk materials[247–250] and densely packed 2D assemblies.[35,251] An almost planar conformation of the molecular backbones can be expected in all nP−NO_2 SAMs.

Along with the qualitative considerations, a quantitative analysis of the entire set of the NEXAFS spectra was performed. For this analysis we used the most prominent π_1* resonance and standard theoretical framework for a vector-type orbital.[184,202] The derived average tilt angles of the π_1* orbital of the molecular backbones in the nPT−NO_2 monolayers are summarized in table 4.8. These values can be used to calculate the average tilt angles of the molecular

Table 4.8.: Average tilt angles of the π_1*(oligophenyl) and π*(NO_2) orbitals as well as the respective average tilt angles of the molecular backbone (twist angle of 32° assumed).[a]

monolayer	π_1*(oligophenyl)	$\pi(NO_2)$	backbone
PT-NO_2	62°	68°	29°
BPT-NO_2	69°	74°	22°
TPT-NO_2	67°	70°	25°

[a] Error bars can be estimated at ±3°.

backbones, as far as the so-called twist angle γ,[35,209] describing the rotation of the backbone along the molecular axis in relation to the tilt direction, is known (figure 4.29). The latter parameter can be measured directly only in selected cases[35,57,252] but is reasonably assumed to be close to the analogous value for the bulk biphenyl and terphenyl (32°).[35,247–250,252] The average tilt angles of the molecular backbones in the nPT−NO_2 monolayers, calculated within this assumption, are compiled in table 4.8. The values for the BPT-NO_2 and TPT-NO_2 monolayers are close to one another, while PT-NO_2 SAMs exhibit slightly larger molecular inclination.

The N K-edge NEXAFS spectra of the nPT−NO_2 films are presented in

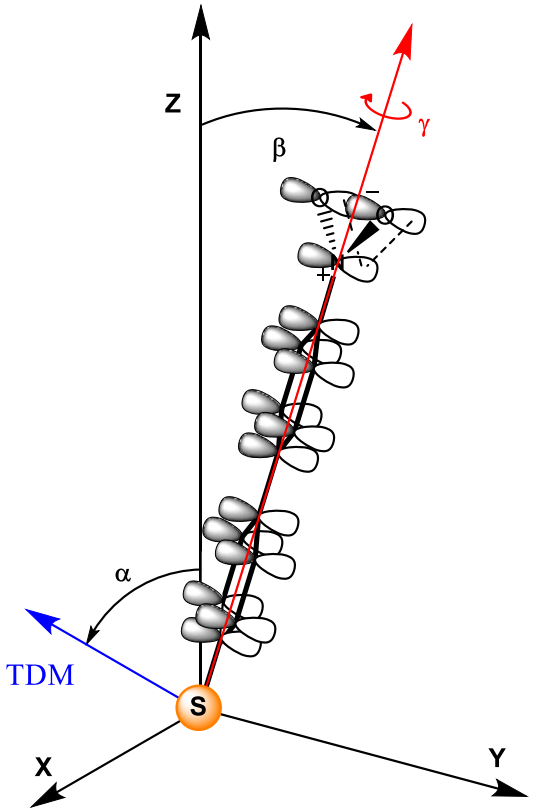

Figure 4.29.: Schematic drawing of the orientation of the BPT-NO_2 molecules in the respective SAMs, representative also of the PT-NO_2 and TPT-NO_2 monolayers. The dihedral rotation is expected to be lifted; the plane of the nitro group is assumed to be parallel to the plane of the adjacent phenyl rin (see text for details); accordingly, the π^* orbitals of the nitro group are parallel to the $\pi_{ph}{}^*$ orbitals. The backbone tilt angle β and twist angle γ describe the molecular orientation. The $\pi_{ph}{}^*$ orbitals of the biphenyl backbone are perpendicular to the ring plane; the respective transition dipole moment TDM_π is shown as a blue arrow; its orientation is given by the angle α. At $\gamma = 0$, TDM_π lies in the plane spanned by the z- and 4,4'-axes. The angles are related by the equation $cos(\alpha) = sin(\beta) \times cos(\gamma)$.[209]

figure 4.30a. These spectra are representative of the nitro tail group. They are dominated by a sharp π^* resonance at ~403.55 eV accompanied by a variety of weaker and broader resonances at higher photon energies. The spectra agree well with literature data for the analogous systems.[54,253] The TDM of the molecular orbitals related to the π^* resonance are believed to be oriented

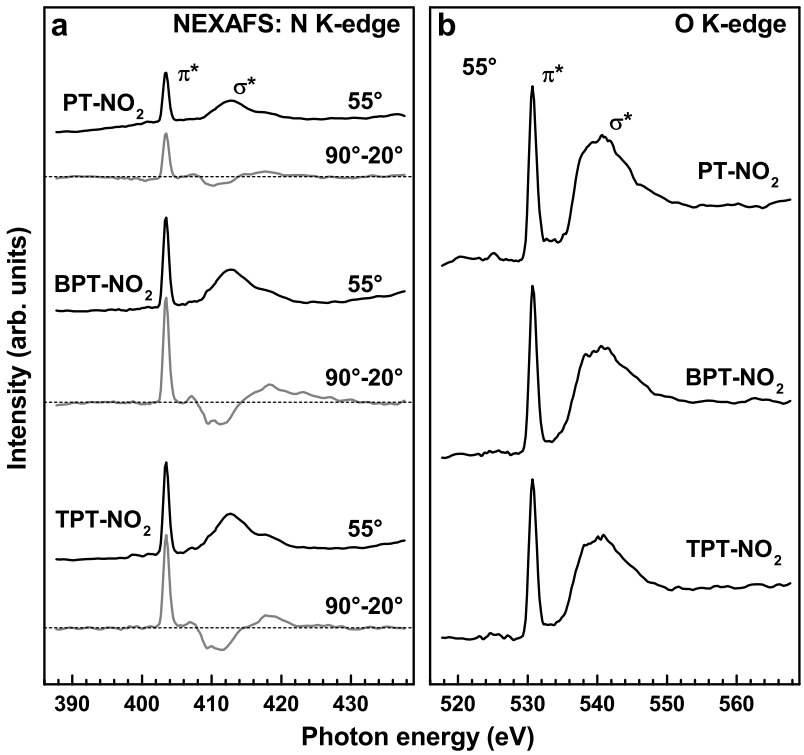

Figure 4.30.: N K-edge NEXAFS (a) and O K-edge (b) spectra of the nPT−NO_2 SAMs acquried at an X-ray incident angle of 55° (back solid curves). N K-edge along with the respective difference between the spectra collected under normal (90°) and grazing (20°) incidence geometry (gray solid curves). The horizontal dashed lines correspond to zero. The characteristic absorption resonances are marked.

perpendicularly to the plane of the nitrile moiety. Due to the rigidity of the oligophenyl backbone, the directional character of the ring−NO_2 bond and presumable conjugation of the π systems of the nitro moiety and the adjacent phenyl ring, the plane of this moiety should be oriented parallel to the ring plane. Accordingly, for all nPT−NO_2 monolayers, the π^* resonance exhibits a positive anisotropy peak in the $90° - 20°$ curves, mimicking the behaviour of the π^* resonances of the phenyl rings at the C K-edge. Numerical evaluation of the entire set of the N K-edge NEXAFS spectra within the standard theoretical framework for a vector-type orbital[184] results in the average tilt angles compiled in table 4.8. These angles are slightly higher, but close to the analogous values for the π_1^* orbitals of the oligophenyl backbone. The observed difference is believed to be related to a systematic error of the evaluation procedure, which, in the case of N K-edge spectra in particular, relies on only one

nitrogen atom per molecule. Consequently, a strong change in the background after variation of the X-ray incidence angles can affect the evaluation of the spectra. To be on the safe side, we have just calculated the average over the oligophenyl-derived and nitro group-derived angle values for each of the studied monolayers and compiled them in table 4.8 as the average tilt angles of the entire molecular backbone.

The O K-edge NEXAFS spectra of the nPT−NO_2 monolayers are presented in figure 4.30b. Similar to the N K-edge data, these spectra are representative of the nitro tail group. They are dominated by a sharp π^* resonance at ∼530.95 eV accompanied by broad σ^* resonances at higher photon energies. The spectra agree well with literature data for analogous systems.[54,253] For this particular edge, only magic angle (55° incidence) spectra have been measured as the orientation of the nitro group was monitored using the N K-edge.

4.1.6.3. AES and RAES

The ultimate goal of the RAES experiments was to monitor electron transfer across the molecular framework to the conductive gold substrate following the resonant excitation of the nitro tail group by a narrow band synchrotron radiation. The chemical composition of this group and its location in the SAM-ambience interface define the ET pathway clear without ambiguity, similar to the case of the nitrile group.[33,36–39,57] The schematic of possible core excitation & de-excitation scenarios for a resonant (RAES) and nonresonant (AES) excitation of the nitro tail group is presented in figure 4.31 (corresponding to figure 3.9 in the experimental chapter), along with the respective abbreviations and explanations. As mentioned above, for the nitro group the resonant excitation can be performed at both, the N and O K-edges following the [N 1s]π^* and [O 1s]π^* scenarios, respectively. The π^* resonances at both of these edges are narrow and quite intense (see figures 4.30a and b). Therefore the photon energy could be adjusted well and controlled excitation was possible. As far as ET to the substrate during the lifetime of the excited state occurs to a noticeable extent, which can be expected at least for the phenyl backbone,[38] an RAES spectrum represents a superposition of the pure auto-ionization spectrum and the ET contribution. The former spectrum can be directly measured using a reference sample where ET is energetically forbidden or occur to a negligible extent only. Due to the length of the molecular backbone, the TPT-NO_2 monolayer should exhibit a negligible extent of ET and was chosen in the present case.[38] The ET contribution can be also measured, using a nonresonant excitation at the same absorption edge. The final states of nonresonant excitation (A in figure 4.31) and the ET decay route after resonant excitation are identical. Accordingly, the spectra should be identical as well.

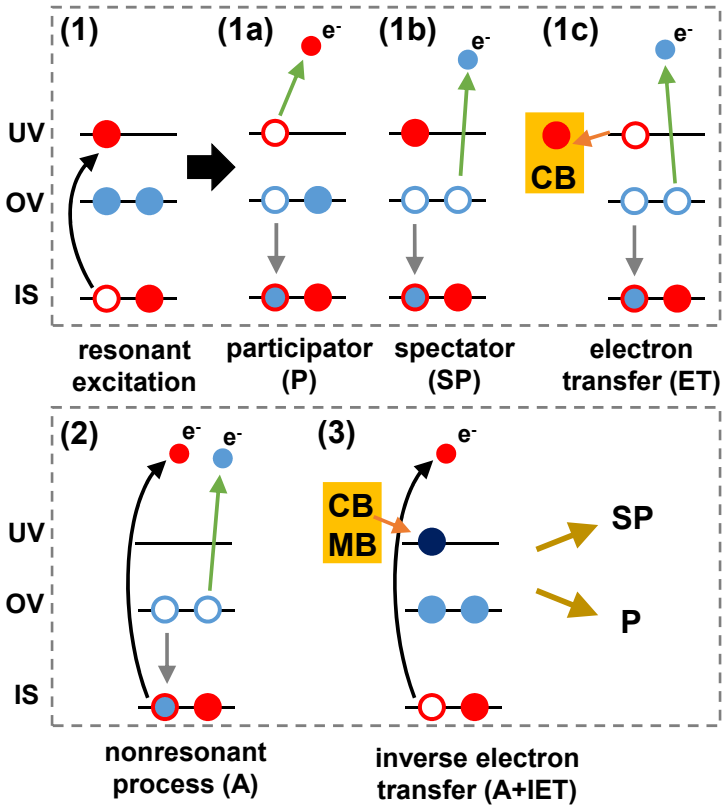

Figure 4.31.: Schematic of core excitation & de-excitation scenarios for the resonant (1) and nonresonant (2) excitation of a functional group weakly coupled to a continuum. Corresponding to figure 3.9 in the experimental chapter, adding an alternative route (3): inverse ET (IET) from the conduction band (CB) or molecular backbone (MB) to the unoccupied valence level (UV), which can occur during the lifetime of the excited state, resulting in the same intermediate situation as in the case of the resonant excitation, with subsequent decay through the participator (P) and spectator (SP) channels.

ET from the excited tail group to the substrate is driven by their potential difference. In other words, by the energy of the resonantly excited electrons with respect to Fermi level (E_F) of the substrate.[33] For efficient electron transfer, the π-resonance excitation energy should be higher than the binding energy of the respective core electron. When looking at the XPS and NEXAFS data (sections 4.1.6.1 and 4.1.6.2), it is the other way around for N and O K-edges. The energy of the $\pi(N^*O_2)$ resonance is ~403.55 eV for all nPT$-NO_2$ monolayers, which is lower than the N 1s E_B, namely 405.4 eV and 405.65 eV for

the PT-NO_2 and BPT-NO_2/TPT-NO_2 SAMs, respectively (see figure 4.27d). Similarly, the energy of the $\pi(NO^*_2)$ resonance is ∼530.95 eV for all nPT−NO_2 monolayers, which is lower than the O 1s E_B, namely 532.1 eV and 532.45 eV for the PT-NO_2 and BPT-NO_2/TPT-NO_2 SAMs, respectively (see figure 4.27e). According to these findings, an electron transfer from the excited tail group to the substrate is energetically forbidden for all nPT−NO_2 SAMs, which is probably related to the strong electronegativity of the nitro group. On the contrary, a process, which is schematically depicted in figure 4.31 (A+IET), the neutralization of the core ionized state by electron transfer from the substrate or the molecular backbone, should be possible. The [N 1s]π^* RAES spectra of

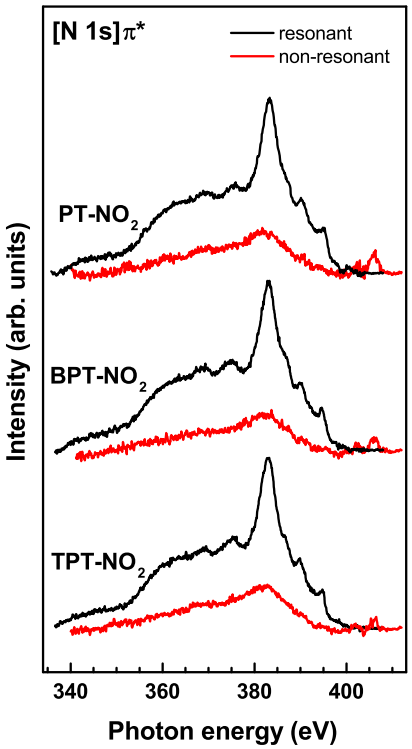

Figure 4.32.: [N 1s]π^* RAES spectra of the nPT−NO_2 SAMs (black solid line), along with the respective nonresonant AES spectra (red solid lines). The energy for the nonresonant excitation was set at ∼4.5 eV above the position of the π^* resonance.

the nPT−NO_2 SAMs are presented in figure 4.32, along with the correspondent nonresonant spectra. The RAES spectra exhibit a variety of distinct features associated with the participant and spectator de-excitation channels and are dominated by a sharp peak at ∼383.2 eV. This peak is most likely assigned to the spectator decay route, because the respective features are usually more

intense as the participator ones (see reference [38] for example). The [N 1s]π^* spectra of the three nPT$-NO_2$ species are almost identical, which indicates that there are no backbone-length-dependent ET contributions as compared to the analogous nitrile-substituted systems.[38] On the basis of previous observations for the latter, this is especially significant for the PT-NO_2 film, where a relevant contribution should be clearly visible.[38] This contribution is ∼42% in case of a strong conjugation between the π^* systems of the tail group and the adjacent ring,[38] but even if such a conjugation does not occur and the relevant molecular orbital is localized at the tail group, the ET contribution is ∼17%,[38] which should be detectable in the RAES spectrum of the PT-NO_2 film (figure 4.32). Following the above mentioned energetic considerations, ET to the substrate following the [N 1s]π^* resonant excitation of the nitro tail group dos ot occur in the nPT$-NO_2$ monolayers, including the shortest molecule of this study (PT-NO_2). The [N 1s]π^* spectra also show no traces of the IET process. The [O 1s]π^* RAES spectra of the nPT$-NO_2$ SAMs are presented in figure 4.33a and 4.34a, along with the corresponding nonresonant spectra. The spectra of the nPT$-NO_2$ systems were acquired from to different sets of samples at two different synchrotron radiation facilities. The only varied parameter was the photon energy for the acquisition of the nonresonant spectra. In the first case (figure 4.33) this energy was set to ∼8.5 eV above the position of the π^* resonance, similar to the [N 1s]π^* experiments. This excitation lies within the σ^* resonance, which is quite intense in the O K-edge spectra (figure 4.30b). Therefore, we were not completely sure of the pure, nonresonant character of the AES spectra acquired under the above conditions and repeated the entire set of the experiments with a larger photon energy shift in the nonresonant case (∼16.5 eV). This was also important to identify the stochastic features perceptible in some of the spectra after several processing steps. Note that in contrast to the nonresonant spectra, the resonant excitation in the experiments at both synchrotron radiation facilities was performed at the same photon energy, corresponding to the position of the intense π^* resonance in the O K-edge NEXAFS spectra (figure 4.30b). As seen in figures 4.33a and 4.34a, the [O 1s]π^* decay spectra of all nPT$-NO_2$ SAMs are dominated by two sharp and intense peaks at ∼515.2 eV and ∼519.1 eV accompanied by several less intense and broader features. The dominant peaks can most likely be assigned to the spectator decay route as mentioned above. Similar to the [N 1s]π^* case, the [O 1s]π^* spectra of the PT-NO_2, BPT-NO_2 and TPT-NO_2 SAMs are almost identical, which excludes the backbone-length-dependent contribution of the ET decay channel and suggests that no electron transfer from the tail group to the substrate took place. There are possible traces of the IET process in the nonresonant spectra. In the given case, these spectra exhibit not only

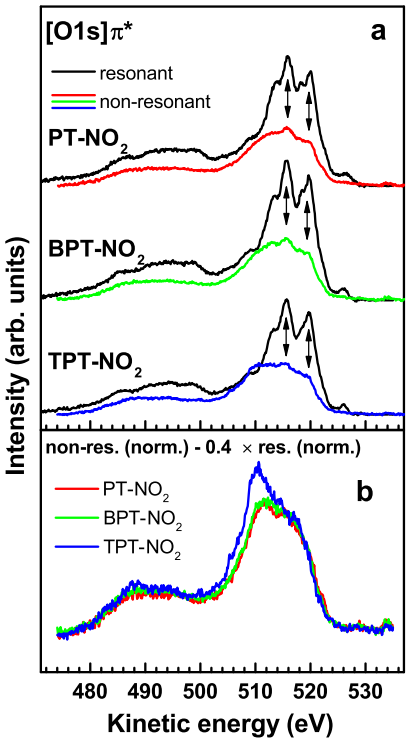

Figure 4.33.: (a) [O 1s]π^* RAES spectra of the nPT$-NO_2$ SAMs (black curves), along with the corresponding nonresonant spectra (red, green and blue curves) (b) difference between the nonresonant and weighted (by a factor of 0.4) RAES spectra. The curves for the different films are color coded. The energy for the nonresonant excitation was set at ~8.5 eV above the position of the π^* resonance. The spectra have been acquired at BESSY II. The arrows highlight the positions of the most pronounced features in the RAES spectra.

typical broad peaks, but also distinct and rather sharp features at the positions of the dominant double peak in the resonant spectra. This correlation leads to the assumption that there is an admixture of the resonant spectra in the nonresonant case, corresponding to the IET process. To prove this hypothesis we subtracted the weighted [O 1s]π^* spectra from the respective nonresonant curves using the same empirical weighting factor (0.4) for all studied systems and both measurement series. The resulting difference spectra shown in figures 4.33b and 4.34b exhibit only broad peaks typical of nonresonant excitation and are identical for all three monolayers apart from the sharp stochastic features visible for some of the systems. These features are observed for the TPT-NO_2 monolayer within the first measurement series and for the PT-NO_2 SAM within

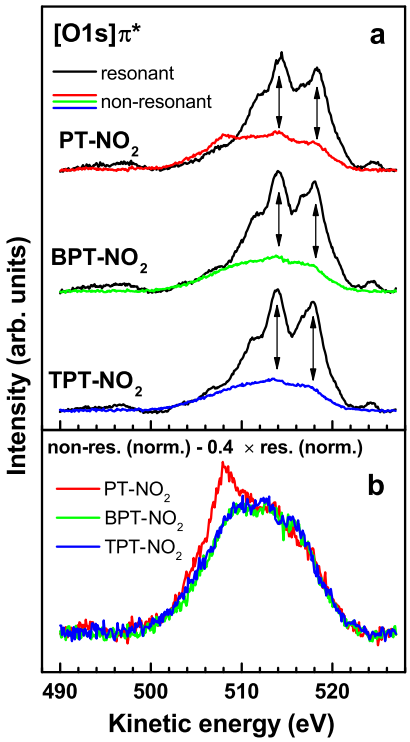

Figure 4.34.: (a) [O 1s]π^* RAES spectra of the nPT$-NO_2$ SAMs (black curves), along with the corresponding nonresonant spectra (red, green and blue curves) (b) difference between the nonresonant and weighted (by a factor of 0.4) RAES spectra. The curves for the different films are color coded. The energy for the nonresonant excitation was set at ∼16.5 eV above the position of the π^* resonance. The spectra have been acquired at MAX-lab. The arrows highlight the positions of the most pronounced features in the RAES spectra.

the second measurement series, which underlines their stochastic character. We think that these features, which are similar to the Auger lines of atomic and molecular oxygen,[254] are related to a possible, not traced minor contamination in the studied systems, which prepared by and ex situ immersion procedure. Another possible but less likely explanation is intermediate species associated with X-ray induced damage, which we tried to avoid by varying the spot position during the measurements. Verification of the stochastical character o these features was one of the main reasons for performing the [O 1s]π^* RAES experiments on two independent sample series, using two different experimental setups. The second reason was a possible effect of the excitation energy in the nonresonant case. As seen in figures 4.33a and 4.34a, this effect is minor

and only has a slight influence on the spectral appearance, whereas the major features are practically not affected.

4.1.6.4. Discussion

XPS and NEXAFS data suggest a high quality of the nPT−NO_2 SAMs. The monomolecular films are well-defined and basically contamination-free. All molecules are bound to the Au(111) substrate via the thiolate anchor and exhibit a packing density close to that of nonsubstituted alkanethiols (ATs) of the same substrate.[170,177,255] This is in accordance with the literature data, which mostly suggest the dominance of the basic $(\sqrt{3} \times \sqrt{3})R30°$ structural motif for aromatic thiolate SAMs on Au(111),[256–260] similar to the AT SAMs.[170,177,255] Thus similar packing densities can be expected. The above mentioned structural motif in the thioaromatic SAMs is mostly representative of the short-range order and is accompanied by disordered areas as well as numerous domain boundaries between the ordered regions.[256–260] Such a heterogeneous assembly should likely be the reason for the slightly lower packing density in the nPT−NO_2 SAMs as compared to the reference DDT monolayers. A similar, slightly lower packing density (4.25×10^{14} molecules/cm^2) was also observed recently in nonsubstituted biphenylthiolate SAMs on Au(111),[246] which underlines the generality of this behavior. The structural heterogeneity should be more pronounced for shorter aromatic systems, which explains the lower packing density in the PT-NO_2 case, compared to the BPT-NO_2 and TPT-NO_2 films.

Note that it is important, in particular for applications, that the nitro-substituted oligophenylthiols form well-defined monolayers as opposed to, for example, the respective carboxylic acids (i.e., carboxyl-substituted oligophenyl thiols), where the formation of hydrogen bonds between the carboxyl moieties results in the building of either disordered monolayers or bilayers.[261,262] Although attractive $NO_2 \cdots NO_2$ interactions should also occur in the nPT−NO_2 SAMs, their extent should depend on the molecular orientation of the neighboring molecules.[252,263] This orentation is assumed to be affected by the surface dipoles, which can be stabilized by a polar solvent[252,263] such as ethanol, used in the present study.

This stabilization has a positive impact on the film structure. Accordingly, the nPT−NO_2 SAMs were found to exhibit high orientational order with an upright molecular orientation characterized by the average tilt angles given in table 4.8. The angle values for the BPT-NO_2 and TPT-NO_2 monolayers are quite close to those of the analogous nonsubstituted SAMs on Au(111) (biphenylthiol (BPT) and terphenylthiol (TPT) with 23° and 20°, respectively).[202] For the latter systems, there is some variation in the reported

values. An average tilt angle of 22° was recently reported for BPT SAMs on gold[246] and values between 20° and 28° for the TPT monolayer,[202,257,261] which was critically discussed in a recent paper.[260] The reference BPT SAMs, which were measured simultaneously with the nPT−NO_2 monolayers of this study, exhibited an average tilt angle of 27°. In any case, the functionalization of the biphenyl and terphenyl backbones with the nitro tail group did not result in any deterioration of the film quality in terms of the orientational order, but rather in its improvement.

This functionalization resulted in significant improvement in the quality of the phenylthiol (PT) SAMs. According to the majority of literature data[264–266] and our groups own experience,[202,242] the quality of these films is rather poor, although there are several reports claiming the formation of a well-ordered PT monolayer on Au(111) with an upright[267,268] or strongly inclined[269] adsorption geometry of the phenyl rings. Such a poor quality is particularly emphasized by a significant molecular inclination (an average tilt angle of 49°),[202] comparably large structural inhomogeneity[242] and the presence of contamination[202,242] associated with a low efficiency of the self-cleaning process during the molecular adsorption and assembly. In contrast, the PT-NO_2 monolayers of the present study exhibit a quite low level of contamination and high orientational order emphasized by the small molecular inclination wit an average tilt angle of 29°. The improvement of the monolayer quality, compared to the nonsubstituted case, is presumably related to the constructive effect of the nitro groups. The energy contribution associated with the interaction between the electronic systems of these groups probably provides an additional thermodynamic drive to densely packed and well-ordered molecular assembly, along with a better efficiency of self-cleaning

In contrast to the nitrile-substituted aromatic thiolate monolayers,[38] the RAES spectra of the nPT−NO_2 SAMs acquired at the N and O K-edges do not exhibit any contributions related to electron transfer to the substrate. The reason for this behavior is probably the energetic situation as discussed above. On the contrary, because the π^*-resonance excitation energy at the N and O K-edges is lower than the E_B of the respective core electron, a reverse process, namely the neutralization of the core ionized state by electron transfer from the substrate or the molecular backbone is in principle possible as depicted schematically in figure 4.31 (A+IET).

Indeed there are hints of such a process for the excitation at the O K-edge. The nonresonant decay spectra shown in figures 4.33a and 4.34a exhibit, even though at low intensity, the characteristic features of the resonant spectra, which is only possible if a part of the de-excitation channels is identical with the resonant case. This requires an intermediate state, which is identical with that

for the resonant excitation. This can be easily achieved in the case of IET to the unoccupied π^* orbital, driven by the energy difference between the excited nitro group and the substrate. The IET contribution does not depend on the length of the molecular backbone, which can be directly seen in the spectra in figures 4.33 and 4.34. The same scaling factor (0.4) was required to equalize the nonresonant spectra for all studied monolayers by subtraction of the weighted resonant contribution. This means that the IET process involves exclusively the common structural unit of the PT-NO_2, BPT-NO_2 an TPT-NO_2 molecules, which is the phenyl ring adjacent to the nitro group. This is understandable in view of the comparably short lifetime of the O 1s inner shell vacancy, which should be close to the values for O_2 (∼4.4 fs)[30] and NO (3.9 fs)[31]. This *core hole clock* time scale can be compared to the characteristic ET time through the molecular framework for nitrile-substituted PT and BPT molecules arranged as SAMs on gold substrates. As far as ET starts from the π^* orbital of th enitrile group, which is conjugated with the adjacent ring, it requires either 9 fs or 29 fs to reach the substrate for the PT or BPT case, respectively,[38], which includes 2.3 fs to 2.8 fs for ET trough the S−Au anchor.[37,38] This leaves 6.5 fs and 26.5 fs for ET through the phenyl and biphenyl only. On the other hand, the basic formula[27] (equation 3.2: $\tau_{ET} = \tau_{core}(1 - P_{ET})/P_{ET}$) of the CHC approach can probably be applied to the IET process. Exchanging P_{ET} for P_{IET} and setting it to 40%, in agreement with the scaling factor, τ_{IET} was found to be 6.9 fs, which correlates surprisingly well with the ET value for the phenyl case (6.5 fs), viz. the ring adjacent to the excited tail group. This support the assumption that only this particular ring is involved in the IET process.

The fact that the IET process is observed only after excitation at the O K-edge, but is not recognizable at the excitation at the N K-edge, can most likely be explained by different contributions of the atomic states located on the oxygen and nitrogen atoms to the final states.[270] This can affect both the IET process and the exact course of the resonant Auger decay, in terms of the weight distribution between the different de-excitation channels.

4.2. Charge Transfer in SURMOFs

Parts of the results presented in this section were published in *Applied Materials* and *ACS Nano* and are adapted from [271] and [168].

The SURMOFs analyzed in this chapter were prepared and structurally characterized using out-of-plane X-ray diffraction (XRD), infrared reflection-absorption (IRRA), time-of-flight secondary ion mass spectrometry (ToF-SIMS) and AFM by Jianxi Liu from the group of Prof. Christof Wöll, KIT, Eggenstein-Leopoldshafen, Germany.

To help understand the charge transport in SURMOFs, also theoretical analysis of the mechanism, using a one-dimensional toy model that describes the transition from tunneling to hopping,[272] was done by our collaborators from the group of Prof. Fabian Pauly, University of Konstanz, Konstanz, Germany. In addition to gain insight into the electronic structure of HKUST-1, they performed additional DFT calculations.[273–275]

The calculations to understand the suggested charge transport mechanism of TCNQ and F4-TCNQ-loaded SURMOFs were done by the group of Prof. Wolfgang Wenzel, KIT, Eggenstein-Leopoldshafen, Germany.[276–280] For a detailed description of the the theoretical methods see the respective publication.[168,271]

The results of our partners were included in the discussion and respective data can be found in the Appendix A.

4.2.1. Pristine SURMOFs

HKUST-1 SURMOFs on CMMT with different thicknesses were used for analysis of their charge transfer properties. The different thicknesses of the LPE grown samples were obtained by applying either 5, 7 or 10 spray cycles according to the procedure reported in the literature.[113] A detailed structural analysis of the SURMOFs can be found in the Appendix A in figures A.8, A.9 and A.10. All films had the expected crystalline [111] orientation (see figure A.8 black line). The thicknesses for the pristine SURMOF films for 5, 7, and 10 spraying cycles are 45.6±6.4, 58.3±6.3, and 71.6±9.9 nm, respectively.

The tunneling junction was assembled as described in the experimental section 3.2.4 and figure 4.35, viz. a drop of Hg was passivated with HDT and gently contacted to the bottom electrode in a cell filled with HDT in HD. The stability of the HKUST-1 SURMOF under these experimental conditions was proven by out-of-plane XRD (see Appendix figure A.13). Before investigation of the SURMOF, the reliability of the setup was checked by using the CMMT SAM on Au as the bottom electrode. While sweeping the bias voltage (V) in the negative (−0.5 V to −0.01 V) and postive (0.01 V to 0.5 V) range, the current flowing through he Hg/HDT//CMMT/Au junction was measured.

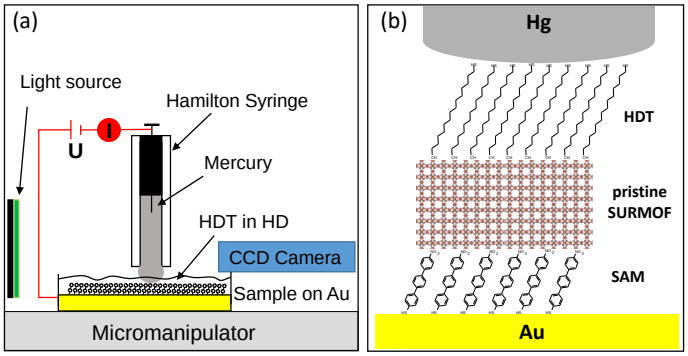

Figure 4.35.: (a) Scheme of the home-build two-terminal junction setup. (b) Magnified schematical junction for the pristine SURMOF.

Measurement of the contact diameter and calculation of the contact area, by observation of the extruded Hg drop with an magnifying camera, provided the necessary information to calculate the current density J under the applied voltage V (see figure 3.12b in the experimental part). The semilog plot of J vs V for the CMMT SAM is shown in figure 4.36. The values are in good agreement with those for SAMs of comparable thickness,[24] marked with a blue star in the figure.

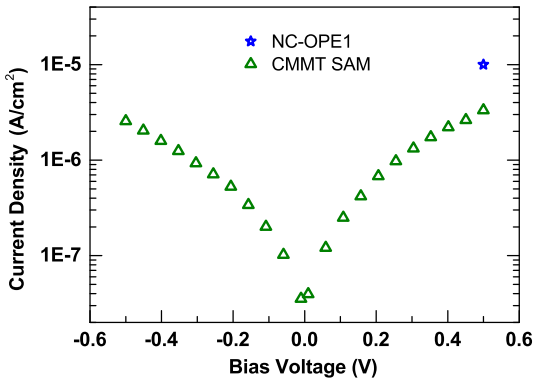

Figure 4.36.: Log J vs V plot for the CMMT SAM. The blue star represents the current density at a bias voltage of 0.5 V for a nitrile-substituted phenylthiol (NC-OPE1) SAM,[24] which has a comparable thickness to the CMMT SAM and is given for comparison.

The HKUST-1 SURMOFs were assembled in the junctions in the following way: Hg/HDT//HKUST-1/CMMT/Au. The semilog plot of the current density J vs V for the three pristine samples (5, 7 and 10 cycles) are shown in figure 4.37a. As can be clearly seen, the values of J for all the HKUST-1

SURMOF films are by far lower (by at least 2 orders of magnitude) than those of the CMMT SAM (see figure 4.36). This result confirms that the prepared SURMOF films, separating the Hg and Au electrodes by a distance of up to 70 nm, are compact, of high quality, and with no major defects that would otherwise cause short-cuts.[76] The measured low conductance reflects also the poor intrinsic conductivity of HKUST-1, in agreement with what was already reported for non-oriented films of HKUST-1 (around $1 \times 10^{-6}\,\mathrm{m\,S^{-1}}$).[281] Additionally, the prepared films appear robust, as tested by varying the pressure applied through the drop on the SURMOF. Very favorable mechanical properties of monolithic SURMOF thin films have also been reported in previous work, based on the results of indentation experiments.[282]

The used setup, with a Hg drop as top electrode gently pressed against the SURMOF, combined with the possiblity to prepare films of known and adjustable thickness, allowed to gain insight into the charge transport mechanism in MOFs by correlating the measured conductance G per area A (or the measured current density $J = G \cdot V/A$ at a fixed voltage) to the thickness of the investigated film. Analogously to what is generally done for metal-molecule-metal junctions, the slope β was extracted from the experimental data using a linear fit of the semilog plot of J at a specific voltage value vs film thickness (see figure 4.37b).[24,77–80,196] This slope is also called *tunneling decay constant* or *attenuation factor*. These terms are used in the following for reasons of compatibility with the literature, even if concluded that charge transport in the SURMOF layers is due to hopping, as discussed later.

After having checked the dependence of β on the applied voltage (see figure 4.37c) and having seen that it shows no significant variation, 0.5 V was used as specific value for V. This is in analogy to what has been reported in the literature for SAMs in Hg-based tunneling junctions.[24] Resulting from the linear fit shown in figure 4.37b, the obtained attenuation factor β corresponds to $\sim$0.006 $\mathrm{Å}^{-1}$. This value is extremely low with respect to those of SAMs[24,77–80,283,284] consisting of short, purely organic, molecular wires. However, the value is in line with values reported for "longer" organic molecular wires[284] or Hg-based tunneling junctions in which metal-organic molecular wires of a length up to 40 nm[196] were integrated. In these latter systems, low-lying energy states were provided by incorporating easily oxidizable metal centers in the organic backbone that appeared involved in a multistep charge hopping mechanism, yielding a linear increase of resistance with length (or conductance vs inverse length).[196]

As shown in the inset of figure 4.37b, the data are also compatible with such a linear, ohmic increase as expected for a charge hopping mechanism. From a linear fit $RA = R_c A + \rho L$, a high resistivity ρ of $6.8 \times 10^{12}\,\Omega\,\mathrm{m}$ was obtained. In the

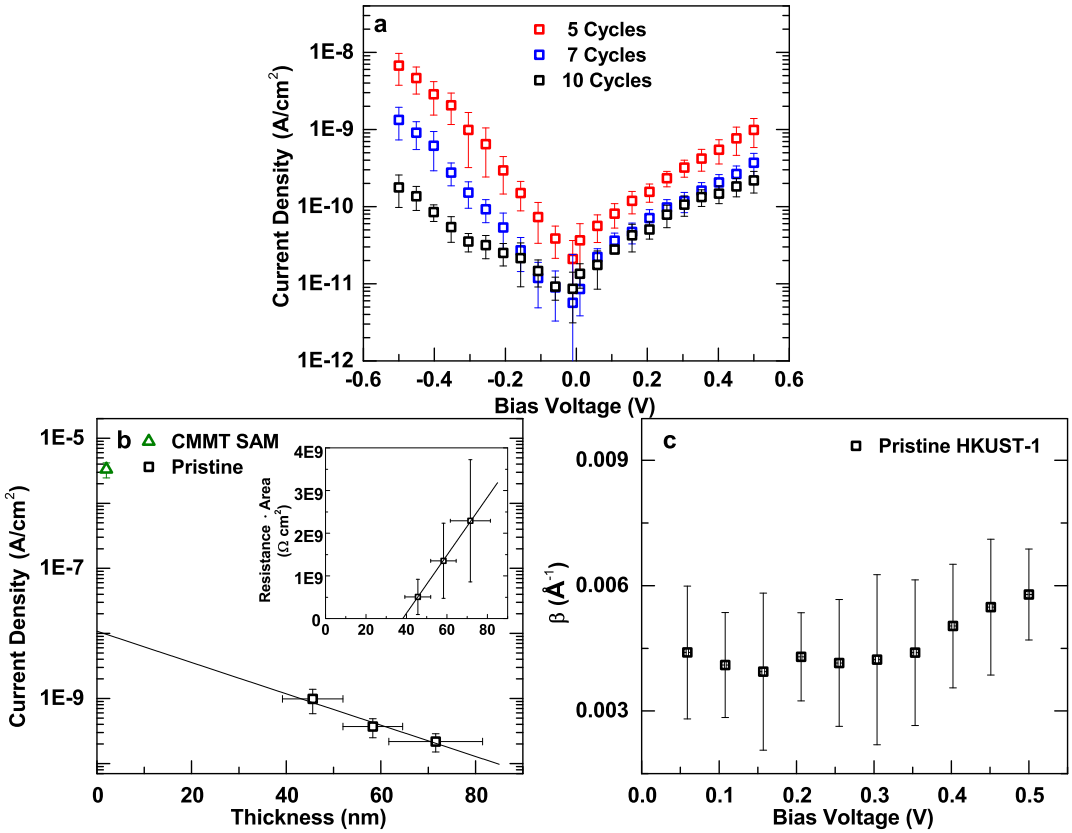

Figure 4.37.: (a) Log J vs V plot for the pristine SURMOFs after different spraying cycles. Red squares: 5 cycles, blue squares: 7 cycles and black squares: 10 cycles. (b) Logarithm of current density at 0.5 V vs thickness of pristine HKUST-1 SURMOFs (black empty squares). From the slope, the decay factor β has been calculated. A green triangle marks the current density for the CMMT SAM. The inset displays resistance times area vs thickness of pristine HKUST-1 SURMOFs (black empty squares). The data was obtained as V/J at V=0.5 V. Straight lines show linear fits, corresponding to an ohmic, linear increase in resistance with length. (c) Plot of β vs applied bias voltage in the range of 0 to 0.5 V to justify the choice of a bias voltage of 0.5 V in (b). It can be observed that β values do not vary much with applied bias voltage. Thus any value of V can be chosen for the analysis.

expression, R is the resistance of the whole Hg/HDT//HKUST-1/CMMT/Au system. It consists of the resistance of the SURMOF film $\rho L/A$ of thickness L and any other series resistance in the system that are summarized in the contact resistance R_c. This contact resistance will for instance contain contributions

from transport through the HDT and CMMT layers. Since only the thickness of the SURMOF is varied, the statements on conduction mechanism concern this layer, whereas R_c in other parts of the systems may arise from hopping, tunneling, or mixtures.

The linear, algebraic increase in resistance with film thickness (figure 4.37b) is generally not compatible with the exponential increase in resistance with thickness as expected for coherent tunneling. Attempts to fit the data with the exponential decay law $G = G_c exp(-\beta L)$ yield β values as low as $0.006\,\text{Å}^{-1}$. This corresponds to an effective tunneling barrier φ of 0.034 meV, if one uses $\beta = 2(2m_e\varphi)^{1/2}/\hbar$ with the electron mass m_e.[285] Such a vanishingly small tunneling barrier would imply good conduction due to molecular states being in resonance with the Fermi level (E_F) of the Hg/HDT//HKUST-1/CMMT/Au systems, an assumption which is not valid here. Coherent tunneling does not adequately describe the obtained data and one can conclude that the reported insulating behaviour[76,281] together with the measured high resistivity suggests an off-resonant hopping transport in the HKUST-1 films.

To understand the charge transport mechanism in the SURMOF and to explain the shallow dependence of conductance on length, a toy model that describes the transition from tunneling to hopping conduction was introduced by our partners.[272] Further details about this model can be found in the literature.[271] The SURMOF is modelled by a one-dimensional chain. The chain sites correspond to the Cu_2 centers, and the coupling of adjacent sites (only nearest neighbour couplings are considered) is via the benzene moiety of the trimesic acid linker. The model takes dephasing into account by connecting each chain site to an external, phase-randomizing reservoir. Assuming off-resonant transport, a transition from a fast, exponentially decaying conductance to an inverse ohmic length dependence, consistent with the inset of figure 4.37b, was observed. Over a certain interval of wire lengths, this latter ohmic regime can be well-approximated by an exponential law with a low β. On the basis of the results of these theoretical considerations, one can explain the low β observed from the insulating, several tens of nanometers thick SURMOF films as being due to ohmic, incoherent hopping of charge carriers.

4.2.2. Loaded SURMOFs

Porous MOFs and SURMOFs can host small molecules that can modulate and increase the conductivity of the framework.[76,281,286] In particular, the electrical transport properties of HKUST-1 films have been enhanced by inserting electro-active species and small molecules, such as iodine[286] or TCNQ[281] in the framework's pores. Such doping has led to thin films with a conductivity by far higher than those of the undoped films. Up to about 2 orders of magnitude in the case of iodine loading[286] and 6 orders of magnitude when using TCNQ s guest molecule.[281] In both cases, the increase in electrical conductivity has been explained on the basis of the interaction between the MOF (either organic linkers[286] or inorganic dimeric nodes[281]) and the guest molecules. Additionally, ferrocene molecules have been used as guests in HKUST-1 oriented thin films[76] where, as determined on the basis of cyclic voltammetry experiments, they act as redox mediators, triggering a charge hopping transport mechanism that involves the same ferrocene molecules immobilized in the pores of the framework. To get further insight into the charge transport mechanism when using suitable molecules as guest, Fc, TCNQ and F4-TCNQ were incorporated in the pores of HKUST-1 SURMOFs.

4.2.2.1. Ferrocene Loading

Loading of the HKUST-1 SURMOFs with Fc, was done as described in the literature[76] and the experimental section 3.1.3.1. The structural analysis and successful loading of the SURMOFs was confirmed by IRRA and out-of plane XRD. The according data by Jianxi Liu can be found in the Appendix A in figures A.8, A.9 and A.10 along with the analysis of the pristine samples.

The current flowing through the Hg/HDT//HKUST-1/CMMT/Au junction, assembled as described in figure 4.38, with the Fc-loaded SURMOFs, was measured for the same samples (5, 7, and 10 spraying cycles with the respective thicknesses of 46.2±5.7, 58.6±7.0, and 72.2±4.0 nm after loading) as in the case of the pristine HKUST-1 SURMOFs. As shown in figure 4.39a-c, the J values are always larger for the Fc-loaded HKUST-1 SURMOFs than for the corresponding pristine samples. The increase for the thinnest sample is slightly larger (5.4 times; figure 4.39a) than for the thickest one (2.8 times; figure 4.39c). This is in line with the theoretical model.[271] The slightly larger β value for the Fc-loaded samples, related to a faster decay of the conductance in these samples than in the pristine SURMOFs, leads to a decrease in the conductance ratio with an increase in the MOF film thickness. The measured better conductivity after the ferocene loading suggests that the ferrocene has an effect on the electronic properties of HKUST-1. However, when plotting logJ vs film

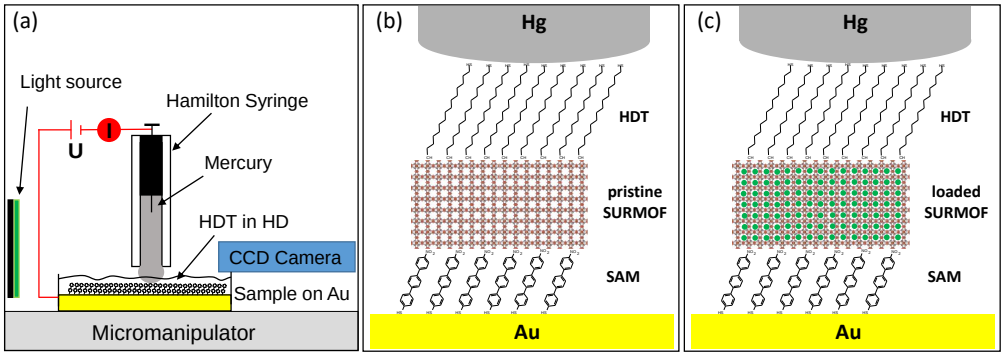

Figure 4.38.: (a) Scheme of the home-build two-terminal junction setup. (b) Magnified schematical junction for the pristine SURMOF and (c) the loaded SURMOF.

thickness (figure 4.39d), a similar dependence of the current density values on the thickness as for the pristine SURMOF samples was found. The β value appeared, within the error bars, barely modified. Nevertheless, its slight increase ($0.008\,\text{Å}^{-1}$) is in agreement with the theoretical model, where an increase towards the Fc-loaded case is proposed. As shown in the inset of figure 4.39d, the data for the Fc-loaded SURMOFs is again compatible with a linear increase of resistance with the film thickness, but the resistivity ρ of $2.8 \times 10^{12}\,\Omega\,\text{m}$ is lowered by a factor of around 2.5. The results support the charge hopping regime as leading conduction mechanism also for the Fc-loaded HKUST-1 SURMOFs.

To further explore the changes upon Fc loading, DFT calculations were performed by our partners. The Fc likes to bind to the benzene-based linkers through $\pi - \pi$ stacking interactions and, in terms of the electronic structure, leads to occupied states within the band gap of the MOF. There were no strongly delocalized electronic states around the band gap. The MOF states are only slightly modified du to hybridization, and molecular orbitals are either located on the ferrocene or on the MOF skeleton. For this reason no change of the charge transport mechanism is expected, as compared to the pristine framework. Although the DFT calculations cannot completely exclude that Fc molecules serve as additional hopping sites in charge transport, the reduction of resistance R and resistivity ρ for the Fc-loaded case was rather attributed to a better electronic coupling of the Cu_2 metal sites, possibly combined with an enhanced dephasing at these nodes. The major factors leading to the low intrinsic conductivity of HKUST-1 are the insulating behaviour of the organic linkers and the bad electronic coupling of Cu_2 metallic nodes, related to the meta configuration of the benzene-derived bridges. Upon loading with Fc, the

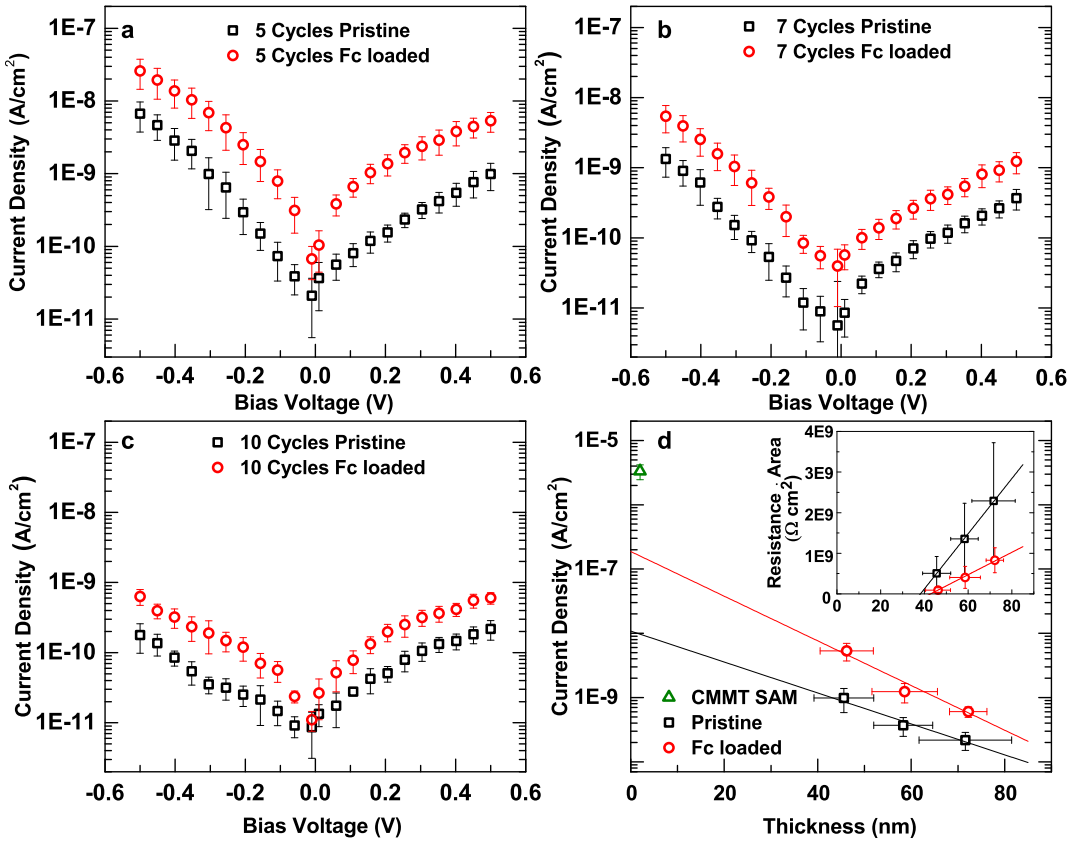

Figure 4.39.: (a) Log J vs V plot for the Fc loaded (red squares) and pristine (black squares) SURMOF after 5 spraying cycles. (b) Log J vs V plot for the Fc loaded (red squares) and pristine (black squares) SURMOF after 7 spraying cycles. (c) Log J vs V plot for the Fc loaded (red squares) and pristine (black squares) SURMOF after 10 spraying cycles. (d) Logarithm of current density at 0.5 V vs thickness of HKUST-1 SURMOFs, pristine (black empty squares) and after ferrocene loading (red empty circles). From the slope, the decay factor β has been calculated. A green triangle marks the current density for the CMMT SAM. The inset displays resistance times area vs thickness of HKUST-1 SURMOFs, pristine (empty black squares) and after ferrocene loading (empty red circles). The data is obtained as V/J at V=0.5 V. Straight lines show linear fits, corresponding to an ohmic, linear increase in resistance with length.

electronic and vibrational structures as well as the electron-vibrational couplings will be modified, as evident from the observed changes in the crystal structure (figure A.8 in the Appendix). The enhanced effective electronic coupling and dephasing strength between and at the Cu_2 centers, leading to the

improved transport properties, may stem from a partial lifting of the destructive electron interface that suppresses conduction for meta couplings.[287–289] An enhanced electron-vibration scattering due to the fluctuating interactions of the Fc molecules on top of the trimesic acid bridges at finite temperature can induce decoherence that reduces destructive interference, in addition to a purely electronic mechanism that changes left- and right-going electron paths on the benzene linker. In addition, a charge rearrangement at the interfaces due to the Fc-related states may modify the charge injection barrier.

4.2.2.2. TCNQ & F4-TCNQ Loading

Loading of the HKUST-1 SURMOFs with TCNQ and F4-TCNQ, was done as described in the experimental section 3.1.3.1. The successful loading of the SURMOFs was confirmed with IRRA and out-of plane XRD. The according data can be found in the Appendix A in figures A.11a-d along with the analysis of the pristine samples. The efficiency of loading was probed with ToF-SIMS and the thickness of the TCNQ-loaded samples was evaluated with AFM (see figure A.12 in the Appendix) and showed 33.3±3.0, 53.2±4.1, and 62.3±7.3 nm for the 5, 7, and 10 spraying cycles, respectively. The values are slightly lower than for the pristine and Fc-loaded SURMOF films discussed before, which is related to a new series of SURMOF samples, prepared for these measurements. The above investigations were done by Jianxi Liu prior to my measurements.

The current flowing through the HKUST-1 films, loaded with TCNQ and F4-TCNQ, integrated in the junction Hg/HDT//HKUST-1/CMMT/Au was measured in the same fashion as for the previously presented pristine and Fc-loaded samples. The results of the conductivity experiments are compiled in figure 4.40. Panel a-c display semilog plots of the current density vs voltage for the pristine (unloaded) HKUST-1 SURMOFs prepared by 5, 7 and 10 spraying cycles. Whereas the currents are very low for the pristine HKUST-1, as expected from the large highest occupied molecular orbital (HOMO)-LUMO gap and consistent with data in the previous section, upon loading with TCNQ (blue triangles) and F4-TCNQ (green squares), the current density increases by 4-5 orders of magnitude for the both guest molecules. The earlier findings of Allendorf and co-workers[281] for TCNQ were reproduced, but verified for much better defined samples in a more reliable experimental setup. In contrast, the results for F4-TCNQ are distinctly different from the previous findings:[281] the current density increases strongly and comparably to the TCNQ case. Based on the above experimental data, a superexchange mechanism for charge transfer was proposed by our partners, where carriers hop from guest to guest mediated by virtual occupancy of a host site, for both TCNQ and F4-TCNQ-loaded SURMOFs (see figure 4.41).[168] In order to compare the experimental results

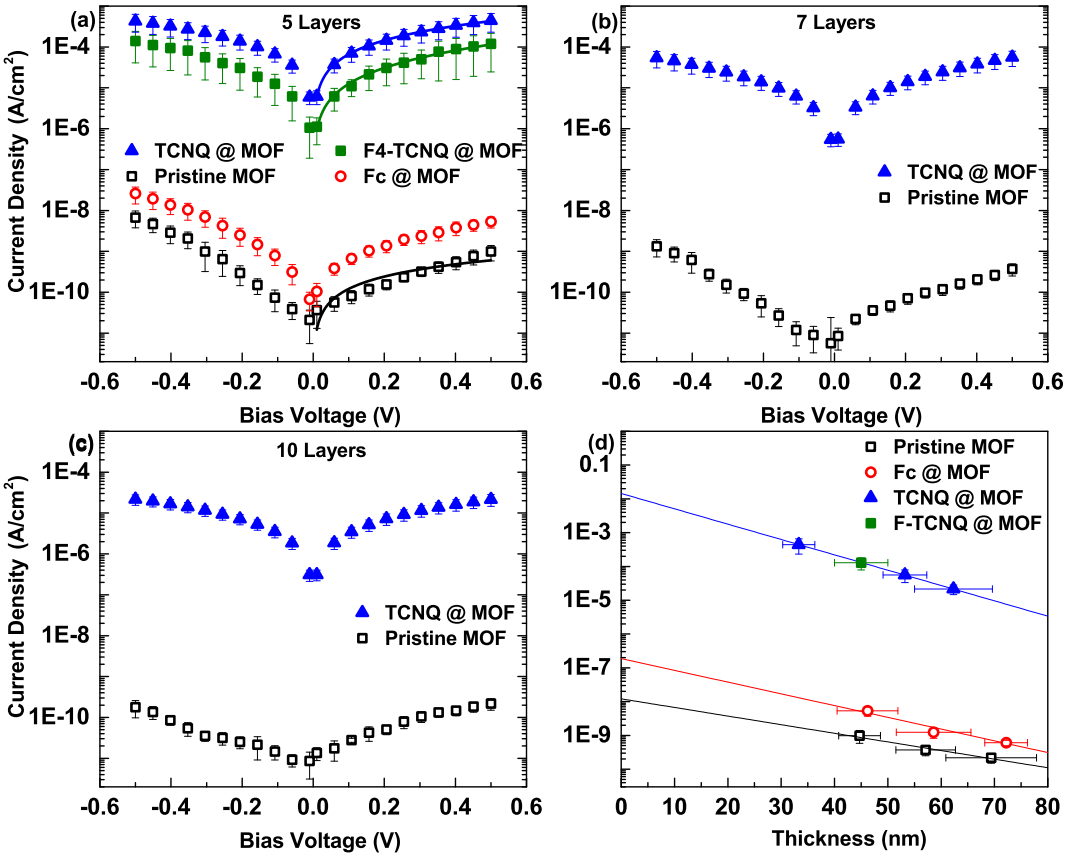

Figure 4.40.: (a) Log J vs V plot for the TCNQ (blue triangles), F4-TCNQ-loaded (green squares) and pristine (black squares) SURMOF after 5 spraying cycles. The theoretical model was fitted to the experimental data (respective colour-coded line). The curve for the 5 cycles Fc-loaded SURMOF was added for comparison (red cicles) (b) Log J vs V plot for the TCNQ-loaded (blue triangles) and pristine (black squares) SURMOF after 7 spraying cycles. (c) Log J vs V plot for the TCNQ-loaded (blue triangles) and pristine (black squares) SURMOF after 10 spraying cycles. (d) Logarithm of current density at 0.5 V vs thickness of HKUST-1 SURMOFs, pristine (black squares) and after TCNQ (blue triangles), F4-TCNQ (green square) and Fc-loading (red circles for comparison); straight lines show linear fits. From the slope of the linear fits, the decay factor β has been calculated.

with the simulated results of our partners, an injection model was used.[290] The resulting theoretical curves (solid lines in figure 4.40a) are in good agreement to the experimental data. See literature[168] for more details about the calculations.

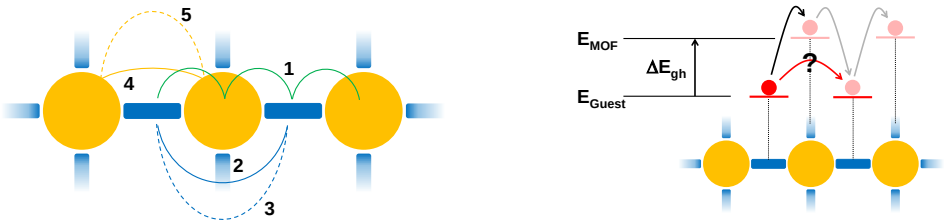

(a) (b)

Figure 4.41.: Extension to figure 2.10. (a) Possible first-order transfer processes are subsequent hopping between guest and MOF sites (1) and the direct transfer between guest-guest or MOF-MOF sites (2,4). Processes (1) an (2) are suppressed by large ΔE and low J, respectively, and the rate of process (4) is limited because MOF states are not occupied. In order to explain high current densities in the MOF-guest system, additional second order processes (superexchange, dashed lines) have to be considered (3,5). (b) Transfer between the LUMO orbitals of the guest molecules can proceed directly or via occupancy of a virtual stat in the MOF. In the superexchange process, the energy difference, ΔE_{gh}, enters linearly in the rate, while it enters exponentially in guest-host hoping processes. Mechanism proposed by the group of Prof. Wolfgang Wenzel, KIT, Eggenstein-Leopoldshafen, Germany, based on the experimental data. From [168].

A semilog plot of the current density J at a bias voltage V=0.5 V as a function of the SURMOF thickness is presented in figure 4.40d. As described in a previous sections of this chapter, for the pristine HKUST-1 SURMOFs, the decrease of current with thickness (or the increase of resistivity) is consistent with quasi-ohmic behaviour, typical of metallo-organic systems.[271,291,292] The values for β, which are only obtained for comparison with the literature, even though it was concluded that the charge transport in the pristine and TCNQ loaded HKUST-1 SURMOFs follow the hopping mechanism, with a specific superexchange scenario in the case of the TCNQ, are 0.006 $Å^{-1}$ for the pristine SURMOF film (see previous sections) and 0.0105 $Å^{-1}$ for the TCNQ-loaded sample. The value is still very low and it is difficult to say at the moment whether the observed increase in the β value is meaningful. Most significantly, the current density values for the TCNQ-loaded SURMOFs are consistently higher than those for the pristine HKUST-1 by 5-6 orders of magnitude.

The obtained resistivity for the pristine SURMOF is about $7.1 \times 10^{12}\,\Omega\,m$ (figure 4.42a), while the resistivity of the TCNQ-loaded one is $5.2 \times 10^{7}\,\Omega\,m$ (figure 4.42b). Thus, the resistivity of HKUST-1 loaded with TCNQ is at least

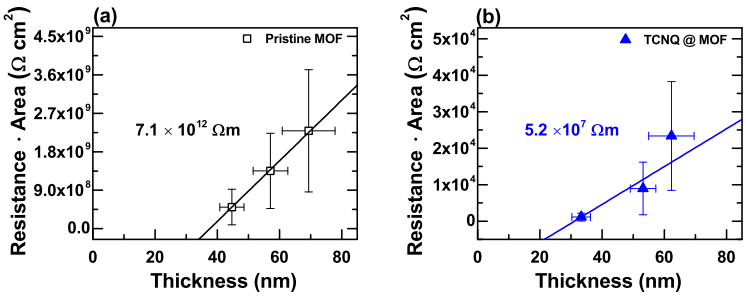

Figure 4.42.: Plot of the resistance times area ($R \cdot A$) vs thickness (L) of pristine (a) and TCNQ-loaded (b) SURMOFs at V=0.5 V. Straight lines show linear fits according to $R \cdot A = R_c \cdot A + \rho \cdot L$, from which the resistivity ρ can be extracted.

5 orders lower than that for the pristine MOF. The same result was observed for the F4-TCNQ, with the data point fitting almost exactly to those for the TCNQ loading. As mentioned above, this result agrees with the superexchange model,[168] but is in dissonance with the earlier findings by Allendorf and coworkers.[281] The reason for this discrepancy are presently unknown and probably related to specific parameters of both experiments. Any possible artifacts in this work was carefully excluded by thorough characterization of the empty and loaded films and by the selection of a specific experimental setup for the electrical transport measurements.

The increased conductivity upon loading the SURMOF with TCNQ and F4-TCNQ is resulting from the position of the LUMO levels, which are substantially closer to the Fermi energy of the electrode (and thereby diminishing the injection barrier) than it is the case in the pristine SURMOF. The LUMO energy of the latter, which is mainly localized on the copper atoms of the paddlewheel unit,[281] exceeds the work functions of commonly used electrodes, such as Pt or Al (which are well over 4.0 eV[281,293]).

4.2.2.3. Effect of the SAM Template

An additional variation of the HKUST-1 systems was the exchange of the so far used CMMT molecule with the 16-mercaptohexadecanoic acid (MHDA) molecule to form the SAM template for the SURMOF. The structure of the molecules are drawn in figure 4.44 on the left and right side. This variation of the SAM template resulted in a different orientation of the SURMOFs, which was confirmed by our partners via XRD.

The resulting J vs V curves of the pristine and TCNQ-loaded SURMOFs using MHDA as a template are exhibited in figure 4.43a for a thickness of 5

spraying cycles and 4.43b for a thickness of 10 spraying cycles. The electrical transport properties for these samples are the same as observed for the SURMOF orientation with CMMT template. After loading with the TCNQ, the current density increased by several orders of magnitude. Clearly visible for the 5 spraying cycles in figure 4.43a. For the 10 spraying cycles, it is assumed that the *real* conductivity of the pristine SURMOF is below the plotted values, which were recorded at the limit of the Keitley Sourcemeter.

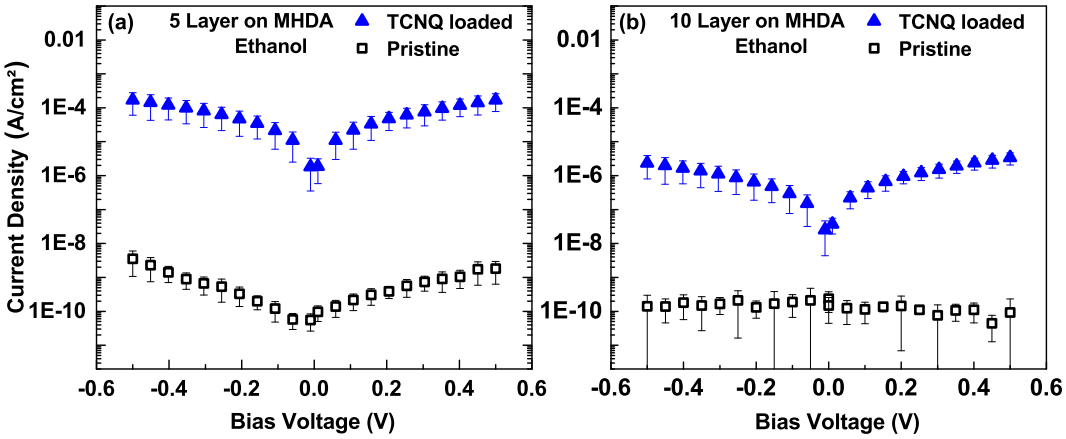

Figure 4.43.: (a) Log J vs V plot for the TCNQ (blue triangles) and pristine (black squares) SURMOF on MHDA template after 5 spraying cycles. (b) Log J vs V plot for the TCNQ-loaded (blue triangles) and pristine (black squares) SURMOF on MHDA template after 10 spraying cycles. In the case of 10 spraying cycles, the pristine SURMOF was outside the measuring range of the used Keithley Sourcemeter

To compare the pristine SAMs with each other, the log J vs V curves of the respective templates on Au(111) are shown in figure 4.44. For these measurements a two-terminal junction with EGaIn instead of mercury as a top electrode was used. The formation of the tip and the junction was described in the experimental section 3.2.4. The stability of the EGaIn junction was higher on these particular molecules as compared to the mercury drop.

The observed current density values drop down by about 1.5 orders of magnitude for MHDA as compared to CMMT, which is according to the film thickness of respecitve films. A numerical evaluation of the effective film thickness was derived from the ratio of the C 1s to Au 4f region, obtained by laboratory XPS analysis following the standard procedure described in the experimental part in section 3.2.1.2 and the literature.[199] The derived values are are 17.8±0.1 Å and 13.9±0.1 Å for MHDA and CMMT, respectively. This presumably explained the values measured for the pristine SURMOF on MHDA after 10 spraying

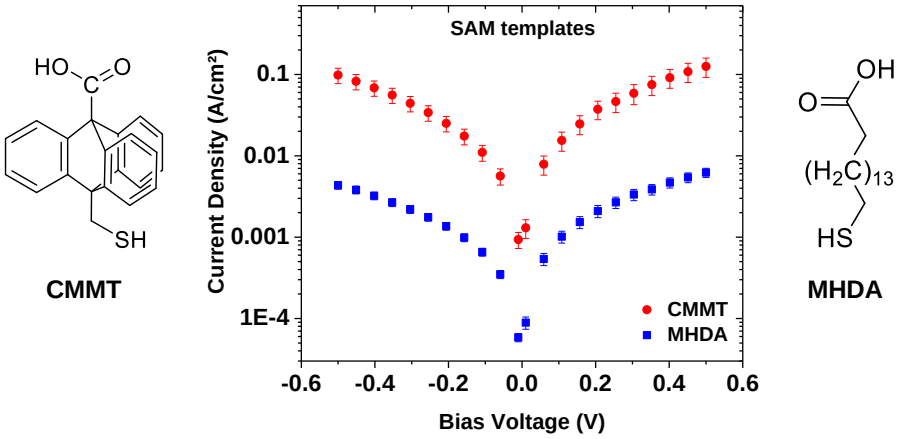

Figure 4.44.: Log J vs V curves of the pure MHDA and CMMT SAMs on Au(111) along with their respective molecular structures. The SAMs of these molecules were used as templates for the SURMOF formation. Measured with the modified setup, using EGaIn instead of mercury.

cycles in figure 4.43b. For pristine SURMOF samples on CMMT it was confirmed that a thickness of 10 spraying cycles is just in the measurable range. Several measurements of pristine SURMOF with a higher thickness (more than 10 spraying cycles) were not measurable, as the limit of the Keithley sourcemeter was reached. For pristine SURMOFs on MHDA this limit was presumably already reached for 10 or less spraying cycles (see figure 4.43b).

4.2.2.4. Effect of the Solvent

As described in the experimental section (section 3.1.3), the loading of TCNQ and F4-TCNQ was performed from their solutions in ethanol. As an alternative, loading from dichlormethane (DCM) solutions was performed, keeping most of the other parameters, including the temperature, unchanged. Although in some cases the loading of the SURMOFs was non-complete and inhomogeneous (shown by ToF-SIMS), the electrical transport properties of the homogeneously loaded samples were observed to be comparable to the samples loaded from ethanol.

5. Conclusions

In this work, I focused on two different nanoscale systems, studying their charge transfer properties.

First, dynamic ET properties of SAMs were studied by RAES in combination with a dedicated CHC approach. A variety of custom molecular assembles were designed and fabricated to address specific questions within the general framework of ET dynamics.

Second, static CT properties of novel SURMOFs with well-defined thickness, quality and orientation were studied by integration of pristine and guest loaded samples into a two-terminal junction setup. The derived current densities and static parameters served as a basis for the understanding of underlying transport mechanisms.

The following specific questions were addressed within the SAM sub-project: (i) the effect of molecular anchor; (ii) ET properties of acene backbone; (iii) ET properties of a non-benzenoid aromatic molecule; (iv) the ultimate proof of ET by direct attachment of nitrile to the substrate and (v) the suitability of alternative tail groups for site-specific resonant excitation.

To fulfil the requirements for the above studies, all SAM samples were extensively studied by advanced X-ray spectroscopy to prove their quality and to obtain detailed information of their structure and organization. All molecules in the SAMs were found to bind to the substrate via the thiolate/selenolate anchor, have an upright orientation and, thus, form well-defined SAMs.

(i) To understand the impact of the anchor substitution on structure, stability and ET properties of SAMs, two representative model systems, NC-NapS/Au(111) and NC-NapSe/Au(111), were investigated. Their similar structural characteristics allowed a rational study of ET properties of thiolate and selenolate SAMs on noble metal substrates. I found identical ET times of 24 ± 4 fs for both systems, which suggests similar electronic coupling efficiency of the Au−S−C and Au−Se−C linker, solving a long-time controversy.

Further, the S→Se substitution was found to be of importance for the molecular organization and structural perfection in the given SAMs. At least in the case of the aromatic SAMs, the Se−Au bond allows for a better structural perfection as compared to the thiolate anchor, resulting in monolayers of a higher quality.

(ii) In addition to the NC-NapS/Se systems, I also analyzed the respective anthracene-based films, NC-AntS/Au(111) and NC-AntSe/Au(111). Their structural similarity and the results of the dynamic ET experiments are in line with the previous observations for NC-NapS/Se on gold. An average τ_{ET} of ∼41±6.5 fs was found for both NC-AntS and NC-AntSe, which confirms that the S→Se exchange does not affect the electronic coupling to the substrate. At the same time, an interesting finding was the dependence of τ_{ET} on the length of the acene backbone with $\beta \approx 0.25\,\text{Å}^{-1}$, being comparable to oligophenyls ($\beta = 0.29\,\text{Å}^{-1}$)[38] and in the range of values derived from static measurements of acenes found in the literature: $\beta = 0.45\,\text{Å}^{-1}$[22] to $0.5\,\text{Å}^{-1}$[53] for monothiols and $0.2\,\text{Å}^{-1}$ for dithiols.[53]

(iii) Additionally a non-benzenoid isomer of naphthalene, azulene was introduced as a molecular backbone. The effective film thickness and molecular orientation of NC-AzuS/Au(111) was found to be similar to NC-NapS/Au(111). The subsequent RAES-CHC investigation delivered τ_{ET}=23±4 fs, which is nearly identical to the NC-NapS film (24±4 fs), showing no noticeable influence of the non-benzenoidic character on the dynamic ET properties.

(iv) For the ultimate proof of ET, the −C≡N moiety was directly attached to Au(111). The cyanide molecules were bound to the gold trough the carbon atom and oriented upright. The time for ET to the gold was found to be below 1 fs, suggesting an almost immediate ET and verifying our approach.

(v) With the design of 4-pyridyl- and nitro-substituted (oligo)phenylthiols, I studied alternative groups to nitrile for site-specific resonant excitation.

Films of PyrP0S/Au(111) and PyrP1S/Au(111) were found to be similar to the respective phenylthiol analogs. Analysis of the [N 1s]π^* RAE spectra of both SAMs suggested a considerable contribution of ET, indicating the suitability of the pyridyl moiety as an alternative to nitrile. Subsequent CHC calculations derived τ_{ET} of 15±3 fs for PyrP0S and 43±7 fs for PyrP1S. Interestingly, these values are inbetween τ_{ET} for [N 1s]π_1^* and [N 1s]π_3^* excitation of the respective nitrile-substituted analogs, with ET via the π_1 orbital being much more efficient due to conjugation with the adjacent phenyl ring. This comparison let assume a slight conjugation between the pyridyl and phenyl rings of the analyzed SAMs.

Further, nitro-(oligo)phenylthiol films were found to be well-defined and similar to those of the analogous nonsubstituted systems. The [N 1s]π^* and [O 1s]π^* decay spectra of all studied nPT−NO_2 SAMs did not exhibit any trace of ET from the excited tail group to the substrate through the molecular framework. At the same time a reverse process, viz., the neutralization of the core ionized state by ET from the substrate/molecular backbone, became in principle possible and could be traced in the given case as an admixture of the resonant contributions into the non-resonant decay spectra at the O K-edge. A simi-

lar extent of these contributions for all studied SAMs suggests that only the phenyl ring adjacent to the nitro group was involved in the inverse electron transfer (IET) process.

The second focal point of my studies was to explore the CT properties of SURMOFs. Samples of high quality, represented by oriented HKUST-1 SURMOF films with low defect density of different thicknesses were fabricated, characterized in detail and incorporated into two-terminal junctions. Transport properties of the basic SURMOFs were found to be analogous to those of hybrid metal-organic molecular wires, manifested by a very low value of the tunneling decay constant ($\beta \approx 0.006\,\text{Å}^{-1}$). This suggested a similar mechanism of conduction, which was elaborated by our partners on the basis of the experimental data.

After incorporation of ferrocene into the pores of HKUST-1 SURMOFs, a noticeable increase in transport current up to 5 times was observed, indicating a reduction in the charge injection barrier and and improved electronic coupling between metal nodes. On the basis of these experimental results, a suitable transport model was developed, revealing a hopping CT mechanism.

Loading the SURMOF with TCNQ and F4-TCNQ resulted in a tremendous increase of current density by 5-6 orders of magnitude higher as compared to the pristine framework for both guest molecules. The earlier findings in the literature[81] were, thus, reproduced for TCNQ, but verified for much better defined samples in a more reliable experimental setup. The F4-TCNQ findings were new and different from the previous results,[81] showing also a strong increase in current density. Based on the above experimental data, a novel superexchange mechanism for CT in the redox-molecule-loaded SURMOFs was proposed, where carriers hop from guest to guest mediated by virtual occupancy of a host site.

The same tremendous increase in current density was observed for TCNQ-loaded SURMOFs with a differently oriented framework and after variation of the loading-solvent.

Both investigated systems show new results for SAMs and SURMOFs, important for possible applications in nanoscale electronics. Further experiments in the framework of ET dynamics of SAMs can be performed with a focus on partly or fully substituted backbones and, thus, influences of inductive effects on the defined ET pathway. In addition, the possibility to assemble SURMOF films in two-terminal junctions provides a reliable basis for further investigations of numerous guest molecules and alternative SURMOF-systems.

A. Supplementary Data by our Partners

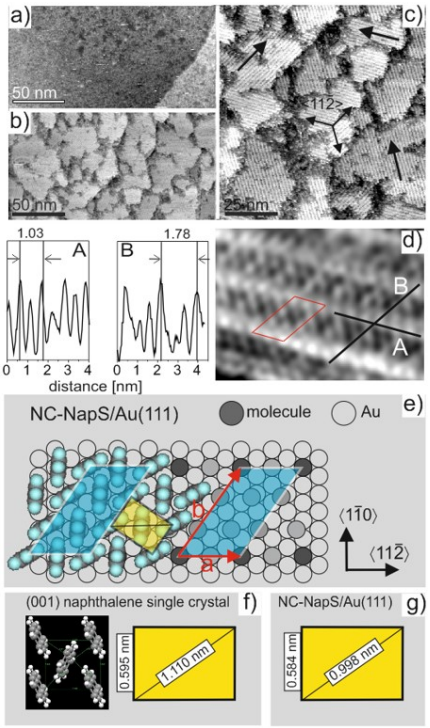

Figure A.1.: STM images taken with different resolutions for the NC-NapS SAMs on Au(111) prepared at room temperature (a) and at 60° (b-d). Height profiles A and B are taken along the lines depicted in (d). The red box in (d) marks the oblique $(2\sqrt{3} \times \sqrt{37})$ unit cell schematically presented in (e). In (f), the 2D herringbone arrangement of the naphthalene molecules within the (001) plane of the naphthalene single crystal is shown, along with the respective rectangular unit cell (in yellow). A similar structural motif can be found in the STM images of the NC-NapS SAMs, as shown by the yellow rectangle in (e). The dimensions of this motif, as determined by STM, are presented in (g) for direct comparison with (f). Data contributed by the group of Prof. Peter Feulner, Physikdepartment E20, Technische Universität München, 85747 Garching, Germany. Reprinted with permission from [188]. Copyright 2015 American Chemical Society.

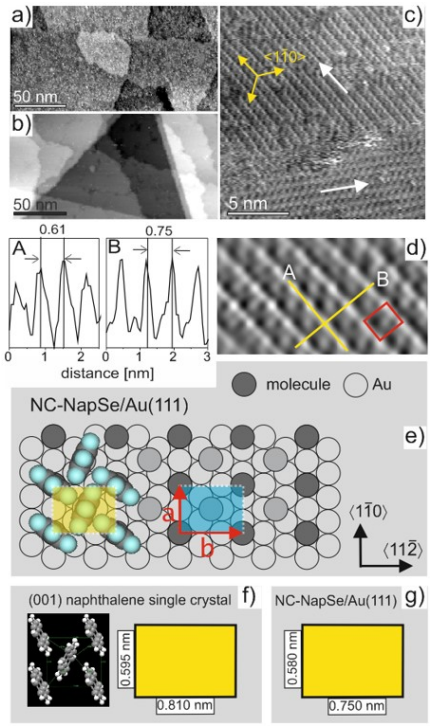

Figure A.2.: STM images taken with different resolutions for the NC-NapSe SAMs on Au(111) prepared at room temperature (a) and at 60° (b-d). Height profiles A and B are taken along the lines depicted in (d). The red box in (d) marks the rectangular $(2 \times 1.5\sqrt{3})$ unit cell schematically presented in (e). In (f), the 2D herringbone arrangement of the naphthalene molecules within the (001) plane of the naphthalene single crystal is shown, along with the respective rectangular unit cell (in yellow). A similar structural motif can be found in the STM images of the NC-NapSe SAMs, as shown by the yellow rectangle in (e). The dimensions of this motif, as determined by STM, are presented in (g) for direct comparison with (f). Data contributed by the group of Prof. Peter Feulner, Physikdepartment E20, Technische Universität München, 85747 Garching, Germany. Reprinted with permission from [188]. Copyright 2015 American Chemical Society.

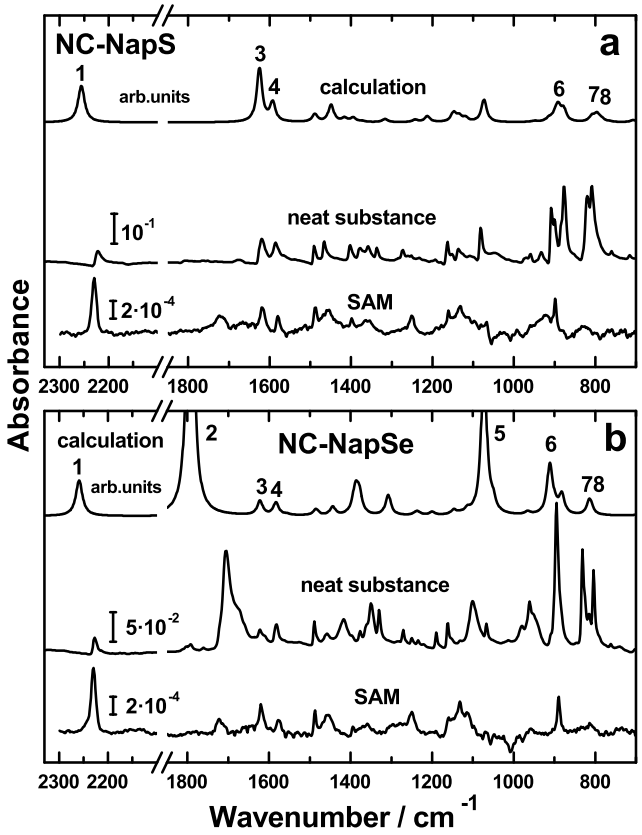

Figure A.3.: IR spectra for NC-NapSH/NC-NapS (a) and NC-NapSeAc/NC-NapSe (b). The upper traces represent calculated spectra of the isolated molecules using DFT; the middle traces show the spectra of the neat substances (NC-NapSH and NC-NapSeAc); in the lower traces, the IRRA spectra of the NC-NapS and NC-NApSe SAMs on Au are displayed. The theoretical spectra are scaled in arbitrary units; the scale bars for the absorbance of the experimental spectra are given in the figure. The most important vibrational bands are designated with numbers. According to the surface selection rule,[294] a more upright orientation can be assumed for NC-NapS and NC-NapSe molecules due to the fact that bands with out-of-plane TDMs (**7** and **8**) are clearly attenuated in comparison to bands with TDMs parallel to the C≡N bond axis (**1**, **3**, **4**, **6**). Data contributed by the group of Prof. Andreas Terfort, Institut für Anorganische und Analytische Chemie, Universität Frankfurt, Max-von-Laue-Straße 7, 680438 Frankfurt, Germany. Reprinted with permission from [188]. Copyright 2015 American Chemical Society.

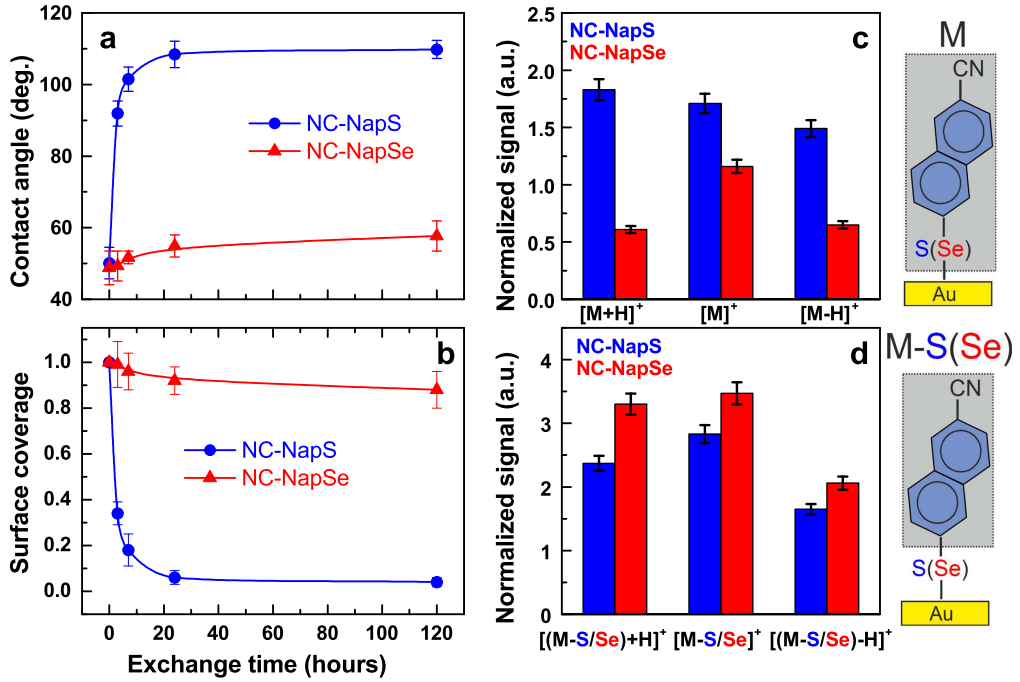

Figure A.4.: WCA (a) and relative surface coverage of the NC-NapS(Se) molecules (b) derived in the course of exchange reaction between the NC-NapS (blue) or NC-NapSe (red) SAMs on Au(111) and HDT molecules in solution. The lines are guides for the eyes. (c) and (d) S-SIMS data analysis: (c) normalized signal of the $[M+H]^+$, $[M]^+$ and $[M-H]^+$ secondary ions related to the desorption of the complete molecules for NC-NapS/Au(111) (blue bars) and NC-NapSe/Au(111) (red bars) SAMs. (b) analogous data for the secondary ions related to the desorption of desulfurized fragments from NC-NapS/Au(111), viz. $[(M-S)+H]^+$, $[M-S]^+$ and $[(M-S)-H]^+$ (red bars) as well as deselenied fragments from NC-NapSe/Au(111), viz. $[(M-Se)+H]^+$, $[M-Se]^+$ and $[(M-Se)-H]^+$ (blue bars). Data contributed by the group of Prof. Piotr Cyganik, Smoluchowski Institute of Physics, Jagiellonian University, Reymonta 4, 30-059 Krakow, Poland. Reprinted with permission from [188]. Copyright 2015 American Chemical Society.

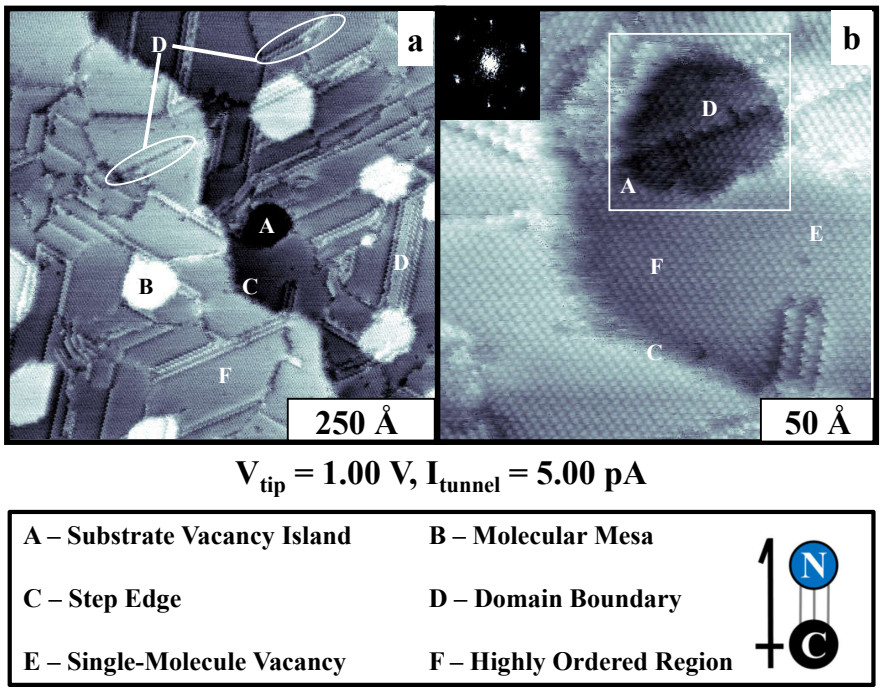

Figure A.5.: STM images of the surface structure of cyanide monolayers on Au(111) at RT. (a) The morphology of the cyanide monolayers with representative surface structures denoted by letters A-F in the image and schematic of cyanide with aligned dipole C→N, Positive→Negative. (b) Molecular resolution images and corresponding Fourier transform showing the hexagonally close-packed lattice with nearest neighbor distance of 3.8±0.5 Å. Data contributed by the group of Prof. Paul Weiss, Department of Chemistry and Biochemistry, University of California, Los Angeles, California 90095, United States. Reprinted with permission from [229]. Copyright 2016 American Chemical Society.

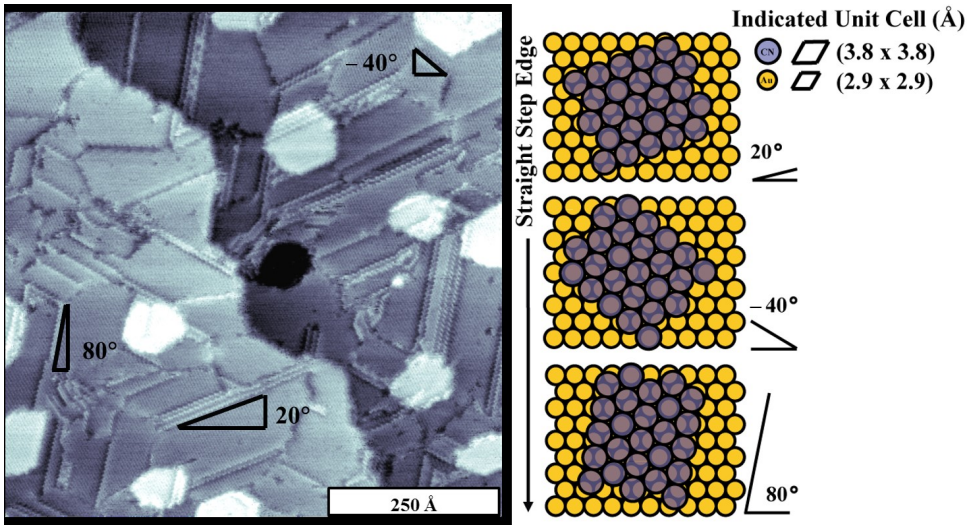

Figure A.6.: STM images of CN on Au(111) as deposited at room temperature and structural schematics. Using the Au close-packed substrate direction with respect to straight step edges (<0 1 0>), we find molecules bind to bridge and atop positions with a (3.8 Å×3.8 Å) cyanide unit cell at 20°, -40°, and 80° orientations with respect to the unreconstructed underlying gold lattice. The dark, larger circles represent the projection of the cyanide molecules on the smaller circles representing the atoms of the Au(111) lattice. Triangles representing examples of the identified orientations relative to the Au(111) lattice are aligned with cyanide domain boundaries and are identified as high-symmetry directions representative of the hexagonal close-packed arrangement. Data contributed by the group of Prof. Paul Weiss, Department of Chemistry and Biochemistry, University of California, Los Angeles, California 90095, United States. Reprinted with permission from [229]. Copyright 2016 American Chemical Society.

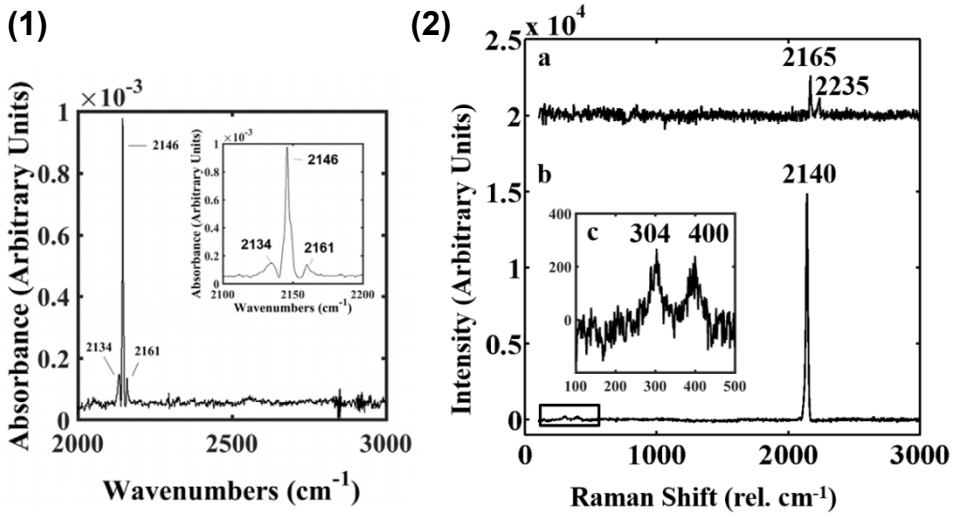

Figure A.7.: (1) The attenuated total reflection Fourier transform infrared spectrum of CN/Au(111) using custom sapphire prism substrates and showing the CN sretch at 2146 cm^{-1} along with two side peaks at 2134 cm^{-1} and 2161 cm^{-1}. The inset is an enlargement of the region of the spectrum containing the CN vibration. (2) (a) Raman spectra of CN monolayers formed on Au(111) using a plasmonic nanohole array and (b) surface-enhanced Raman substrates made of polycrystalline Au nanoparticles evaporated onto glass. (c) The inset shows both the low freuqency modes attributed to the substrate-molecule bond, Au-CN bend at 304 cm^{-1} and Au-CN stretch at 400 cm^{-1}, which were only detected on the Au nanoparticles. Data contributed by the group of Prof. Paul Weiss, Department of Chemistry and Biochemistry, University of California, Los Angeles, California 90095, United States. Reprinted with permission from [229]. Copyright 2016 American Chemical Society.

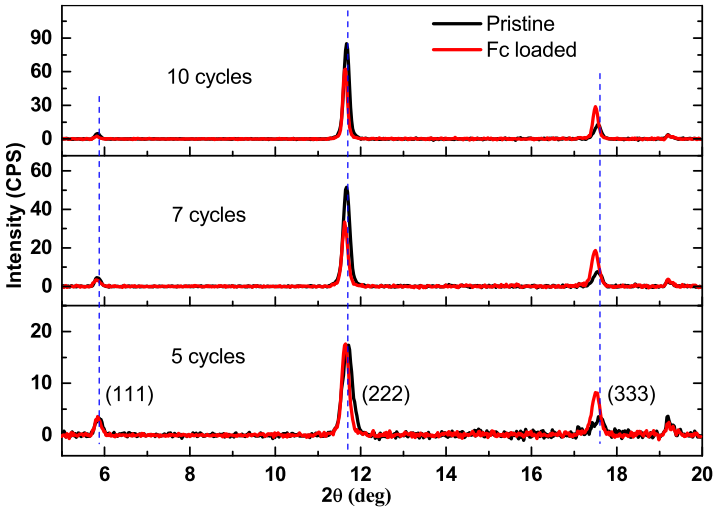

Figure A.8.: (a) Out-of-plane XRD of the pristine (black) and the ferrocene-loaded (red) HKUST-1 SURMOF samples. From top to bottom: 10, 7 and 5 spraying cycles. Data contributed by Jianxi Liu, group of Prof. Christof Wöll, Institute of Functional Interfaces (IFG), Kalsruhe Institute of Technology (KIT), 76344 Eggenstein-Leopoldshafen, Germany. Reprinted with permission from [271]. Copyright 2015 American Chemical Society.

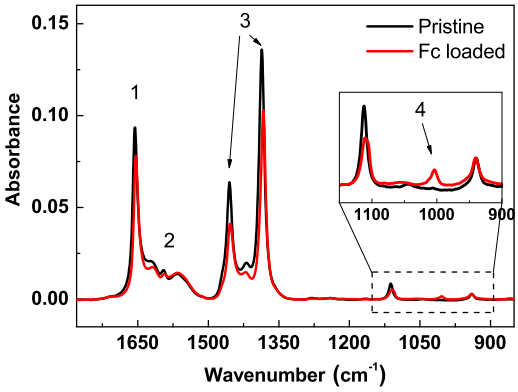

Figure A.9.: IRRA spectra of HKUST-1 SURMOFs before (black) and after (red) loading with ferrocene. Feature 1 stems from COO_{asym}, 2 from benzene ring, 3 from COO_{sym} and 4 from aromatic C−H stretching coming from the ferocene ring, present only after loading. Data contributed by Jianxi Liu, group of Prof. Christof Wöll, Institute of Functional Interfaces (IFG), Kalsruhe Institute of Technology (KIT), 76344 Eggenstein-Leopoldshafen, Germany. Reprinted with permission from [271]. Copyright 2015 American Chemical Society.

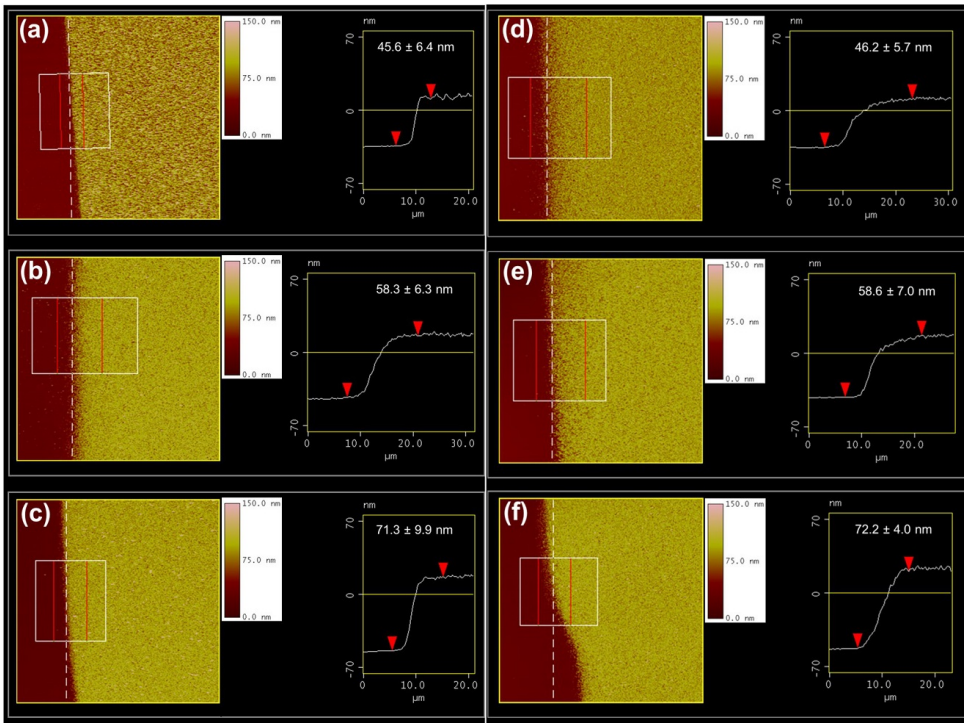

Figure A.10.: AFM topographic images (left) and cross-section analysis (right) of HKUST-1 SURMOFs with different spraying cycles. (a-c) 5, 7, and 10 spraying cycles of the pristine HKUST-1 SURMOFs; (d-f) Fc loaded HKUST-1 SURMOFs for the same samples of 5, 7, and 10 spraying cycles. An average thickness value is analyzed within the white frame (left). The thicknesses are determined by the number of spraying cycles, and the error for thickness is given by roughness average of the AFM cross-section analysis. The removal of these HKUST-1 SURMOFs was achieved by chemical etching. Data contributed by Jianxi Liu, group of Prof. Christof Wöll, Institute of Functional Interfaces (IFG), Kalsruhe Institute of Technology (KIT), 76344 Eggenstein-Leopoldshafen, Germany. Reprinted with permission from [271]. Copyright 2015 American Chemical Society.

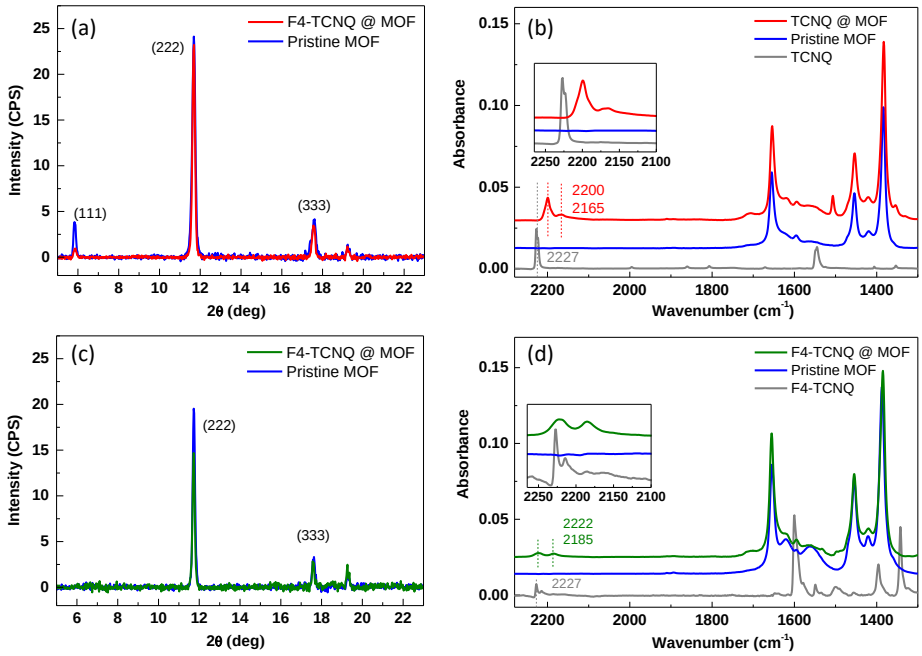

Figure A.11.: XRD and IRRAS data for pristine and loaded HKUST-1 SURMOFs. Out-of-plane XRD of representative pristine (blue) and (a) TCNQ-loaded (red) (c) F4-TCNQ-loaded SURMOF samples (5 spraying cycles). (b) IRRA spectra of representative pristine (bue curve) and TCNQ-loaded (red curve) HKUST-1 SURMOF samples (10 spraying cycles). A spectrum of F4-TCNQ drop-casted on a Au surface is shown for comparison (black curve). Inset: Selected range of the spectra (2275 and 2100 cm^{-1}) containing the C≡N band. (d) IRRA spectra of the pristine (blue curve) and F4-TCNQ-loaded (green curve) SURMOFs (5 spraying cycles). A spectrum of TCNQ drop-casted on a Au surface is shown for comparison (black curve). Inset: Selected range of the spectra (2275 and 2100 cm^{-1}) containing the C≡N band. Data contributed by Jianxi Liu, group of Prof. Christof Wöll, Institute of Functional Interfaces (IFG), Kalsruhe Institute of Technology (KIT), 76344 Eggenstein-Leopoldshafen, Germany. Reprinted with permission from [168]. Copyright 2016 American Chemical Society.

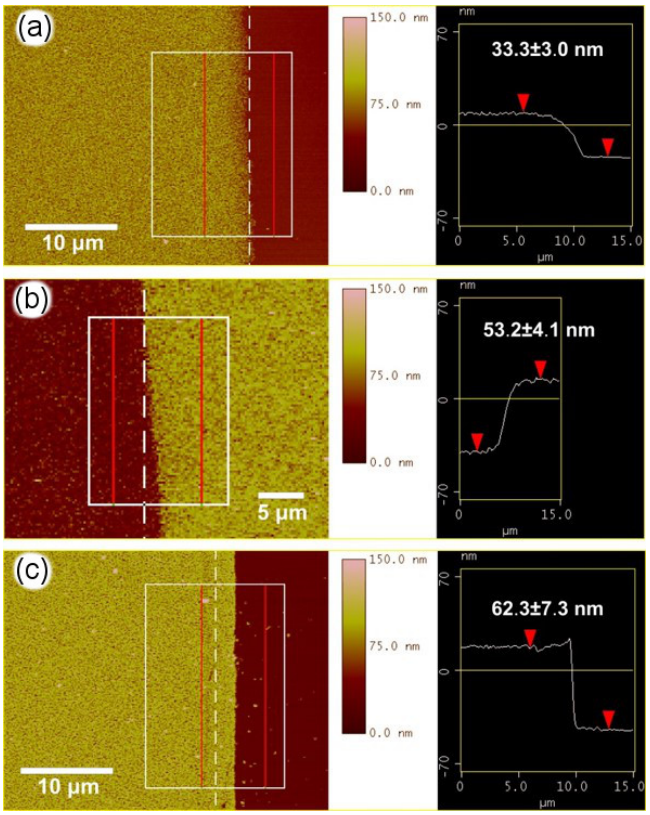

Figure A.12.: AFM topographic images (left) and cross-section analysis (right) of TCNQ-loaded HKUST-1 SURMOFs with different spraying cycles. An average thickness value is analyzed within the white frame (left). The thicknesses are determined by the number of spraying cycles, and the ror for thickness is given by roughness average of the AFM cross-section analysis. The valus are slightly lower than for the analogous pristine and Fc loaded SURMOFs. This difference is presumably related to the specific thickness of a seperate sample series. Figure A.10 shows that no thickness difference should be observed after loading. Data contributed by Jianxi Liu, group of Prof. Christof Wöll, Institute of Functional Interfaces (IFG), Kalsruhe Institute of Technology (KIT), 76344 Eggenstein-Leopoldshafen, Germany. Reprinted with permission from [168]. Copyright 2016 American Chemical Society.

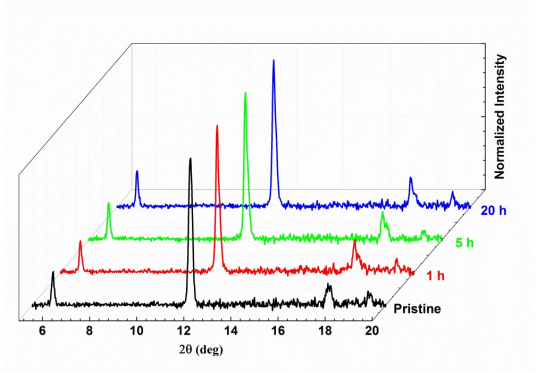

Figure A.13.: Out-of-plane X-ray diffraction data of a 10 spraying cycles HKUST-1 sample before and after immersion in HDT solution in HD for a variable amount of time (1 to 20h). Data contributed by Jianxi Liu, group of Prof. Christof Wöll, Institute of Functional Interfaces (IFG), Kalsruhe Institute of Technology (KIT), 76344 Eggenstein-Leopoldshafen, Germany. Reprinted with permission from [271]. Copyright 2015 American Chemical Society.

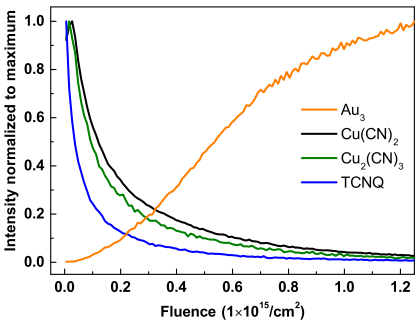

Figure A.14.: Time-of-flight secondary ion mass spctrometry (ToF-SIMS) depth profile of a representative TCNQ-loaded HKUST-1 SURMOF sample (20 spraying cycles) acquried upon C_{60} erosion to prove the efficient and homogeneous loading of the guest molecules in the nanopores. Individual signals are color-coded. All signals are normalized to the maximum for convenient presentation and comparison. Data contributed by Jianxi Liu, group of Prof. Christof Wöll, Institute of Functional Interfaces (IFG), Kalsruhe Institute of Technology (KIT), 76344 Eggenstein-Leopoldshafen, Germany. Reprinted with permission from [168]. Copyright 2016 American Chemical Society.

B. Lists

B.1. List of Abbreviations

AES Auger electron spectroscopy

AFM atomic force microscopy

AT alkanethiol

ATR attenuated total reflection

BET Brunauer-Emmett-Teller

CB conduction band

CHC core hole clock

CT charge transfer

DFT density functional theory

DOS density of states

ESCA electron spectroscopy for chemical analysis

ET electron transfer

FWHM full width at half-maximum

HOMO highest occupied molecular orbital

HRXPS high resolution X-ray photoelectron spectroscopy

IET inverse electron transfer

IMFP inelastic mean free path

IP ionization potential

IR infrared

IRRA	infrared reflection-absorption
KP	Kelvin probe
LPE	liquid phase epitaxy
LUMO	lowest unoccupied molecular orbital
MO	molecular orbital
MOF	metal-organic framework
MW	molecular wire
NEXAFS	near edge X-ray absorption fine structure
OV	occupied valence level
P	participator
PE	photon energy
PES	photoelectron spectroscopy
PEY	partial electron yield
PVD	physical vapor deposition
RAES	resonant Auger electron spectroscopy
RT	room temperature
SAM	self-assembled monolayer
SBU	secondary building unit
SERS	surface enhanced Raman spectroscopy
SIMS	secondary ion mass spectrometry
SP	spectator
STM	scanning tunneling microscopy
SURMOF	surface-anchored metal-organic framework
TDM	transition dipole moment

ToF-SIMS time-of-flight secondary ion mass spectrometry

UHV ultrahigh vacuum

UPS ultraviolet photoelectron spectroscopy

UV unoccupied valence level

UV ultraviolet

WCA water contact angle

WF work function

XPS X-ray photoelectron spectroscopy

XRD X-ray diffraction

B.2. List of Chemicals

Abbreviations of the Basic Chemicals

BDC	1,4-benzene-dicarboxylate
BTC	1,3,5-benzene-tricarboxylic acid
BPT	biphenylthiol
$CHCl_3$	trichloromethane
CMMT	9-carboxy-10-(mercaptomethyl)triptycene thiol
DCM	dichlormethane
DDT	dodecane-1-thiol
DMF	dimethylformamide
EtOH	ethanol
EGaIn	eutectic gallium indium
Fc	ferrocene
F4-TCNQ	2,3,5,6-tetrafluoro-7,7,8,8-tetracyanoquinodimethane
HCl	hydrochloric acid
HCN	hydrogen cyanide
HD	hexadecane
HDT	hexadecane-1-thiol
HKUST-1	Hong Kong University of Science & Technology - 1
KCN	potassium cyanide
KOH	potassium hydroxide
MeOH	methanol
MHDA	16-mercaptohexadecanoic acid
NaOH	sodium hydroxide

ODT	octadecane-1-thiol
PT	phenylthiol
TCNQ	7,7,8,8-tetracyanoquinodimethane
THF	tetrahydrofuran
TPT	terphenylthiol

Abbreviations of the Custom-synthesized Chemicals

AzuSH	azulene-2-thiol
NC-AzuSH	6-cyanoazulene-2-thiol
NC-AntSH	6-cyanoanthracene-2-thiol
NC-AntSeAc	6-cyanoanthracene-2-selenoacetate
NC-NapSH	6-cyanonaphthalene-2-thiol
NC-NapSeAc	6-cyanonaphthalene-2-selenoacetate
NapSH	naphthalene-2-thiol
NC-PT	4-cyanophenyl-1-thiol
NC-BPT	4′-cyanobiphenyl-4-thiol
NC-TPT	4″-cyanoterphenyl-4-thiol
PyrP1SH	4-(4-pyridyl)phenyl-1-methanethiol
PyrP0SH	4-(4-pyridyl)phenyl-1-thiol
PyrPP1SH	4′(4-pyridyl)biphenyl-4-methanethiol
PT-NO_2	4-nitrophenyl-1-thiol
BPT-NO_2	4′-nitrobiphenyl-4-thiol
TPT-NO_2	4″-nitroterphenyl-4-thiol

B.3. List of Symbols

$\mathbf{E_B}$	eV	binding energy
$\mathbf{E_{exc}}$	eV	excitation energy
$\mathbf{E_F}$	eV	Fermi level
$\mathbf{E_{kin}}$	eV	kinetic energy
$\mathbf{I}$	A	current
$\mathbf{V}$	V	voltage
$\mathbf{P_{ET}}$		portion of electron transfer events
$\tau_{\mathbf{ET}}$	fs	electron transfer time
$\tau_{\mathbf{core}}$	fs	known lifetime of inner shell vacancy
Φ	eV	work function
λ	nm	attenuation length
σ	Å^2	cross section
φ	meV	tunneling barrier
$\mathbf{R}$	Ω	resistance
ρ	$\Omega\,\text{m}$	resistivity
$\mathbf{G}$	S	conductance
β	Å^{-1}	tunneling decay constant
$\mathbf{J}$	A/cm^2	current density
α	$^\circ$	tilt angle
γ	$^\circ$	twist angle

B.4. List of Publications

Included in this Thesis

[1] P. Waske, T. Wächter, A. Terfort, M. Zharnikov, *Nitro-Substituted Aromatic Thiolate Self-Assembled Monolayers: Structural Properties and Electron Transfer upon Resonant Excitation of the Tail Group*, *J. Phys. Chem. C.* **Nov. 2014**, *Vol. 118*, pp. 26049–26060.

[2] J. Ossowski, T. Wächter, L. Silies, M. Kind, A. Noworolska, F. Blobner, D. Gnatek, J. Rysz, M. Bolte, P. Feulner, A. Terfort, P. Cyganik, M. Zharnikov, *Thiolate versus Selenolate: Structure, Stability, and Charge Transfer Properties*, *ACS Nano* **Apr. 2015**, *Vol. 9*, pp. 4508–4526.

[3] J. Liu, T. Wächter, A. Irmler, P. G. Weidler, H. Gliemann, F. Pauly, V. Mugnaini, M. Zharnikov, C. Wöll, *Electric Transport Properties of Surface-Anchored Metal-Organic Frameworks and the Effect of Ferrocene Loading*, *ACS Appl. Mater. Interfaces* **May 2015**, *Vol. 7*, pp. 9824–9830.

[4] T. Neumann, J. Liu, T. Wächter, P. Friederich, F. Symalla, A. Welle, V. Mugnaini, V. Meded, M. Zharnikov, C. Wöll, W. Wenzel, *Superexchange Charge Transport in Loaded Metal Organic Frameworks*, *ACS Nano* **July 2016**, *Vol. 10*, pp. 7085–7093.

[5] A. I. Guttentag, T. Wächter, K. K. Barr, J. M. Abendroth, T.-B. Song, N. F. Sullivan, Y. Yang, D. L. Allara, M. Zharnikov, P. S. Weiss, *Surface Structure and Electron Transfer Dynamics of the Self-Assembly of Cyanide on Au(111)*, *J. Phys. Chem. C.* **2016**, **[accepted]**.

[6] T. Wächter, A. Terfort, M. Zharnikov, *Dynamic Electron Transfer Properties of Nitrile-Substituted Anthracenethiol and -selenol*, **[in preparation]**.

[7] T. Wächter, M. Barybin, M. Zharnikov, *Structure and Electron Transfer Properties of Nitrile-Substituted Azulenethiol*, **[in preparation]**.

[8] T. Wächter, A. Terfort, M. Zharnikov, *Pyridine as Target for Site-Specific Resonant Excitation of Pyridinethiols on Noble Metal Surfaces*, **[in preparation]**.

Besides this Thesis

[1] Z. Zhang, T. Wächter, M. Kind, S. Schuster, J. W. Bats, A. Nefedov, M. Zharnikov, A. Terfort, *Self-Assembled Monolayers of Perfluoroanthracenylaminoalkane Thiolates on Gold as Potential Electron Injection Layers*, *ACS Appl. Mater. Interfaces* **Feb. 2016**, *Vol. 8*, pp. 7308–7319.

[2] I. Hehn, S. Schuster, T. Wächter, T. Abu-Husein, A. Terfort, M. Zharnikov, E. Zojer, *Employing X-ray Photoelectron Spectroscopy for Determining Layer Homogeneity in Mixed Polar Self-Assembled Monolayers*, *J. Phys. Chem. Lett.* **Aug. 2016**, *Vol. 7*, pp. 2994–3000.

[3] M. Lindner, M. Valasek, J. Homberg, K. Edelmann, L. Gerhard, W. Wulfhekel, O. Fuhr, T. Wächter, M. Zharnikov, V. Kolivoska, L. Pospisil, G. Meszaros, M. Hromadova, M. Mayor, *Importance of the Anchor Group Position (Para versus Meta) in Tetraphenylmethane Tripods: Synthesis and Self-Assembly Features*, *Chem. Eur. J.* **Aug. 2016**, *Vol. 22*, pp. 13218–13235.

[4] M. Carlotti, A. Kovalchuk, T. Wächter, M. Zharnikov, R. C. Chiechi, *Conformation-driven Quantum Interference Effects Mediated by Through-space Conjugation in Tunneling Junctions Comprising Self-Assembled Monolayers*, *Nat. Commun.*, **[accepted]**.

[5] Q. Zhang, W.-T. Wang, C.-Y. Chi, Y.-C. Huang, T. Wächter, M. Zharnikov, Y. Tai, D.-J. Liaw, *A Novel Perspective of Organic Electronic Material: An Electronically Hermaphrodite Polymer for Cathode and Anode Buffer Layers*, *Nature*, **[submitted]**.

B.5. List of Conference Contributions

[1] V. Mugnaini*, J. Liu, T. Wächter, M. Zharnikov, M. Buck, C. Wöll, Electrochemical investigation of surface anchored porous coatings, 30th European Conference on Surface Science (ECOSS-30), Antalya, Turkey, **Sept. 2014**.

[2] P. Waske, T. Wächter*, A. Terfort, M. Zharnikov, Inverse electron transfer in nitro-substituted monomolecular films, DPG Spring Meeting, Berlin, Germany, **Mar. 2015**.

[3] C. Partes, S. Schuster, T. Wächter, M. Kind*, M. Zharnikov, A. Terfort, Symmetric Attachment of Annulated Aromatic Hydrocarbons in Self-assembled Monolayers by Use of Oxazoles, 62th International Symposium of American Vacuum Society, San Jose, USA, **Oct. 2015**.

[4] J. Ossowski, T. Wächter*, L. Silies, M. Kind, A. Noworolska, F. Blobner, D. Gnatek, J. Rysz, M. Bolte, P. Feulner, A. Terfort, P. Cyganik, M. Zharnikov, Thiolate versus Selenolate: Structure, Stability, and Charge Transfer Properties, DPG Spring Meeting, Regensburg, Germany, **Mar. 2016**.

[5] J. Liu, T. Wächter, A. Irmler, P. G. Weidler, H. Gliemann, F. Pauly, V. Mugnaini, M. Zharnikov*, C. Wöll, Electric transport properties of pristine and loaded surface-anchored metal-organic frameworks, DPG Spring Meeting, Regensburg, Germany, **Mar. 2016**.

[6] A. Guttentag*, T. Wächter, K. Barr, J. M. Abendroth, T.-B. Song, Y. Yang, D. L. Allara, M. Zharnikov, P. S. Weiss, Precious poison: The self-assembly of cyanide on Au111, ACS meeting, San Diego, USA, **Mar. 2016**.

*presenting person

References

[1] H. Furukawa, K. E. Cordova, M. O'Keeffe, O. M. Yaghi, *Science* **Aug. 2013**, *341*, 1230444–1230444.

[2] D. J. Tranchemontagne, J. L. Mendoza-Cortes, M. O'Keeffe, O. M. Yaghi, *Chem. Soc. Rev.* **2009**, *38*, 1257.

[3] J. M. Tour, *Molecular Electronics*, World Scientific, **2003**.

[4] D. M. Adams, L. Brus, C. E. D. Chidsey, S. Creager, C. Creutz, C. R. Kagan, P. V. Kamat, M. Lieberman, S. Lindsay, R. A. Marcus, *J. Phys. Chem. B* **2003**, *107*, 6668.

[5] S. Karthäuser, *J. Phys.: Condens. Matter* **Nov. 2010**, *23*, 013001.

[6] D. J. Wold, R. Haag, M. A. Rampi, C. D. Frisbie, *J. Phys. Chem. B* **Mar. 2002**, *106*, 2813–2816.

[7] F.-R. F. Fan, Y. Yao, L. Cai, L. Cheng, J. M. Tour, A. J. Bard, *J. Am. Chem. Soc.* **Mar. 2004**, *126*, 4035–4042.

[8] V. B. Engelkes, J. M. Beebe, C. D. Frisbie, *J. Am. Chem. Soc.* **Nov. 2004**, *126*, 14287–14296.

[9] P. A. Lewis, C. E. Inman, F. Maya, J. M. Tour, J. E. Hutchison, P. S. Weiss, *J. Am. Chem. Soc.* **Dec. 2005**, *127*, 17421–17426.

[10] A. V. Tivanski, Y. He, E. Borguet, H. Liu, G. C. Walker, D. H. Waldeck, *J. Phys. Chem. B* **Mar. 2005**, *109*, 5398–5402.

[11] H. B. Akkerman, P. W. M. Blom, D. M. de Leeuw, B. de Boer, *Nature* **May 2006**, *441*, 69–72.

[12] A. M. Moore, A. A. Dameron, B. A. Mantooth, R. K. Smith, D. J. Fuchs, J. W. Ciszek, F. Maya, Y. Yao, J. M. Tour, P. S. Weiss, *J. Am. Chem. Soc.* **Feb. 2006**, *128*, 1959–1967.

[13] Kim, J. M. Beebe, Y. Jun, X.-Y. Zhu, C. D. Frisbie, *J. Am. Chem. Soc.* **Apr. 2006**, *128*, 4970–4971.

[14] B. Kim, S. H. Choi, X.-Y. Zhu, C. D. Frisbie, *J. Am. Chem. Soc.* **Dec. 2011**, *133*, 19864–19877.

[15] M. A. Rampi, O. J. A. Schueller, G. M. Whitesides, *Appl. Phys. Lett.* **1998**, *72*, 1781.

[16] E. A. Weiss, R. C. Chiechi, G. K. Kaufman, J. K. Kriebel, Z. Li, M. Duati, M. A. Rampi, G. M. Whitesides, *J. Am. Chem. Soc.* **Apr. 2007**, *129*, 4336–4349.

[17] O. Seitz, A. Vilan, H. Cohen, J. Hwang, M. Haeming, A. Schoell, E. Umbach, A. Kahn, D. Cahen, *Adv. Funct. Mater.* **July 2008**, *18*, 2102–2113.

[18] D. Fracasso, M. I. Muglali, M. Rohwerder, A. Terfort, R. C. Chiechi, *J. Phys. Chem. C* **May 2013**, *117*, 11367–11376.

[19] M. H. Lee, G. Speyer, O. F. Sankey, *Phys. Status Solidi B* **July 2006**, *243*, 2021–2029.

[20] D. M. Adams, L. Brus, C. E. D. Chidsey, S. Creager, C. Creutz, C. R. Kagan, P. V. Kamat, M. Lieberman, S. Lindsay, R. A. Marcus, R. M. Metzger, M. E. Michel-Beyerle, J. R. Miller, M. D. Newton, D. R. Rolison, O. Sankey, K. S. Schanze, J. Yardley, X. Zhu, *J. Phys. Chem. B* **July 2003**, *107*, 6668–6697.

[21] B. Branchi, F. C. Simeone, M. A. Rampi in *Topics in Current Chemistry*, Springer Science + Business Media, **2011**, pp. 85–119.

[22] Kim, J. M. Beebe, Y. Jun, X.-Y. Zhu, C. D. Frisbie, *J. Am. Chem. Soc.* **Apr. 2006**, *128*, 4970–4971.

[23] E. A. Weiss, R. C. Chiechi, G. K. Kaufman, J. K. Kriebel, Z. Li, M. Duati, M. A. Rampi, G. M. Whitesides, *J. Am. Chem. Soc.* **Apr. 2007**, *129*, 4336–4349.

[24] C. J. Querebillo, A. Terfort, D. L. Allara, M. Zharnikov, *J. Phys. Chem. C* **Dec. 2013**, *117*, 25556–25561.

[25] N. Tuccitto, V. Ferri, M. Cavazzini, S. Quici, G. Zhavnerko, A. Licciardello, M. A. Rampi, *Nat. Mater.* **Nov. 2008**, *8*, 41–46.

[26] C. Musumeci, G. Zappala, N. Martsinovich, E. Orgiu, S. Schuster, S. Quici, M. Zharnikov, A. Troisi, A. Licciardello, P. Samori, *Adv. Mater.* **Dec. 2013**, *26*, 1688–1693.

[27] P. A. Brühwiler, O. Karis, N. Mårtensson, *Rev. Mod. Phys.* **2002**, *74*, 703.

[28] L. Wang, W. Chen, C. Huang, Z.-K. Chen, A. T. S. Wee, *J. Phys. Chem. B* **2006**, *110*, 674.

[29] B. Kempgens, A. K. M. Neeb, H. M. Köppe, A. M. Bradschaw, J. Feldhaus, *J. Phys. B* **1996**, *29*, 5389.

[30] C. Nicolas, C. Miron, *J. Electron Spectrosc. Relat. Phenom.* **2012**, *185*, 267.

[31] R. Püttner, I. Dominguez, T. J. Morgan, C. Cisneros, R. F. Fink, E. Rotenberg, T. Warwick, M. Domke, G. Kaindl, A. S. Schlachter, *Phys. Rev. A* **1999**, *59*, 3415.

[32] B. Kempgens, A. Kivimäki, M. Neeb, H. M. Köppe, A. M. Bradshaw, J. Feldhaus, *J. Phys. B: At. Mol. Opt. Phys.* **Nov. 1996**, *29*, 5389–5402.

[33] S. Neppl, U. Bauer, D. Menzel, P. Feulner, A. Shaporenko, M. Zharnikov, P. Kao, D. Allara, *Chem. Phys. Lett.* **2007**, *447*, 227.

[34] W. Chen, L. Wang, C. Huang, T. T. Lin, X. Y. Gao, K. P. Loh, Z. K. Chen, A. T. S. Wee, *J. Am. Chem. Soc.* **2006**, *128*, 935.

[35] N. Ballav, B. Schüpbach, O. Dethloff, P. Feulner, A. Terfort, M. Zharnikov, *J. Am. Chem. Soc.* **2007**, *129*, 15416.

[36] N. Ballav, B. Schüpbach, S. Neppl, P. Feulner, A. Terfort, M. Zharnikov, *J. Phys. Chem. C* **2010**, *114*, 12719.

[37] P. Kao, S. Neppl, P. Feulner, D. L. Allara, M. Zharnikov, *J. Phys. Chem. C* **2010**, *114*, 13766.

[38] H. Hamoudi, S. Neppl, P. Kao, B. Schüpbach, P. Feulner, A. Terfort, D. Allara, M. Zharnikov, *Phys. Rev. Lett.* **2011**, *107*, 027801.

[39] F. Blobner, P. B. Coto, F. Allegretti, M. Bockstedte, O. Rubio-Pons, H. Wang, D. L. Allara, M. Zharnikov, M. Thoss, P. Feulner, *J. Phys. Chem. Lett.* **2012**, *3*, 436.

[40] A. Shaporenko, P. Cyganik, M. Buck, A. Terfort, M. Zharnikov, *J. Phys. Chem. B* **July 2005**, *109*, 13630–13638.

[41] D. Käfer, A. Bashir, G. Witte, *J. Phys. Chem. C* **July 2007**, *111*, 10546–10551.

[42] P. Cyganik, K. Szelagowska-Kunstman, A. Terfort, M. Zharnikov, *J. Phys. Chem. C* **Oct. 2008**, *112*, 15466–15473.

[43] A. Bashir, D. Käfer, J. Müller, C. Wöll, A. Terfort, G. Witte, *Angew. Chem. Int. Ed.* **June 2008**, *47*, 5250–5252.

[44] A. M. Track, F. Rissner, G. Heimel, L. Romaner, D. Käfer, A. Bashir, G. M. Rangger, O. T. Hofmann, T. Bucko, G. Witte, E. Zojer, *J. Phys. Chem. C* **Feb. 2010**, *114*, 2677–2684.

[45] M. Dendzik, A. Terfort, P. Cyganik, *J. Phys. Chem. C* **Sept. 2012**, *116*, 19535–19542.

[46] M. H. Dishner, J. C. Hemminger, F. J. Feher, *Langmuir* **Sept. 1997**, *13*, 4788–4790.

[47] K. Szelagowska-Kunstman, P. Cyganik, B. Schüpbach, A. Terfort, *Phys. Chem. Chem. Phys.* **2010**, *12*, 4400.

[48] M. G. Samant, C. A. Brown, J. G. Gordon, *Langmuir* **June 1992**, *8*, 1615–1618.

[49] J. D. Monnell, J. J. Stapleton, S. M. Dirk, W. A. Reinerth, J. M. Tour, D. L. Allara, P. S. Weiss, *J. Phys. Chem. B* **Nov. 2005**, *109*, 20343–20349.

[50] G. Heimel, L. Romaner, E. Zojer, J.-L. Brédas, *Nano Lett.* **2007**, *7*, 932.

[51] M. D. Ventra, N. D. Lang, *Phys. Rev. B* **Dec. 2001**, *65*, 045402.

[52] M. D. Ventra, N. D. Lang, S. Pantelides, *Chem. Phys.* **Aug. 2002**, *281*, 189–198.

[53] B. Kim, S. H. Choi, X.-Y. Zhu, C. D. Frisbie, *J. Am. Chem. Soc.* **Dec. 2011**, *133*, 19864–19877.

[54] M. Zharnikov, A. Shaporenko, A. Paul, A. Gölzhäuser, A. Scholl, *J. Phys. Chem. B* **2005**, *109*, 5168.

[55] J. Liu, B. Schüpbach, A. Bashir, O. Shekhah, A. Nefedov, M. Kind, A. Terfort, C. Wöll, *Phys. Chem. Chem. Phys.* **2010**, *12*, 4459.

[56] K. Peter, C. Vollhardt, N. E. Schore, *Organic Chemistry*, Macmillan Education, **2014**, 1408 Seiten.

[57] H. Hamoudi, P. Kao, A. Nefedov, D. L. Allara, M. Zharnikov, *Beilstein J. Nanotechnol.* **2012**, *3*, 12.

[58] T. Weidner, A. Shaporenko, N. Ballav, A. Ulman, M. Zharnikov, *J. Phys. Chem. C* **Jan. 2008**, *112*, 1191–1198.

[59] Q.-L. Zhu, Q. Xu, *Chem. Soc. Rev.* **Mar. 2014**, *43*, 5468–5512.

[60] G. Ferey, *Chem. Soc. Rev.* **2008**, *37*, 191–214.

[61] Y. He, W. Zhou, G. Qian, B. Chen, *Chem. Soc. Rev.* **Mar. 2014**, *43*, 5657–5678.

[62] M. P. Suh, H. J. Park, T. K. Prasad, D.-W. Lim, *Chem. Rev.* **Feb. 2012**, *112*, 782–835.

[63] T. A. Makal, J.-R. Li, W. Lu, H.-C. Zhou, *Chem. Soc. Rev.* **2012**, *41*, 7761.

[64] J. Lee, O. K. Farha, J. Roberts, K. A. Scheidt, S. T. Nguyen, J. T. Hupp, *Chem. Soc. Rev.* **2009**, *38*, 1450.

[65] V. Stavila, A. A. Talin, M. D. Allendorf, *Chem. Soc. Rev.* **May 2014**, *43*, 5994–6010.

[66] P. Falcaro, R. Ricco, C. M. Doherty, K. Liang, A. J. Hill, M. J. Styles, *Chem. Soc. Rev.* **May 2014**, *43*, 5513–5560.

[67] A. Morozan, F. Jaouen, *Energy Environ. Sci.* **2012**, *5*, 9269.

[68] D. M. D'Alessandro, J. R. R. Kanga, J. S. Caddy, *Aust. J. Chem.* **2013**, *64*, 718.

[69] M. D. Allendorf, A. Schwartzberg, V. Stavila, A. A. Talin, *Chem. Eur. J* **Sept. 2011**, *17*, 11372–11388.

[70] M. Sadakiyo, T. Yamada, H. Kitagawa, *J. Am. Chem. Soc.* **July 2009**, *131*, 9906–9907.

[71] Z. Zhang, H. Yoshikawa, K. Awaga, *J. Am. Chem. Soc.* **Nov. 2014**, *136*, 16112–16115.

[72] D. Wu, Z. Guo, X. Yin, Q. Pang, B. Tu, L. Zhang, Y.-G. Wang, Q. Li, *Adv. Mater.* **Feb. 2014**, *26*, 3258–3262.

[73] S. S. Chui, *Science* **Feb. 1999**, *283*, 1148–1150.

[74] D. Zacher, O. Shekhah, C. Wöll, R. A. Fischer, *Chem. Soc. Rev.* **2009**, *38*, 1418.

[75] O. Shekhah, H. Wang, S. Kowarik, F. Schreiber, M. Paulus, M. Tolan, C. Sternemann, F. Evers, D. Zacher, R. A. Fischer, C. Wöll, *J. Am. Chem. Soc.* **Dec. 2007**, *129*, 15118–15119.

[76] A. Dragässer, O. Shekhah, O. Zybaylo, C. Shen, M. Buck, C. Wöll, D. Schlettwein, *Chem. Commun.* **2012**, *48*, 663–665.

[77] E. Tran, M. A. Rampi, G. M. Whitesides, *Angew. Chem. Int. Ed.* **July 2004**, *43*, 3835–3839.

[78] M. A. Rampi, G. M. Whitesides, *Chem. Phys.* **Aug. 2002**, *281*, 373–391.

[79] R. E. Holmlin, R. F. Ismagilov, R. Haag, V. Mujica, M. A. Ratner, M. A. Rampi, G. M. Whitesides, *Angew. Chem. Int. Ed.* **June 2001**, *40*, 2316–2320.

[80] R. E. Holmlin, R. Haag, M. L. Chabinyc, R. F. Ismagilov, A. E. Cohen, A. Terfort, M. A. Rampi, G. M. Whitesides, *J. Am. Chem. Soc.* **May 2001**, *123*, 5075–5085.

[81] A. A. Talin, A. Centrone, A. C. Ford, M. E. Foster, V. Stavila, P. Haney, R. A. Kinney, V. Szalai, F. E. Gabaly, H. P. Yoon, F. Leonard, M. D. Allendorf, *Science* **Dec. 2013**, *343*, 66–69.

[82] G. E. Poirier, E. D. Pylant, *Science* **May 1996**, *272*, 1145–1148.

[83] R. G. Nuzzo, D. L. Allara, *J. Am. Chem. Soc.* **June 1983**, *105*, 4481–4483.

[84] M. D. Porter, T. B. Bright, D. L. Allara, C. E. D. Chidsey, *J. Am. Chem. Soc.* **June 1987**, *109*, 3559–3568.

[85] L. H. Dubois, R. G. Nuzzo, *Annu. Rev. Phys. Chem.* **Oct. 1992**, *43*, 437–463.

[86] C. D. Bain, J. Evall, G. M. Whitesides, *J. Am. Chem. Soc.* **Aug. 1989**, *111*, 7155–7164.

[87] C. D. Bain, G. M. Whitesides, *Science* **Apr. 1988**, *240*, 62–63.

[88] H. A. Biebuyck, C. D. Bain, G. M. Whitesides, *Langmuir* **June 1994**, *10*, 1825–1831.

[89] P. E. Laibinis, G. M. Whitesides, D. L. Allara, Y. T. Tao, A. N. Parikh, R. G.Nuzzo, *J. Am. Chem. Soc.* **1991**, *113*, 7152.

[90] L. H. Dubois, B. R. Zegarski, R. G. Nuzzo, *J. of Chem. Phys.* **1993**, *98*, 678.

[91] M. M. Walczak, C. Chung, S. M. Stole, C. A. Widrig, M. D. Porter, *J. Am. Chem. Soc.* **Mar. 1991**, *113*, 2370–2378.

[92] P. Fenter, P. Eisenberger, J. Li, N. Camillone, S. Bernasek, G. Scoles, T. A. Ramanarayanan, K. S. Liang, *Langmuir* **Oct. 1991**, *7*, 2013–2016.

[93] J. C. Love, D. B. Wolfe, R. Haasch, M. L. Chabinyc, K. E. Paul, G. M. Whitesides, R. G. Nuzzo, *J. Am. Chem. Soc.* **2003**, *125*, 2597–2609.

[94] A. Carvalho, M. Geissler, H. Schmid, B. Michel, E. Delamarche, *Langmuir* **Mar. 2002**, *18*, 2406–2412.

[95] Z. Li, S.-C. Chang, R. S. Williams, *Langmuir* **Aug. 2003**, *19*, 6744–6749.

[96] N. Muskal, I. Turyan, D. Mandler, *J. Electroanal. Chem.* **June 1996**, *409*, 131–136.

[97] G. Haehner, C. Woell, M. Buck, M. Grunze, *Langmuir* **Aug. 1993**, *9*, 1955–1958.

[98] A. Ulman, *Chem. Rev.* **Jan. 1996**, *96*, 1533–1554.

[99] A. Shaporenko, J. Müller, T. Weidner, A. Terfort, M. Zharnikov, *J. Am. Chem. Soc.* **Feb. 2007**, *129*, 2232–2233.

[100] F. K. Huang, R. C. Horton, D. C. Myles, R. L. Garrell, *Langmuir* **Aug. 1998**, *14*, 4802–4808.

[101] Y. Sato, F. Mizutani, *Phys. Chem. Chem. Phys.* **2004**, *6*, 1328.

[102] A. Shaporenko, A. Ulman, A. Terfort, M. Zharnikov, *J. Phys. Chem. B* **Mar. 2005**, *109*, 3898–3906.

[103] J. C. Love, L. A. Estroff, J. K. Kriebel, R. G. Nuzzo, G. M. Whitesides, *Chem. Rev.* **Apr. 2005**, *105*, 1103–1170.

[104] CambridgeSoft, ChemDraw 13.0, Software, **2013**.

[105] O. M. Yaghi, H. Li, M. Eddaoudi, M. O'Keeffe, *Nature* **Nov. 1999**, *402*, 276–279.

[106] H. Furukawa, O. M. Yaghi, *J. Am. Chem. Soc.* **July 2009**, *131*, 8875–8883.

[107] S. S.-Y. Chui, S. M.-F. Lo, J. P. H. Charmant, A. G. Orpen, I. D. Williams, *Science* **Feb. 1999**, *283*, 1148–1150.

[108] S. Hermes, F. Schröder, R. Chelmowski, C. Wöll, R. A. Fischer, *J. Am. Chem. Soc.* **Oct. 2005**, *127*, 13744–13745.

[109] Y. Yoo, H.-K. Jeong, *Chem. Comm.* **2008**, 2441.

[110] U. Müller, WO 2005/049892, **2005**.

[111] A. Schoedel, C. Scherb, T. Bein, *Angew. Chem. Int. Ed.* **Aug. 2010**, *49*, 7225–7228.

[112] R. Ameloot, E. Gobechiya, H. Uji-i, J. A. Martens, J. Hofkens, L. Alaerts, B. F. Sels, D. E. D. Vos, *Adv. Mater.* **Mar. 2010**, *22*, 2685–2688.

[113] H. K. Arslan, O. Shekhah, J. Wohlgemuth, M. Franzreb, R. A. Fischer, C. Wöll, *Adv. Funct. Mater.* **Sept. 2011**, *21*, 4228–4231.

[114] T. Ladnorg, A. Welle, S. Heißler, C. Wöll, H. Gliemann, *Beilstein J. Nanotechnol.* **Oct. 2013**, *4*, 638–648.

[115] N. Greeves, ChemTube3D, www.chemtube3d.com.

[116] P. van der Heide, *X-ray photoelectron spectroscopy : an introduction to principles and practices*, Wiley-Blackwell, **2012**.

[117] S. Hofmann, *Auger- and X-Ray Photoelectron Spectroscopy in Materials Science: A User-Oriented Guide*, 1st ed., Springer-Verlag Berlin Heidelberg, **2013**.

[118] M. Chung, L. Jenkins, *Surf. Sci.* **1970**, *22*, 479–485.

[119] NIST X-ray Photoelectron Spectroscopy Database, National Institute of Standards and Technology, Gaithersburg http://srdata.nist.gov/xps/, **2012**.

[120] G. E. McGuire, *Auger Electron Spectroscopy Reference Manual: A Book of Standard Spectra for Identification and Interpretation of Auger Electron Spectroscopy Data*, 1st ed., Springer US, **1979**.

[121] K. Jacobs, XPS Setup, http://jacobs.physik.uni-saarland.de, last accessed **24-10-2016**.

[122] D. A. Shirley, *Phys. Rev. B* **June 1972**, *5*, 4709–4714.

[123] S. Tougaard, *Surf. Interface Anal.* **Mar. 1997**, *25*, 137–154.

[124] C. L. A. Lamont, J. Wilkes, *Langmuir* **Mar. 1999**, *15*, 2037–2042.

[125] F. Schreiber, *Prog. Surf. Sci.* **2000**, *65*, 151–257.

[126] H. Kondoh, M. Iwasaki, T. Shimada, K. Amemiya, T. Yokoyama, T. Ohta, M. Shimomura, S. Kono, *Phys. Rev. Lett.* **Feb. 2003**, *90*.

[127] P. W. Atkins, J. de Paula, *Physikalische Chemie*, 4th ed., Wiley-VCH, **2006**.

[128] A. Nefedov, C. Wöll in *Surface Science Techniques*, Springer Science + Business Media, **2013**, pp. 277–303.

[129] J. Stöhr, *NEXAFS spectroscopy*, 1st ed. 1992. Corr. 2nd printing, Springer, **2010**.

[130] P. Bagus, K. Weiss, A. Schertel, C. Wöll, W. Braun, C. Hellwig, C. Jung, *Chem. Phys. Lett.* **Jan. 1996**, *248*, 129–135.

[131] P. Jiang, A. Nion, A. Marchenko, L. Piot, D. Fichou, *J. Am. Chem. Soc.* **Sept. 2006**, *128*, 12390–12391.

[132] J. G. Simmons, *J. Phys. D: Appl. Phys.* **May 1971**, *4*, 613–657.

[133] S. M. Sze, K. K. Ng, *Physics of semiconductor devices*, John Wiley & Sons, **2006**.

[134] J. J. Davis, N. Wang, A. Morgan, T. Zhang, J. Zhao, *Faraday Discuss.* **2006**, *131*, 167–179.

[135] D. Aswal, S. Lenfant, D. Guerin, J. Yakhmi, D. Vuillaume, *Anal. Chim. Acta* **May 2006**, *568*, 84–108.

[136] R. L. McCreery, *Chem. Mater.* **Nov. 2004**, *16*, 4477–4496.

[137] A. Salomon, D. Cahen, S. Lindsay, J. Tomfohr, V. Engelkes, C. Frisbie, *Adv. Mater.* **Nov. 2003**, *15*, 1881–1890.

[138] D. K. James, J. M. Tour, *Chem. Mater.* **Nov. 2004**, *16*, 4423–4435.

[139] H. B. Akkerman, B. de Boer, *J. Phys.: Condens. Matter* **Dec. 2007**, *20*, 013001.

[140] Y. A. Berlin, A. L. Burin, M. A. Ratner, *Chem. Phys.* **Jan. 2002**, *275*, 61–74.

[141] W. Wang, T. Lee, M. Reed, *Proc. IEEE* **Oct. 2005**, *93*, 1815–1824.

[142] M. L. Chabinyc, X. Chen, R. E. Holmlin, H. Jacobs, H. Skulason, C. D. Frisbie, V. Mujica, M. A. Ratner, M. A. Rampi, G. M. Whitesides, *J. Am. Chem. Soc.* **Oct. 2002**, *124*, 11730–11736.

[143] M. Duati, C. Grave, N. Tcbeborateva, J. Wu, K. Müllen, A. Shaporenko, M. Zharnikov, J. K. Kriebel, G. M. Whitesides, M. A. Rampi, *Adv. Mater.* **Feb. 2006**, *18*, 329–333.

[144] J. K. N. Mbindyo, T. E. Mallouk, J. B. Mattzela, I. Kratochvilova, B. Razavi, T. N. Jackson, T. S. Mayer, *J. Am. Chem. Soc.* **Apr. 2002**, *124*, 4020–4026.

[145] V. Mujica, M. A. Ratner, *Chem. Phys.* **Mar. 2001**, *264*, 365–370.

[146] B. Ulgut, H. D. Abruna, *Chem. Rev.* **July 2008**, *108*, 2721–2736.

[147] E. Tran, C. Grave, G. M. Whitesides, M. A. Rampi, *Electrochim. Acta* **Sept. 2005**, *50*, 4850–4856.

[148] C. Grave, C. Risko, A. Shaporenko, Y. Wang, C. Nuckolls, M. A. Ratner, M. A. Rampi, M. Zharnikov, *Adv. Funct. Mater.* **Dec. 2007**, *17*, 3816–3828.

[149] S. Maisch, F. Buckel, F. Effenberger, *J. Am. Chem. Soc.* **Dec. 2005**, *127*, 17315–17322.

[150] T. Shamai, A. Ophir, Y. Selzer, *Appl. Phys. Lett.* **2007**, *91*, 102108.

[151] F. Chen, X. Li, J. Hihath, Z. Huang, N. Tao, *J. Am. Chem. Soc.* **Dec. 2006**, *128*, 15874–15881.

[152] Y. Selzer, A. Salomon, D. Cahen, *J. Phys. Chem. B* **Oct. 2002**, *106*, 10432–10439.

[153] F.-R. F. Fan, J. Yang, L. Cai, D. W. Price, S. M. Dirk, D. V. Kosynkin, Y. Yao, A. M. Rawlett, J. M. Tour, A. J. Bard, *J. Am. Chem. Soc.* **May 2002**, *124*, 5550–5560.

[154] N. B. Zhitenev, A. Erbe, H. Meng, Z. Bao, *Nanotechnology* **Jan. 2003**, *14*, 254–257.

[155] W. Wang, T. Lee, M. A. Reed, *J. Phys. Chem. B* **Dec. 2004**, *108*, 18398–18407.

[156] C. Bock, D. V. Pham, U. Kunze, D. Käfer, G. Witte, C. Wöll, *J. Appl. Phys.* **2006**, *100*, 114517.

[157] W. Wang, T. Lee, M. A. Reed, *Phys. Rev. B* **July 2003**, *68*, 035416.

[158] Y. Selzer, M. A. Cabassi, T. S. Mayer, D. L. Allara, *Nanotechnology* **May 2004**, *15*, S483–S488.

[159] D. Segal, A. Nitzan, M. Ratner, W. B. Davis, *J. Phys. Chem. B* **Apr. 2000**, *104*, 2790–2793.

[160] T. Renger, R. A. Marcus, *J. Phys. Chem. A* **Oct. 2003**, *107*, 8404–8419.

[161] V. Lakhno, V. Sultanov, B. M. Pettitt, *Chem. Phys. Lett.* **Dec. 2004**, *400*, 47–53.

[162] D. Segal, A. Nitzan, W. B. Davis, M. R. Wasielewski, M. A. Ratner, *J. Phys. Chem. B* **Apr. 2000**, *104*, 3817–3829.

[163] F. Anariba, R. L. McCreery, *J. Phys. Chem. B* **Oct. 2002**, *106*, 10355–10362.

[164] E. A. Weiss, M. J. Tauber, R. F. Kelley, M. J. Ahrens, M. A. Ratner, M. R. Wasielewski, *J. Am. Chem. Soc.* **Aug. 2005**, *127*, 11842–11850.

[165] Xu, Zhang, Li, Tao, *Nano Lett.* **June 2004**, *4*, 1105–1108.

[166] S. H. Choi, B. Kim, C. D. Frisbie, *Science* **2008**, *320*, 1482–1486.

[167] S. A. DiBenedetto, A. Facchetti, M. A. Ratner, T. J. Marks, *J. Am. Chem. Soc.* **May 2009**, *131*, 7158–7168.

[168] T. Neumann, J. Liu, T. Wächter, P. Friederich, F. Symalla, A. Welle, V. Mugnaini, V. Meded, M. Zharnikov, C. Wöll, W. Wenzel, *ACS Nano* **July 2016**, *10*, 7085–7093.

[169] R. A. Marcus, *Rev. Mod. Phys.* **July 1993**, *65*, 599–610.

[170] F. Chesneau, J. Zhao, C. Shen, M. Buck, M. Zharnikov, *J. Phys. Chem. C* **2010**, *114*, 7112.

[171] A. Nefedov, C. Wöll in, *Vol. 51*, (Eds.: G. Bracco, B. Holst), Springer-Verlag: Berlin, Germany, **2013**, Chapter Advanced Applications of NEXAFS Spectroscopy for Functionalized Surfaces, pp. 277–303.

[172] K. Heister, M. Zharnikov, M. Grunze, L. Johansson, A. Ulman, *Langmuir* **2001**, *17*, 8.

[173] M. Zharnikov, *J. Electron Spectrosc. Relat. Phenom.* **2010**, *178–179*, 380.

[174] J. Moulder, J. Chastain, *Handbook of X-ray Photoelectron Spectroscopy: A Reference Book of Standard Spectra for Identification and Interpretation of XPS Data*, Physical Electronics Division, Perkin-Elmer Corporation, Eden Prairie, MN, USA, **1992**.

[175] R. W. Kwok, *XPSPeak 4.1*, *Department of Chemistry The Chinese University of Hong Kong* **1999**.

[176] B. D. Ratner, D. G. Castner in *Surface Analysis – The Principal Techniques*, John Wiley & Sons, Ltd, **2009**, pp. 47–112.

[177] F. Schreiber, *Prog. Surf. Sci.* **2000**, *65*, 151–257.

[178] H. Kondoh, M. Iwasaki, T. Shimada, K. Amemiya, T. Yokohama, T. Ohta, M. Shimomura, K. Kono, *Phys. Rev. Lett.* **2003**, *90*, 066102.

[179] F. Chesneau, B. Schüpbach, K. Szelągowska-Kunstman, N. Ballav, P. Cyganik, A. Terfort, M. Zharnikov, *Phys. Chem. Chem. Phys.* **2010**, *12*, 12123.

[180] H. Hamoudi, K. Döring, F. Chesneau, H. Lang, M. Zharnikov, *J. Phys. Chem. C* **2012**, *116*, 861.

[181] P. E. Batson, *Phys. Rev. B* **1993**, *48*, 2608.

[182] M. Domke, T. Mandel, A. Puschmann, C. Xue, D. A. Shirley, G. Kaindl, H. Petersen, P. Kuske, *Rev. Sci. Instrum.* **1992**, *63*, 80.

[183] P. A. Waske, W. Eck, M. Zharnikov, *J. Phys. Chem. C* **2012**, *116*, 13559.

[184] J. Stöhr, *NEXAFS Spectroscopy*, Springer-Verlag: Berlin, Germany, **1992**.

[185] M. Piancastelli, *J. Electron Spectrosc. Relat. Phenom.* **Mar. 2000**, *107*, 1–26.

[186] M. Zharnikov, *J. Electron Spectrosc. Relat. Phenom.* **Apr. 2015**, *200*, 160–173.

[187] P. Waske, T. Wächter, A. Terfort, M. Zharnikov, *J. Phys. Chem. C.* **Nov. 2014**, *118*, 26049–26060.

[188] J. Ossowski, T. Wächter, L. Silies, M. Kind, A. Noworolska, F. Blobner, D. Gnatek, J. Rysz, M. Bolte, P. Feulner, A. Terfort, P. Cyganik, M. Zharnikov, *ACS Nano* **Apr. 2015**, *9*, 4508–4526.

[189] J. Schnadt, P. A. Brühwiler, L. Patthey, J. N. O'Shea, S. Södergen, M. Odelius, R. Ahuja, O. Karis, M. Bässler, P. Persson, H. Siegbahn, S. Lunell, N. Mårtenson, *Nature* **2002**, *418*, 620.

[190] M. P. de Jong, R. Friedlein, S. L. Sorensen, G. Öhrwall, W. Osikowicz, C. Tengsted, *Phys. Rev. B* **2005**, *72*, 035448.

[191] A. Föhlisch, P. Feulner, F. Hennies, A. Fink, D. Menzel, D. Sanchez-Portal, P. M. Echenique, W. Wurth, *Nature* **2005**, *436*, 373.

[192] W. Wurth, A. Föhlisch in *Ultrafast Phenomena*, *Vol. 88*, Springer Science + Business Media, **2007**, pp. 707–709.

[193] R. Haag, M. A. Rampi, R. E. Holmlin, G. M. Whitesides, *J. Am. Chem. Soc.* **Sept. 1999**, *121*, 7895–7906.

[194] R. C. Chiechi, E. A. Weiss, M. D. Dickey, G. M. Whitesides, *Angew. Chem. Int. Ed.* **Jan. 2008**, *47*, 142–144.

[195] M. D. Dickey, R. C. Chiechi, R. J. Larsen, E. A. Weiss, D. A. Weitz, G. M. Whitesides, *Adv. Funct. Mater.* **Apr. 2008**, *18*, 1097–1104.

[196] N. Tuccitto, V. Ferri, M. Cavazzini, S. Quici, G. Zhavnerko, A. Licciardello, M. A. Rampi, *Nat. Mater.* **Nov. 2008**, *8*, 41–46.

[197] M. Zharnikov, M. Grunze, *J. Phys.: Condens. Matter* **2001**, *13*, 11333.

[198] T. Weidner, A. Shaporenko, J. Müller, M. Schmid, P. Cyganik, A. Terfort, M. Zharnikov, *J. Phys. Chem. C* **Aug. 2008**, *112*, 12495–12506.

[199] J. Thome, M. Himmelhaus, M. Zharnikov, M. Grunze, *Langmuir* **1998**, *14*, 7435.

[200] J. Horsley, J. Stöhr, A. P. Hitchcock, D. C. Newbury, A. L. Johnson, F. Sette, *J. Chem. Phys.* **1985**, *83*, 6099.

[201] T. Yokoyama, K. Seki, I. Morisada, K. Edamatsu, T. Ohta, *Phys. Scr.* **1990**, *41*, 189.

[202] S. Frey, V. Stadler, K. Heister, W. Eck, M. Zharnikov, M. Grunze, B. Zeysing, A. Terfort, *Langmuir* **2001**, *17*, 2408.

[203] M. Robin, I. Ishii, R. McLaren, A. Hitchcock, *J. Electron Spectrosc. Relat. Phenom.* **Jan. 1988**, *47*, 53–92.

[204] H. Agren, O. Vahtras, V. Carravetta, *Chem. Phys.* **June 1995**, *196*, 47–58.

[205] H. Oji, R. Mitsumoto, E. Ito, H. Ishii, Y. Ouchi, K. Seki, T. Yokoyama, T. Ohta, N. Kosugi, *J. Chem. Phys.* **1998**, *109*, 10409.

[206] J. Dauselt, J. Zhao, M. Kind, R. Binder, A. Bashir, A. Terfort, M. Zharnikov, *J. Phys. Chem. C* **Feb. 2011**, *115*, 2841–2854.

[207] S. Rangan, J.-J. Gallet, F. Bournel, S. Kubsky, K. L. Guen, G. Dufour, F. Rochet, F. Sirotti, S. Carniato, V. Ilakovac, *Phys. Rev. B* **Apr. 2005**, *71*, 165318.

[208] S. Carniato, V. Ilakovac, J.-J. Gallet, E. Kukk, Y. Luo, *Phys. Rev. A* **Feb. 2005**, *71*, 022511.

[209] H. T. Rong, S. Frey, Y.-J. Yang, M. Zharnikov, M. Buck, M. Wühn, C. Wöll, G. Helmchen, *Langmuir* **2001**, *17*, 1582.

[210] J. Hautman, J. P. Bareman, W. Mar, M. L. Klein, *Faraday Trans.* **1991**, *87*, 2031.

[211] S. Frey, A. Shaporenko, M. Zharnikov, P. Harder, D. L. Allara, *J. Phys. Chem. B* **Aug. 2003**, *107*, 7716–7725.

[212] L. Patrone, S. Palacin, J. Charlier, F. Armand, J. P. Bourgoin, H. Tang, S. Gauthier, *Phys. Rev. Lett.* **Aug. 2003**, *91*, 096802.

[213] J. Ossowski, J. Rysz, M. Krawiec, D. Maciazek, Z. Postawa, A. Terfort, P. Cyganik, *Angew. Chem. Int. Ed.* **Dec. 2014**, *54*, 1336–1340.

[214] S. Wyczawska, P. Cyganik, A. Terfort, P. Lievens, *Chem. Phys. Chem.* **Aug. 2011**, *12*, 2554–2557.

[215] M. Konopka, R. Rousseau, I. Stich, D. Marx, *J. Am. Chem. Soc.* **Sept. 2004**, *126*, 12103–12111.

[216] M. Konopka, R. Rousseau, I. Stich, D. Marx, *Phys. Rev. Lett.* **Aug. 2005**, *95*, 096102.

[217] A. Ulman, *Chem. Rev.* **Jan. 1996**, *96*, 1533–1554.

[218] K. Yokota, M. Taniguchi, T. Kawai, *J. Am. Chem. Soc.* **May 2007**, *129*, 5818–5819.

[219] T. Ishida, M. Hara, I. Kojima, S. Tsuneda, N. Nishida, H. Sasabe, W. Knoll, *Langmuir* **Apr. 1998**, *14*, 2092–2096.

[220] D. Käfer, G. Witte, P. Cyganik, A. Terfort, C. Wöll, *J. Am. Chem. Soc.* **Feb. 2006**, *128*, 1723–1732.

[221] M. Klues, K. Hermann, G. Witte, *J. Chem. Phys.* **Jan. 2014**, *140*, 014302.

[222] J. L. Bredas, G. B. Street, B. Themans, J. M. Andre, *J. Chem. Phys.* **1985**, *83*, 1323.

[223] P. Kao, S. Neppl, P. Feulner, D. L. Allara, M. Zharnikov, *J. Phys. Chem. C* **Aug. 2010**, *114*, 13766–13773.

[224] V. Huc, J.-P. Bourgoin, C. Bureau, F. Valin, G. Zalczer, S. Palacin, *J. Phys. Chem. B* **Nov. 1999**, *103*, 10489–10495.

[225] A. P. Hitchcock, G. Tourillon, R. Garrett, N. Lazarz, *J. Phys. Chem.* **Nov. 1989**, *93*, 7624–7628.

[226] A. Föhlisch, P. Feulner, F. Hennies, A. Fink, D. Menzel, D. Sanchez-Portal, P. M. Echenique, W. Wurth, *Nature* **July 2005**, *436*, 373–376.

[227] W. Wurth, A. Fröhlisch in, (Eds.: P. Corkum, D. M. Jonas, R. J. D. Miller, A. M. Weiner), Springer Berlin Heidelberg, Berlin, Heidelberg, **2007**, Chapter Direct Observation of Electron Dynamics at Surfaces using X-ray Spectroscopy, pp. 707–709.

[228] J. C. Applegate, M. K. Okeowo, N. R. Erickson, B. M. Neal, C. L. Berrie, N. N. Gerasimchuk, M. V. Barybin, *Chem. Sci.* **2016**, *7*, 1422–1429.

[229] A. I. Guttentag, T. Wächter, K. K. Barr, J. M. Abendroth, T.-B. Song, N. F. Sullivan, Y. Yang, D. L. Allara, M. Zharnikov, P. S. Weiss, *J. Phys. Chem. C (accepted)* **2016**.

[230] C. Yan, A. Gölzhäuser, M. Grunze, C. Wöll, *Langmuir* **Mar. 1999**, *15*, 2414–2419.

[231] J. Pireaux, M. Liehr, P. Thiry, J. Delrue, R. Caudano, *Surf. Sci.* **June 1984**, *141*, 221–232.

[232] Zhou, T. Baunach, V. Ivanova, D. M. Kolb, *Langmuir* **May 2004**, *20*, 4590–4595.

[233] Y. Zubavichus, M. Zharnikov, Y. Yang, O. Fuchs, E. Umbach, C. Heske, A. Ulman, M. Grunze, *Langmuir* **Dec. 2004**, *20*, 11022–11029.

[234] K. Kunimatsu, H. Seki, W. G. Golden, J. G. Gordon, M. R. Philpott, *Langmuir* **Mar. 1988**, *4*, 337–341.

[235] C. D. Zangmeister, S. W. Robey, R. D. van Zee, J. G. Kushmerick, J. Naciri, Y. Yao, J. M. Tour, B. Varughese, B. Xu, J. E. Reutt-Robey, *J. Phys. Chem. B* **Aug. 2006**, *110*, 17138–17144.

[236] M. Kiguchi, S. Miura, K. Hara, M. Sawamura, K. Murakoshi, *Appl. Phys. Lett.* **2006**, *89*, 213104.

[237] A. Kim, F. S. Ou, D. A. A. Ohlberg, M. Hu, R. S. Williams, Z. Li, *J. Am. Chem. Soc.* **June 2011**, *133*, 8234–8239.

[238] H.-J. Himmel, A. Terfort, C. Wöll, *J. Am. Chem. Soc.* **Nov. 1998**, *120*, 12069–12074.

[239] A. Shaporenko, M. Brunnbauer, A. Terfort, L. S. O. Johansson, M. Grunze, M. Zharnikov, *Langmuir* **May 2005**, *21*, 4370–4375.

[240] C. Kolczewski, R. Püttner, O. Plashkevych, H. Argren, V. Staemmler, M. Martins, G. Snell, A. S. Schlachter, M. Sant'Anna, G. Kaindl, L. G. M. Pettersson, *J. Chem. Phys.* **2001**, *115*, 6426.

[241] P. Bolognesi, P. O'Keeffe, Y. Ovcharenko, L. Avaldi, V. Carravetta, *J. Chem. Phys.* **2012**, *136*, 154308.

[242] A. Shaporenko, A. Terfort, M. Grunze, M. Zharnikov, *J. Electron Spectrosc. Relat. Phenom.* **2006**, *151*, 45.

[243] M. G. Roper, M. P. Skegg, C. J. Fisher, J. J. Lee, V. R. Dhanak, D. P. Woodruff, R. G. Jones, *Chem. Phys. Lett.* **2004**, *389*, 87.

[244] J. L. Solomon, R. J. Madix, J. Stöhr, *Surf. Sci.* **1991**, *255*, 12.

[245] R. R. Cooney, S. G. Urquhart, *J. Phys. Cem. B* **2004**, *108*, 18185.

[246] A. M. Masillamani, N. Crivillers, E. Orgiu, J. Rotzler, D. Bossert, R. Thippeswamy, M. Zharnikov, M. Mayor, P. Samori, *Chem.–Eur. J.* **2012**, *18*, 10335.

[247] J. Trotter, *Acta Crystallogr.* **1961**, *14*, 1135.

[248] I. A. Kitaigorodskii, *Organic Chemical Crystallography*, Consultants Bureau: New York, **1961**.

[249] H. M. Rietveld, E. N. Maslen, C. J. B. Clews, *Acta Crystallogr.* **1970**, *B26*, 693.

[250] G.-P. Charbonneau, Y. Delugeard, *Acta Crystallogr.* **1976**, *B32*, 1420.

[251] A. Shaporenko, M. Elbing, A. Błaszczyk, C. von Hänisch, M. Mayor, M. Zharnikov, *J. Phys. Chem. B* **2006**, *110*, 4307.

[252] J. F. Kang, A. Ulman, S. Liao, R. Jordan, *Langmuir* **Mar. 1999**, *15*, 2095–2098.

[253] C. C. Turci, S. G. Urquhart, A. P. Hitchcock, *Can. J. Chem.* **1996**, *74*, 851.

[254] C. D. Caldwell, S. J. Schaphorst, M. O. Krause, J. Jimenez-Mier, *J. Electron Spectrosc. Relat. Phenom.* **1994**, *67*, 243.

[255] P. Fenter, P. Eisenberger, K. S.Liang, *Phys. Rev. Lett.* **1993**, *70*, 2447.

[256] T. Y. B. Leung, P. Schwartz, G. Scoles, F. Schreiber, A. Ulman, *Surf. Sci.* **2000**, *458*, 34.

[257] C. Fuxen, W. Azzam, R. Arnold, G. Witte, A. Terfort, C. Wöll, *Langmuir* **2001**, *17*, 3689.

[258] T. Ishida, W. Mizutani, H. Azehara, F. Sato, N. Choi, U. Akiba, M. Fujihira, H. Tokumoto, *Langmuir* **2001**, *17*, 7459.

[259] W. Azzam, C. Fuxen, A. Birkner, H.-T. Rong, M. Buck, C. Wöll, *Langmuir* **2003**, *19*, 4958.

[260] A. Bashir, W. Azzam, M. Rohwerder, A. Terfort, *Langmuir* **2013**, *29*, 13449.

[261] H.-J. Himmel, A. Terfort, C. Wöll, *J. Am. Chem. Soc.* **1998**, *120*, 12069.

[262] R. Arnold, W. Azzam, A. Terfort, C. Wöll, *Langmuir* **2002**, *18*, 3980.

[263] J. F. Kang, A. Ulman, S. Liao, R. Jordan, G. Yang, G.-y. Liu, *Langmuir* **2001**, *17*, 95.

[264] E. Sabatani, J. Cohen-Boulakia, M. Bruening, I. Rubinstein, *Langmuir* **1993**, *9*, 2974–2981.

[265] A.-A. Dhirani, W. Zehner, R. P. Hsung, P. Guyot-Sionnest, L. Sita, *J. Am. Chem. Soc.* **1996**, *118*, 3319.

[266] Y.-T. Tao, C.-C. Wu, J.-Y. Eu, W.-L. Lin, *Langmuir* **1997**, *13*, 4018.

[267] K. T. Carron, L. G. Hurley, *J. Phys. Chem.* **1991**, *95*, 9979.

[268] C. M. Whelan, C. J. Barnes, C. G. H. Walker, N. M. D. Brown, *Surf. Sci.* **1999**, *425*, 195.

[269] C. A. Szafranski, W. Tanner, P. E. Laibinis, R. L. Garrell, *Langmuir* **1998**, *14*, 3570.

[270] M. N. Piancastelli, V. Carravetta, I. Hjelte, A. D. Fanis, K. Okada, N. Saito, M. Kitajima, H. Tanaka, K. Ueda, *Chem. Phys. Lett.* **2004**, *399*, 426.

[271] J. Liu, T. Wächter, A. Irmler, P. G. Weidler, H. Gliemann, F. Pauly, V. Mugnaini, M. Zharnikov, C. Wöll, *ACS Appl. Mater. Interfaces* **May 2015**, *7*, 9824–9830.

[272] J. L. D'Amato, H. M. Pastawski, *Phys. Rev. B* **Apr. 1990**, *41*, 7411–7420.

[273] TURBOMOLE 6.5, TURBOMOLE is a development of the University of Karlsruhe and Forschungszentrum Karlsruhe 1989–2000, **since 2007**.

[274] S. Grimme, J. Antony, S. Ehrlich, H. Krieg, *J. Chem. Phys.* **2010**, *132*, 154104.

[275] A. Schäfer, C. Huber, R. Ahlrichs, *J. Chem. Phys.* **1994**, *100*, 5829.

[276] A. D. Becke, *J. Chem. Phys.* **1993**, *98*, 1372.

[277] A. Schäfer, H. Horn, R. Ahlrichs, *J. Chem. Phys.* **1992**, *97*, 2571.

[278] V. Stehr, J. Pfister, R. F. Fink, B. Engels, C. Deibel, *Phys. Rev. B* **Apr. 2011**, *83*.

[279] P.-O. Lowdin, *J. Chem. Phys.* **1950**, *18*, 365.

[280] R. Ahlrichs, M. Bär, M. Häser, H. Horn, C. Kölmel, *Chem. Phys. Lett.* **Oct. 1989**, *162*, 165–169.

[281] A. A. Talin, A. Centrone, A. C. Ford, M. E. Foster, V. Stavila, P. Haney, R. A. Kinney, V. Szalai, F. E. Gabaly, H. P. Yoon, F. Leonard, M. D. Allendorf, *Science* **Dec. 2013**, *343*, 66–69.

[282] S. Bundschuh, O. Kraft, H. K. Arslan, H. Gliemann, P. G. Weidler, C. Wöll, *Appl. Phys. Lett.* **2012**, *101*, 101910.

[283] C. Grave, E. Tran, P. Samori, G. M. Whitesides, M. A. Rampi, *Synth. Met.* **Dec. 2004**, *147*, 11–18.

[284] L. Luo, S. H. Choi, C. D. Frisbie, *Chem. Mater.* **Feb. 2011**, *23*, 631–645.

[285] C. Untiedt, A. I. Yanson, R. Grande, G. Rubio-Bollinger, N. Agraït, S. Vieira, J. van Ruitenbeek, *Phys. Rev. B* **Aug. 2002**, *66*, 085418.

[286] D. Y. Lee, D. V. Shinde, S. J. Yoon, K. N. Cho, W. Lee, N. K. Shrestha, S.-H. Han, *J. Phys. Chem. C* **July 2014**, *118*, 16328–16334.

[287] M. Mayor, H. B. Weber, J. Reichert, M. Elbing, C. von Hänisch, D. Beckmann, M. Fischer, *Angew. Chem. Int. Ed.* **Dec. 2003**, *42*, 5834–5838.

[288] S. V. Aradhya, J. S. Meisner, M. Krikorian, S. Ahn, R. Parameswaran, M. L. Steigerwald, C. Nuckolls, L. Venkataraman, *Nano Lett.* **Mar. 2012**, *12*, 1643–1647.

[289] C. R. Arroyo, R. Frisenda, K. Moth-Poulsen, J. S. Seldenthuis, T. Bjornholm, H. S. van der Zant, *Nanoscale Res. Lett.* **2013**, *8*, 234.

[290] Y. Shen, M. W. Klein, D. B. Jacobs, J. C. Scott, G. G. Malliaras, *Phys. Rev. Lett.* **Apr. 2001**, *86*, 3867–3870.

[291] N. Tuccitto, V. Ferri, M. Cavazzini, S. Quici, G. Zhavnerko, A. Licciardello, M. A. Rampi, *Nat. Mater.* **Nov. 2008**, *8*, 41–46.

[292] C. Musumeci, G. Zappala, N. Martsinovich, E. Orgiu, S. Schuster, S. Quici, M. Zharnikov, A. Troisi, A. Licciardello, P. Samori, *Adv. Mater.* **Dec. 2013**, *26*, 1688–1693.

[293] H. L. Skriver, N. M. Rosengaard, *Phys. Rev. B* **Sept. 1992**, *46*, 7157–7168.

[294] R. G. Greenler, *J. Chem. Phys.* **1966**, *44*, 310.

Acknowledgements

I would like to thank my supervisor Prof. Dr. Michael Zharnikov for giving me the possibility to conduct the research in this interesting topic and for his support and advice during the last years.

Many thanks go to Prof. Dr. Dirk-Peter Herten for taking the position as a second referee.

I would also like to thank all my co-workers, with whom it has been a pleasure to work. This includes all my former and actual members of the group and officemates, namely Swen Schuster, Mustafa Sayin, Can Yildirim, Andre Brink, Jean Thusek, Eric Sauter, Yan Rui and Musamir Khan as well as the technical staff of our institute: Günter Meinusch, Peter Jeschka and Reinhold Jehle. Thank you for all the valuable discussions and support during my PhD time.

I am thankful to all colleagues from all over the world, who collaborated with our group in various projects: from the University of Frankfurt, Germany, the group of Prof. Andreas Terfort, who provided most of the SAM precursors for our experiments. Prashant Waske and Nikolaus Meyerbröker, Ruprecht-Karls University, Heidelberg, Germany, who conducted the synthesis of the nitro-substituted molecules and the group of Prof. Mikhail V. Barybin from the University of Kansas, USA, for the synthesis of the azulene precursors.

Regarding our cooperation in the thiolate versus selenolate sub-project, I would like to thank Jakub Ossowski, Agnieszka Noworolska, Dominika Gnatek, Jakub Rysz and Prof. Piotr Cyganik from the Jagiellonian University, Krakow Poland as well as Laura Silies, Martin Kind, Michael Bolte and Prof. Andreas Terfort from the University of Frankfurt, Germany and Florian Blobner as well as Prof. Peter Feulner from TU München, Garchingen, Germany.

For the cooperation regarding the cyanide on gold sub-project, I would like to thank Andrew I. Guttentag, Kristopher K. Barr, John M. Abendroth, Tze-Bin Song and Prof. Paul S. Weiss from the University of California, Los Angeles, USA as well as Nichole F. Sullivan and Prof. David L. Allara from the Pennsylvania State University, Pennsylvania, USA.

In relation with the MOF projects, my thank goes to Jianxi Liu from the group of Prof. Christof Wöll, KIT in Eggenstein-Leopoldshafen, who synthe-

sized and characterized the SURMOF samples and took several trips to Heidelberg to discuss our results. From the same institute, I also have to thank Peter G. Weidler, Hartmut Gliemann, Veronica Mugnaini, Tobias Neumann, Pascal Friederich, Franz Symalla, Alexander Welle, Velimir Meded and Prof. Wolfgang Wenzel and from the University of Konstanz, Germany, Andreas Irmler and Prof. Fabian Pauly.

I would also like to thank the HZB and MAX-lab for the allocation of various beamtimes and the staff for technical support. In particular: A. Nefedov and Ch. Wöll for technical cooperation at BESSY II and A. Preobrajenski for technical assistance at MAX-lab.

Thanks go to the German Research Society (DFG) for financially supporting this work.

Thanks go to my parents and my brother, for always supporting me in my decisions and helping me to reach my goals.

Last but not least, my deepest gratitude for having confidence in me and also *pushing* me, if necessary, goes to my wife Tabea.